國 立 中 央 大 學

太 空 科 學 研 究 所

博 士 論 文

太陽日冕中高能電子的無碰撞傳輸

研 究 生: 李 光 武

指導教授: 郝 玲 妮 教授

Jörg Büchner 教授

Nina Elkina 博士

中華民國九十七年六月二十四日

Collisionless Transport of Energetic Electrons in the Solar Corona

Author: Kuang Wu Lee

Advisor: Prof. Lin-Ni Hau

Prof. Jörg BÜchner

Dr. Nina Elkina

Institute of Space Science, National Central University

June 24th, 2008

Acknowledgement

Two years of intensive work in Max-Planck-Institut für Sonnensystemforschung (MPS), finally, this thesis was finished by the end of year 2007. I would like to dedicate this work to one of my supervisors, Dr. Elkina, who gives help and suggestions not only on work but also on many aspects of my life in Germany.

The stay in MPS is a very promising experience for me, not only expend my horizon of different cultural life but also the way of proceeding research. For the offering of this unique chance, I am very grateful for another supervisor, Prof. Buechner. He kindly agreed my participation in his group in the year 2006 and suggested some directions of research in this limited two-year period.

Before the visit of MPS in Katlenburg-Lindau, I spent three years in doctoral program with my supervisor in home institution, Prof L.-N. Hau, with her I learned the spirit of perusing perfection as a researcher in plasma physics. With her encouragement, I prepared myself many useful skills for the work challenges in MPS.

In Katlenburg-Lindau I had spent very good time with friends, like Setareh, Xiaobo and Jean in our group. The life overlapped with some close friends I cherish very much, they are Elena, Thomas and Konstantine, the mother, father and their lovely son.

There are still so many people who have helped me or shared good time with me, either in MPS or Institute of Space Science, National Central University. Although the names are not written in this acknowledgement, you are all deeply carved in my memory.

摘要

在無碰撞的太陽日冕電漿環境中有許多的瞬間高能現象發生。由於日冕中極低的粒子密度，以及瞬間高能現象的時間尺度遠小於碰撞週期，因此古典的粒子彈性碰撞在此環境中並不適用。在此環境下非碰撞的傳輸效應對於電漿分布的演化有決定性的影響。由最新的太陽閃焰觀測中，我們常可發現所謂的”不連續冪次分佈”，其代表著無碰撞電漿傳輸效應的強大影響力。在太陽日冕物理中，另一個重要的主題是關於太陽閃焰前磁重聯的產生機制。在強磁化的無碰撞電漿中，帶電粒子是被束縛於特定的磁力線上。當磁重聯產生時，由於強電流產生的非碰撞的傳輸效應，帶電粒子的”磁凍結效應”會被打破。而此非碰撞傳輸效應也就是所謂的”異常電阻”。

本論文中，我們將首先以線性估算的方式，探討太陽日冕的磁場環境下可產生的異常電阻。對於電漿，我們以多流體的方式來描述系統中產生的電漿波與不穩定性。由先前的模擬結果我們知道，區域性的電漿靜電結構對於電漿傳輸特性有很大的影響。線性頻散分析結果顯示出，兩種靜電不穩定性在此電流環境下成長，他們分別是 Buneman instability 與 modified two stream instability (MTSI)。其頻率以及波數的頻譜也在此分析。為了推估不穩定性在飽和條件下所產生的異常電阻，我們與先前的 Vlasov 模擬結果做比較。有別於傳統上認為 Buneman 不穩定性提供了大部分異常電阻的產生，我們發現斜向傳播的 MTSI 也可產生可觀的異常電阻。

在觀測中，通常太陽閃焰所推估的高能電子約是幾十至幾百 keV，然而若以日冕區域的磁重聯出流 Alfvén 速度推估，電子的動能最多只有幾個 keV。為了解決此能量上的不一致，觀測上所看到的日冕環頂 Hard X Ray 來源，因此被推測是一個快速震波。快速震波是一個很有效率的粒子加速機制，許多的二維日冕磁流體模擬也顯示出日冕環頂快速震波的存在。然而因為磁流體所須符合的電中性，以及電子離子等溫條件，磁流體模擬結果並無法解釋所觀測到的能量不一致。對於此一問題，我們以理論推估的磁重聯出流 Alfvén 速度，以及一個反射邊界條件，對日冕環頂快速震波做一維電磁粒子模擬 (1D EM PIC)。結果顯示原本大約 7 keV 的電子經過快速震波後大約可以加速到 120 keV，也就是到達了日冕環頂 Hard X Ray 的能量範圍。

另外，對於沿著日冕環頂向色球層傳輸的高能電子流會造成日冕區域違反電中性，反向電流因此被提出來解決此一問題。在此條件下，一個背景質子與兩個對向流動的電子物種存在於系統中。線性分析結果顯示出兩種不同的靜電不穩定性存在，分別是 Buneman 與 electron-electron two stream 不穩定性。以Vlasov 模擬在周期性邊界條件下，靜電 Double Layers (electrostatic DLs) 的產生可以耗散反向運動的電子流，而電漿的加熱效應在模擬的飽和階段是自然的結果。在此系統中 DLs 扮演了能量轉換者的角色。此一靜電結構在發展初期將電子流的動能轉換為電漿波的能量，並且在結構發展的飽和階段又將電漿波的靜電場能轉換為

電漿的熱能。另一個值得注意的模擬結論是，原本由日冕環頂向下傳輸的高斯分佈電漿，在經過與 DLs 交互作用後逐漸演化成”不連續冪次分佈”。 此結果顯示出不連續冪次分佈可能是電漿與日冕環中靜電 Double Layers 的自然結果。

Abstract

Many energetic and transient plasma phenomena take place in collisionless solar coronal environment. The classical binary collision in the corona takes relatively longer time than the usual time scale of the phenomena, and the mean free path of plasma is around 1 AU in coronal condition. Therefore the collisionless transport dominates the plasma evolution in this environment. From recent observations of solar flares, the spectrum shows a clear broken-power-law distribution, which indicates a strong influence of collisionless plasma transport effect. Another important topic in solar corona physics is the magnetic reconnection which is assumed to take place prior to the solar flare. To break the frozen-in condition in strongly magnetized collisionless plasma, some resistive effect should take place to reduce the curl-B generated current, i.e. the anomalous resistivity causes the current reduction in central current sheet.

In this thesis the anomalous resistivity is first studied from a linear estimation in a current carrying system. A multi-fluid description of plasma is used to study the waves and instabilities with coronal plasma parameters. As we know the localized electrostatic structures influence significantly on plasma transport in current carrying system. Two instabilities, the Buneman instability and the modified two stream instability (MTSI), are identified and their frequency wave-number (ω-k) spectra are analyzed. To estimate the resulting anomalous resistivity in the instability saturation stage, we compare with the previous Vlasov simulation results. We found, in contrast to the general understanding that Buneman mode contributes primarily to the generated anomalous resistivity, an obliquely propagating modified two stream instability also generates a non-negligible anomalous resistivity.

Because of the energy gap between the coronal reconnection outflow and the observed chromospheric hard X ray (HXR) emission, an existence of loop-top fast shock was proposed for a secondary acceleration of electrons. We performed a one-dimensional electromagnetic particle-in-cell simulation with a reflective boundary, which mimics the coronal soft X ray (SXR) loop. Because of the accumulation of magnetic field, a clear fast mode magnetosonic shock formed on upstream side of the reflective boundary. Electron and ion heating are shown in the downstream of the fast shock. An original reconnection outflow with *7 keV* kinetic energy can be finally accelerated to around *120 keV*, which is the typical energy level of the observed flare footpoint emissions.

As to the frequently observed flare broken-power-law spectrum, which is best fitted by two different distribution index, we are interesting in the generation

mechanism of this specific spectrum. For high energy electrons traveling downward to chromosphere in the coronal loops, a return current model is proposed to satisfy the charge neutrality condition in corona and also the Faraday's induction law in flaring loops. With a stationary background ion species and two counter-streaming electron species, Buneman and electron-electron two stream instability take place in the current-free system. In the Vlasov simulation with periodic boundary condition, electrostatic double layers (DLs) are generated to dissipate the drifts of counter-streaming electrons. Plasma heating is a natural consequence in the final stage of plasma evolution. In the system the electrostatic double layers take the role as an energy converter. DLs first accumulate kinetic energy from electron drifts for its growth of electric field energy, and in the late stage of DLs evolution the wave energy is further converted into thermal energy of plasma. Interestingly the spectrum of downward propagating electron finally shows a broken-power-law distribution, which corresponds to the frequent observed footpoint emissions. The result shows that a broken-power-law spectrum on flare footpoints is possibly a consequence of collisionless plasma transport with electrostatic DLs.

List of Figures

Contents

Chapters

1 Introduction

1.1 Overview on Solar Corona Observations

The visible part of our sun that can be seen with naked eyes is the so-called photosphere. Like the surfaces of other stars in Galaxy, the sun emanates the optical radiations that has an effective blackbody temperature approximately $T_{\odot} \approx 5785K$. However, for observations with different bands of emissions such as hard X-ray (HXR), soft X-ray (SXR) or radio wavelength, the photosphere becomes invisible for eyes but other solar structures can be seen by instruments.

Beneath the photosphere is the solar convection zone, which is defined as the height for standard one solar radius ($R_{\odot} \approx 700Mm$) from the solar centroid core to the top of convection zone. And above which, the photosphere is the lowest layer of solar atmosphere, and above photosphere lies the the rarer and more dynamical chromosphere, and the outer most solar atmosphere is the solar corona.

Along the radial direction of the solar atmosphere, the temperature decreases from the bottom of photosphere $T = 5785K$ to the value $T = 4300K$ on the top. The chromosphere lies about $2000km$ above the photosphere. The temperature rises across the chromosphere from $T = 4300K$ of the bottom to about $T = 1 \times 10^4 K$ on the top, and it reaches $T = 2 \times 10^6 K$ in solar corona. Solar corona is a highly non-uniform region, in the sense of magnetic field and thermal pressure. Several large-scale and highly energetic events, such as solar flares and coronal-mass-ejections (CMEs), take place therein. Also, the plasma dynamics and magnetic field geometry in this region are very complicated, the solar corona environment has attracted a substantial interests from the solar-terrestrial interaction study, and the solar corona is usually considered as a natural environment for plasma experiments. Therefore, the evolutions of the spectrum of energetic particles in this collisionless environment are the primary tools and themes of many coronal studies.

Concerning the topic of energetic plasma transport in collisionless corona, we briefly introduce the selected solar environments that we are interested. Conventionally, solar corona is surficially subdivided into three regions, which by individual has very different magnetic field and plasma density characteristics: (1) solar active regions, (2) quite sun and (3) coronal holes.

1. Active Regions

Active regions are the locations of highly magnetic field concentrations. With the dynamic plasma motions in photosphere and chromosphere, the magnetic activities in corona exhibit perminant features, e.g. magnetic reconfigurations, flux cancellation and magnetic field reconnection processes.

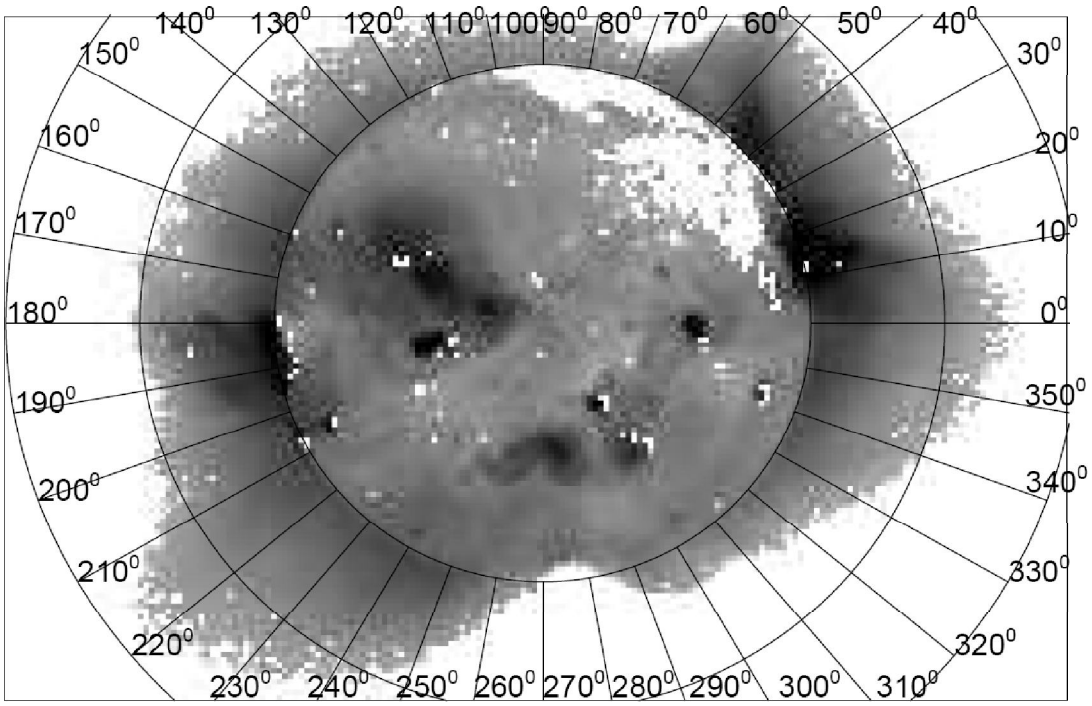

Figure 1.1: Composite soft X-ray image of the sun observed on 1992 Aug 26 with Yohkoh. The labels indicate the locations of active regions (AR; dark grey), quiet sun regions (QS; light grey), and coronal holes (CH; white) (Aschwanden 2001).

The overall area of solar active regions accounts for a relatively samll fraction of the entire coronal surface. The most pronounced expression of a typical coronal active region is the appearance of sunspot groups, which stretch strong magnetic fields from solar convection zone to corona. Sunspot groups are the regions that possess a major magnetic polarity, accompanying with a considerable amount of relatively small-scale oppositely-polarized poles. Active regions are comprised mainly of closed magnetic field lines because of the bipolar nature of magnetism ($\nabla \cdot \vec{B} = 0$: no magnetic single pole exists), although the observational existence of magnetic single poles is still a puzzle and its creation mechanism attracts high interests contemporarily from the solar physicists. It's currently believed the single poles reveal partially the extensive magnetic strucutres beneath corona.

In the region of highly magnetic polarity alternations, various energetic and dynamical processes such as corona mass ejections (CMEs), solar flares and the associate plasma heating occur continuously. A prominent plasma heating phenomenon that can be seen from solar soft X-ray (SXR) is the bright corona loops, which are caused by the plasma filling from the chromospheric plasma evaporation (this is the consequence of energetic coronal plasma bombardment) and the SXR loop usually has a longer lifetime than the HXR transient events. Solar SXR loops are hotter and denser plasma regions than its ambient environment, and they are the common post-products of the plasma ejection from coronal looptop. The spatial extension of solar SXR loops covers a wide range of scale according to their different equilibrium conditions.

2. Quiet Sun

In the early days of solar study, the remaining areas except the solar active regions were dubbed the quiet sun regions. However, with time many dynamic processes have been discovered all over the solar surface, the name 'quiet sun' is considered as a misnomer, only justified in a relative term of levels. Dynamic processes in the quiet sun range from many small-scale phenomena such as network heating events, nanoflares, explosive events, bright points, and soft X-ray jets, and to large-scale structures, such as transequatorial loops or coronal arches. The distinction between active regions and quiet sun regions becomes more and more blurred because most of the large-scale structures that overarch quiet sun regions are rooted in active regions. A good working definition is that quiet sun encompass all closed magnetic field regions (excluding active regions), clearly demarcating the quiet sun territory from coronal holes that encompass the open magnetic field regions.

3. Coronal holes

The northern and southern polar zones of the sun have generally been found to be darker than the equatorial zones during solar eclipses. Waldmeier (1957) thus coined those zones as "Koronale Löcher" (in German, i.e., coronal holes). Today it is fairly clear that these zones are dominated by open magnetic field lines, which act as efficient conduits for flushing heated plasma from the corona into the solar wind, if there are any chromospheric upflows at their footpoints. Because of this efficient transport mechanism, coronal holes are empty of high temperature plasma most of the time, and thus appear much darker than the quiet sun, where heated plasma upflowing from the chromosphere remains trapped until it cools down and precipitates back to the chromosphere.

Like our Earth atmosphere displays a large variety of cloud shapes, the solar corona exhibits an equally rich menagery of loop morphologies, which can reveal important clues about the underlying magnetic reconnection and reconfiguration processes. The rapidly varying processes, which all result from a loss of equilibrium and also called eruptive processes, such as flares, coronal mass ejections or small-scale variability phenomena, take place in the coronal active regions.

Among which we are more interested in solar flares, not only because flare is the most energetic phenomenon but also because of its rich relevant plasma physics that can possibly be applied to many plasma environments, which sometimes have great similarity, e.g. the terrestrial magnetosphere or even the laboratory torus geometry. A flare process is associated with a rapid energy release in the solar corona, believed to be driven by stored non-potential magnetic energy and triggered by instabilities during the magnetic reconfiguration. Such energy release process results in the acceleration of nonthermal particles and eventually causes heating of coronal/chromospheric plasma. These processes emit radiation in almost all wavelengths. To study the solar flare plasma dynamics, electromagnetic emission in the hard X-ray range of $\epsilon_X \approx 10 - 300keV$ is very helpful since the high spectral energy nature of solar flares. Nevertheless after the impulsive phase of flares, the emission spectrum gradually switches to soft X-ray range ($\epsilon_X \leq 10keV$), therefore with the observation instruments in that energy range can help to build a complete scenario of flare evolution. The temporal and delicate spatial profiles of flare spectra are

the major criteria and diagnostics of flare evolution, and should also be used as the final judgments of all the proposed mechanisms. In the following section we will primarily introduce the basic flare spectra features.

1.2 Electron Spectrum Evolution during Solar Flares

Electromagnetic emissions of the hard-X-ray (HXR) in the energy range ($\epsilon_X \approx 10 - 300keV$) is mainly caused by plasma thick-target radiations, which are the interactions between the relativistic electrons and background thermal ions. Solar HXR provides the primary diagnostics of plasma acceleration and transport evolution in the coronal loops. In the view that solar HXR is generated in the collisional chromosphere by the pricipitating electrons from collisionless corona, the informations about plasma transport come mainly from the HXR energy spectra of pricipitation cites, the energy-dependent timing and the temporal evolution of other emission bands. Therefore with the piecewise informations from HXR, models of plasma transort are proposed to reconstruct the corresponding magnetic topology and allow us to localize the primary particle acceleration sites, comparing to the strong HXR emission footpoints.

The ultimate goal of the diagnostics is to utilize the remote observations on the reconstruction of a global physical picture to understand the particle energization and transport characteristics in solar flares. The theoretical and observational milestones of solar flare study in the last 20 years are the creation of loop-top HXR source model and the electron time-of-flight measurements, which both point out consistently that the acceleration and injection of energetic particle occur in between the reconnection site and the SXR coronal loops (Masuda et al. 1994). With the high spatial resolution and the wide energy range capability of photometers onboard the sattelite RHESSI, fine temporal variations of solar flares spectra are revealed and hence refocus our attentions to the observational-compatible models.

Basically there are several interesting characteristics of flare HXR emissions, and those representative facts are used as criteria of determining feasible models: (1) Looptop HXR source, (2) Time-of-flight delays, (3) Chromospheric height dependent HXR peaks and (4) Soft-hard-soft spectral evolutions.

1.2.1 HXR Sources above Coronal SXR Loop

Conventionally, the solar flares are classified into two categories. According to the time profiles of solar flares, flares with the long-lived and slow-developing SXR and HXR profiles with a clear inverted Y-shaped are considered as the results of magnetic reconnection. This type of flares has the name 'two ribbon flares'; A different mechanism, seems, is required for the explanation of the other type of flares, which have a much shorter and impulsive HXR profile, the so called 'compact flares'.

The discovery of hard X-ray sources located above the soft X-ray-bright flare loops (see Fig. 1.2) by Masuda et al. (1994) represented a major breakthrough in locating the sites of particle acceleration sources downword magnetic reconnection points (Fletcher & DePontieu 1999). Previously it was not clear whether HXR-emitting electrons are

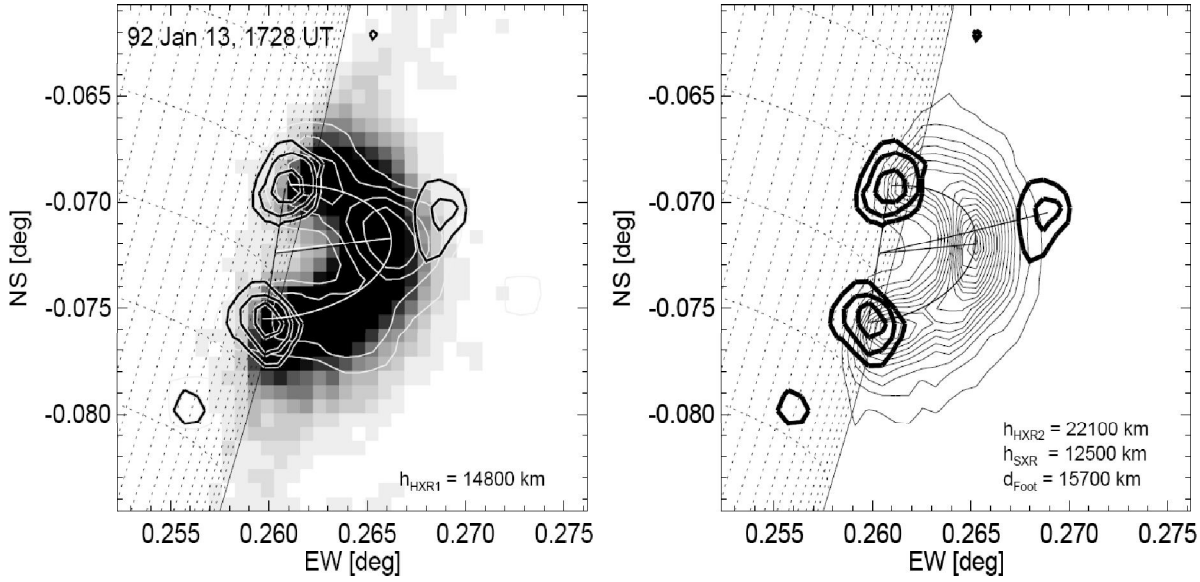

Figure 1.2: Coronal soft X-ray and hard X-ray emission observed during the Masuda flare (Masuda et al. 1994)

accelerated inside or outside prominent soft X-ray flare loops. However, since plasma densities above flare loops are relatively low, no hard X-ray emission was expected in this collisionless plasma above flare loops. Therefore, Masuda's discovery of hard X-ray emission above soft X-ray-bright flare loops changed our minds.

With this observational evidence of the looptop hard X-ray source, it is claimed by Masuda that these two kinds can be caused by the same mechanism with different emission demonstrations, i.e. these two types have the shared characteristics. The unified picture of these two kinds of solar flares is supported by the so called 'Masuda flare' event in the active region (NOAA 6994 on 13 January 1992), of which it consists of a clear structure of two SXR ribbons with a fast-evolving single spike of HXR at $\geq 20keV$. With the help of the integrated power of the hard X-ray telescope and the soft X-ray telescope on board the Yohkoh satellite (Ogawara et al. 1991), and with its highly increased spatial resolution, an intense HXR source is identified well above the apex of coronal SXR-loop. For this event the 'looptop' HXR source is significantly higher than the top of SXR loop about $10^5 km$ and has no direct counterpart of SXR image.

Also, the consequence of the looptop HXR observation suggests the existence of a collisional high density region in the original dilute collisionless corona. Considering the possible magnetic field geometry of the HXR-corresponding high energy particles, the formation of a magnetosonic fast shock above the looptop HXR source is speculated. Therefore the high energy particles, inverted from the looptop HXR emission, are proposed as the products of a fast shock acceleration.

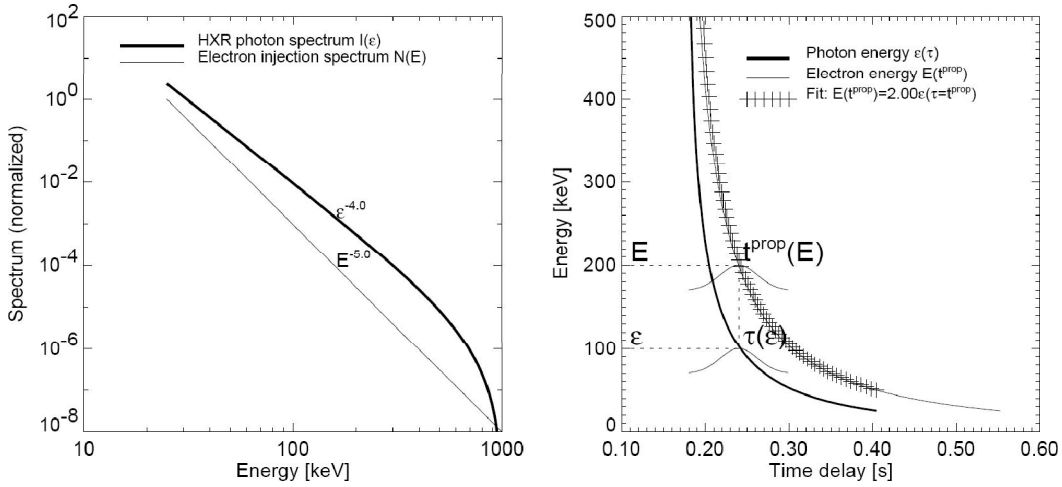

Figure 1.3: Theoretical prediction of time-of-flight delays of coronal loop HXR emissions (Aschwanden & Schwartz 1996)

1.2.2 HXR Time-of-Flight Delays

Although the energized nonthermal electrons propagate with relativistic speed, it still takes a finite time to travel from the coronal acceleration site to the chromospheric precipitation (and hard X-ray emission) site. Suppose that the electrons of the distribution in the whole energy range is accelerated synchronously and leaves the acceleration site at the same time, particles of the same pitch angle with higher energy should arrive the chromospheric emission site in a relatively shorter time than the lower energy ones. Hence a time delay of HXR peaks in different photon energies is expected from spectrum observations. Such energy-dependent time delays due to velocity dispersion is named as time-of-flight (TOF) delays, and they have been measured from BATSE/CGRO data in virtually all flares with pulse structures.

The relative time delays between adjacent energy channels are generally very small. To measure reliably such small time delays beyond the temporal resolution or time binning of the instrument, a trick is simply used that implements a cross-correlation technique with interpolation at the maximum of the cross-correlation coefficient (CCC), which yields a sub-binning accuracy if the photon statistics are sufficiently high. For most of the flare cases, with a inferred flare loop size and TOF delays measurements, a direct deduced conclusion is that the particle acceleration time is much shorter than the free-streaming time, implying that the particle acceleration take place synchronously at the loop cusp regions, but not in the propagation path. A theoretical time-dependent hard X-ray photon spectrum is shown in Fig.1.3, in which a time-dependent electron injection spectrum is computed (Aschwanden & Schwartz 1996).

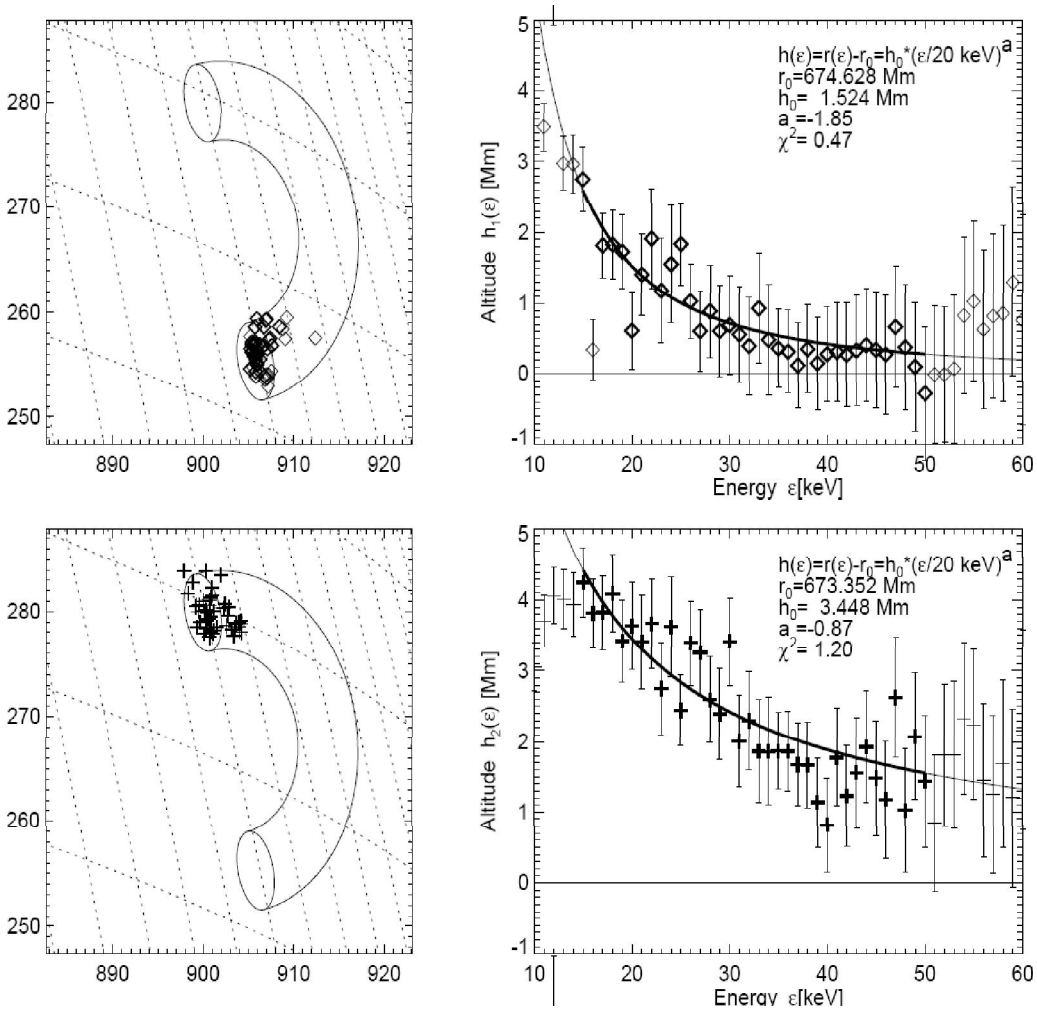

Figure 1.4: Altitude measurements of the northern and southern hard X-ray sources, carried out by using RHESSI observations for the 2002-Feb-22 flare, are shown (Aschwanden et al. 2002).

1.2.3 Chromospheric Height-Dependent HXR Peaks

Coronal loop footpoint sources generally show nonthermal hard X-ray spectrum during flares. Hard X-ray footpoint sources coincide with the endpoints of soft X-ray flare loops, so they have to be located in the chromosphere or slightly above in the transition region. This is expected from the thick-target bremsstrahlung model, if acceleration of precipitating electrons takes place at (collisionless) coronal heights. The height of these hard X-ray footpoint sources depends on the electron energy as well as on the chromospheric density $n_p(h)$ as a function of altitude h which determines the stopping depth of precipitating electrons (see e.g. Brown et al. (2002a)). A simplified derivation of the height of hard X-rays sources is given by Brown et al. (2002), which is given with the assumptions of (1) no mirroring of particles, (2) full target ionization, (3) 1D Coulomb collisional transport, neglecting pitch angle changes, and (4) power law function for electron injection flux energy spectrum. Altitude measurements of the hard X-ray sources carried out by using RHESSI

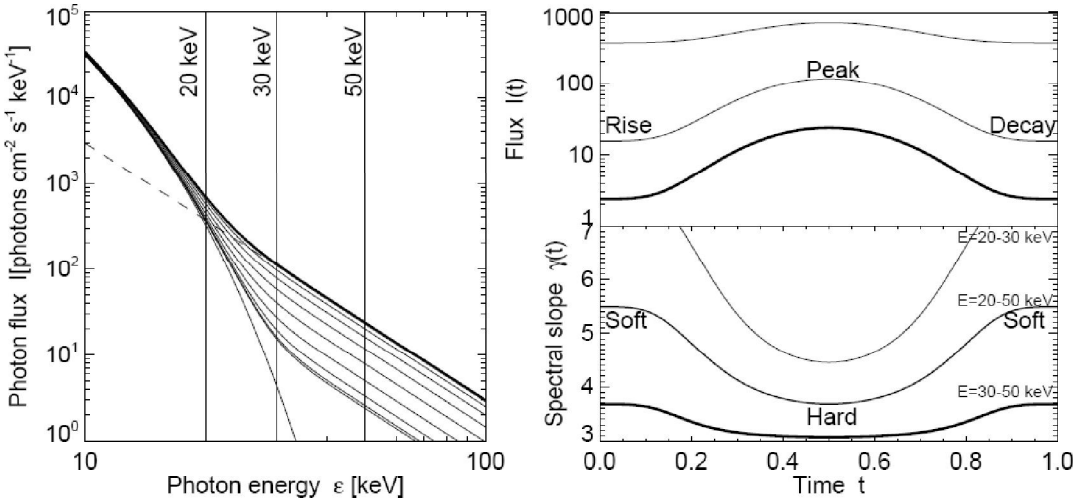

Figure 1.5: Simulation of spectral evolution during a flare. The spectra were calculated with the CHIANTI code by Phillips (2004), except that the nonthermal component varies in time between 10% and 100% of the total thermal energy. The resulting spectra are shown (left), and the temporal evolution of the fluxes at 20, 30, and 50keV are shown (top right).

observations for the 2002-Feb- 22 flare are shown in Fig.1.4, and the centroid height of hard X-ray footpoint sources is located at progressively lower altitudes with higher energies, as pointed out in Matsushita et al. (1992). The source-averaged electron spectrum of different HXR peaks are obtained via numerical inversion of the photon spectrum, and it also confirmed the basic broken power-law found by using forward-fitting (Holman et al. 2003).

1.2.4 Soft-Hard-Soft Spectral Evolution

Petrosian et al. (2002) made a study of looptop sources and footpoints in Yohkoh events. They found that the spectral index of the looptop source is softer than the footpoints on average by a factor of 1. Masuda et al. (1994) first noted a third HXR source situated above the looptop. Alexander and Metcalf (1997) analyzed this event carefully, concluding that the looptop source can be best described by a thermal component with a non-thermal tail.

The source-averaged hard X-ray spectra of flares initially often show a steep spectral slope (soft), which flattens at the peak of the flare (hard), and then becomes steeper again (soft) in the decay phase of the flare. This evolutionary pattern has been called the soft-hard-soft evolution. The thermal spectrum has a much steeper slope than the nonthermal power law in the range of $20 - 30keV$. The soft-hard-soft (SHS) spectral evolution often seen in impulsive flares (Grigis 2004) and this important observation about the time behavior of the HXR flux has already been made in the late 1960s by Parks and Winckler (1969) and Kane and Anderson (1970). The SHS may contribute to both the downward and upward motions of nonthermal sources along the flare loop (Sui et al. 2006).

It is found that the soft-hard-soft behavior appears in both, coronal source and foot-

points. This is a strong indication that soft-hard-soft is a feature of the acceleration mechanism rather than a transport effect (Battaglia and Benz 2006). A theoretical result of the spectum from simulation is shown in Fig.1.5 (Phillips 2004).

1.3 Open Questions in Solar Flare Research

1.3.1 Particle Acceleration

Magnetic reconnection is the trigger mechanism of energy release in most of the solar flare models. This process reconnects the original two seperated magnetic field lines into a new field line of a lower energy state, and it is a way of converting the stored magnetic energy into particle thermal and kinetic energy. It takes place usually above the coronal cusp-region, and it is believed to be the primary energy source that generates the observed high-energy particles in terms of HXR photons.

According to a large scale coronal structure consideration, i.e. the MHD model, the plasma velocity of reconnection outflow is close to the coronal Alfvén speed. A typical Alfvén speed calculated from SOHO/EIT measurements of 30 coronal loops in active regions (Aschwanden 1999a), at the possible height of reconnection sites, is in the range of $V_{Al} = 1000 \sim 3000 km/sec$, which is less than 1% speed of light and has a thermal distribution characteristics. However, even till now there is only one observation that can be interpreted as the direct signature of reconnection outflow, which demonstrates a clear supra-arcade downflow in (McKenzie, D.E. & Hudson, H.S. 1999) with a value $V_{out} \approx 100 - 200 kms^{-1}$, which is apparently lower than the expected Alfvén speed. Nevetheless, during solar flares electron energy derived from photo emission can reach tens of keV in the loop-top HXR sites, and reaches few hundreds keV in the footpoint HXR sites. The particle velocity that can generate HXR up to $\geq 100 keV$ is from 10% to $60 \sim 70\%$ speed of light. So what causes the further acceleration after plasmas leave the reconnection site? The electron spectrum from HXR emissions, on the contrary, exhibits a characteristics of nonthermal distribution instead of the original thermal coronal distribution. Then what causes the evolution of particle distribution?

At any rate, a secondary acceleration mechanism should exist between the reconnection site and the HXR emission locations to bridge the observational discrepancy of plasma kinetic energy.

Strong electromagnetic waves, which are generated in magnetic reconnection processes as well as during plasma propagation, have the ability to accelerate particles out of the thermal distribution to the higher nonthermal energy range. Nonthermal particles in solar flares can be accelerated by mainly three mechanisms as was summarized in Chap. 11 of Aschwanden (2006): (1) DC electric field acceleration, (2) stochastic acceleration, and (3) shock acceleration.

(1) DC Electric Field Acceleration

When an electric DC field is applied to a plasma, electrons and ions are accelerated in opposite directions, but the attraction between opposite electric charges causes an impeding electric dragging force or friction, which depends strongly on the ion-collision frequency. However, for large relative velocities the frictional force can become smaller than the accelerating force, and electrons can be accelerated freely out of the thermal

distribution.

The run away velocity of a plasma distribution embedded in an externally-applied electric field E_D is (Knoepfel & Spong 1979)

$$v_r = v_{Te}(\frac{E_D}{E})^{1/2} \tag{1.1}$$

where E_D is the Dreicer electric field (Dreicer 1959) defined as

$$E_D = \frac{q_i ln\lambda}{\lambda_D^2} \tag{1.2}$$

in the above expression $ln\lambda$ is the Coulomb logarithm.

According to the electric field intensity, DC field acceleration can be further subdivided into (1) Sub-Dreicer electric field and (2) Super-Dreicer electric field. Sub-Dreicer acceleration requires large-extended reconnection current sheet to accelerate particle to the observed energy. For the model proposed by Holman (1985), an electric field $E \approx 3 \times 10^{-10}$ (statvolt cm^{-1}) in the current sheet with a typical flare loop size $L \approx 30Mm$ can accelerate electrons to an energy $W \approx 100kev$. This energy gain is sufficient to the observed HXR spectrum.

Practically the sub-Dreicer electric filed model can explain the nonthermal electron distribution in most HXR spectra. But several difficulties are still unsolved in this model, e.g. the stability of the assumed large scale current sheet and the location of the acceleration site. For a large current sheet, small perturbation in the system can cause tearing mode instability (Sturrock 1966) and the current sheet would eventually break into small magnetic islands, as a signature of bursty HXR emission (McAteer et al. 2007). On the other hand if one assumes a large-scale DC electric field between the coronal reconnection site and chromospheric footpoints, the energy-dependent timing of electrons accelerated in this DC electric field contradicts the observed time-of-flight (TOF) delays (Aschwanden & Schwartz 1996). Also, if a static or steady electron beam current is assumed, the return-current cancellation is the problem in many DC electric field models. The return current can limit the acceleration efficiency severely (Brown & Melrose 1977).

The super-Dreicer model which with a more strong DC electric field ($E \gg E_D$) is proposed to overcome the requirement of a large scale current sheet in sub-Deicer model, and the particles can be accelerated to the desired energy level in a raletive short length. This model avoids the difficulties that a large current sheet is unstable for tearing mode instability, and the particle acceleration time is much shorter than the propagation time, which satisfies the observed TOF delays from flare HXR emissions. However the exact mechanism that can generate such a strong electric field ($E_\parallel = 10Vcm^{-1}$ for a length $L = 10^2cm$) in the reconnection outflow region is still an unknown.

Other DC electric field acceleration mechanisms are also proposed, e.g., the model of field-aligned electric potential drops. Electric potential drops can be caused in many ways, and one of the possibilities is that the potential drop is created by the field aligned electrostatic double-layers (DLs). Electrostatic double-layer is basically a demonstration of charge seperation in plasma. A strong electric field locates in the center of this structure to sustain the charge seperation and creates a net potential. Generally a solar flare is difficult to be described by only a single double-layer because such strong electric field requires

a very strong current density. The bulk velocity of the required current should be much higher than its thermal velocity, which is difficult to be generated in reconnection outflow (Volwerk 1993). Consequently the acceleration by many double-layers is proposed to overcome this difficulty. Basically plasma acceleration by several weak double-layer is a stochastic process, hence a higher energy particle requires a longer time to be accelerated. Therefore the drawback of this model, like other earlier mentioned models, is the inevitable inconsistency with the TOF delay of HXR observations.

(2) Stochastic Acceleration

There is, generally, a broadband spectrum of waves present in plasma environment, some waves will have constructive interference and others have destructive interference with the gyromotion of the charged particles and with the local plasma oscillation. The energy transfer between broadband waves and particles can be described as a stochastic process. In this mechanism the interactions of wave and charge particles is a random collision process, hence some parts of particle distribution experience a net energy gain while some parts are slowed down via the same interactions. The efficiency of the most proposed stochastic acceleration models depends on the turbulent level of background waves, and the accelerations are primarily caused by the resonance of particles with various modes of electromagnetic or electrostatic waves.

In general the concept of stochastic acceleration has several advantages over the previous DC electric field acceleration. First, since wave-particle interaction is a microscopic process, it can be averaged out in a macroscopic scale, the compensation of charge neutrality by return current is not necessary. Second, as long as the turbulent region is large enough for sufficient wave-particle interaction, any energy level of charge particles can be reached via this mechanism, i.e. there is no energy limit on the particle acceleration.

Nevertheless, there are also some drawbacks of this model. The primary problem is the origins of the high level electromagnetic wave turbulence. The turbulence level in solar sorona is almost impossible to measure, therefore the observed spectra can be reproduced with an arbitrarily tune on the assumed perturbation level. Also, the primary controversy of this model is that the stochastic acceleration does not satisfy the TOF delay observation, which demands a coherent acceleration of particles in all energy range and it possibly is the most important judgement of the applicable acceleration mechanisms.

(3) Shock Acceleration

Particle acceleration in shock structures has been theoretically and observationally investigated and became a well-established astrophysical acceleration mechanism for high-energy particles. Shocks are nonlinear waves that are generated by the steepening mechanism from the original linear waves (i.e. perturbation level is smaller than background values). Suppose the bulk velocity of a plasma flow is higher than the characteristic speeds of ambient plasma, the waves fronts of the upward propagating waves accumulate in the direction of upstream and become steepened at a certain distance away from the wave sources. To have the sources of wave generation, obstacles of plasma flow are usually required for the shock formation in natural environment. Shock theory tells us that entropy increases across a shock, and the entropy increase becomes greater as the shock strength increases. This is the main difference of a shock from the ordinary waves, of which the entropy does not change, then a wave is basically a reversible process.

Shock acceleration is also called Fermi acceleration. For particles that cross a shock once, this process is also called 'shock drift acceleration', which is a first-order Fermi

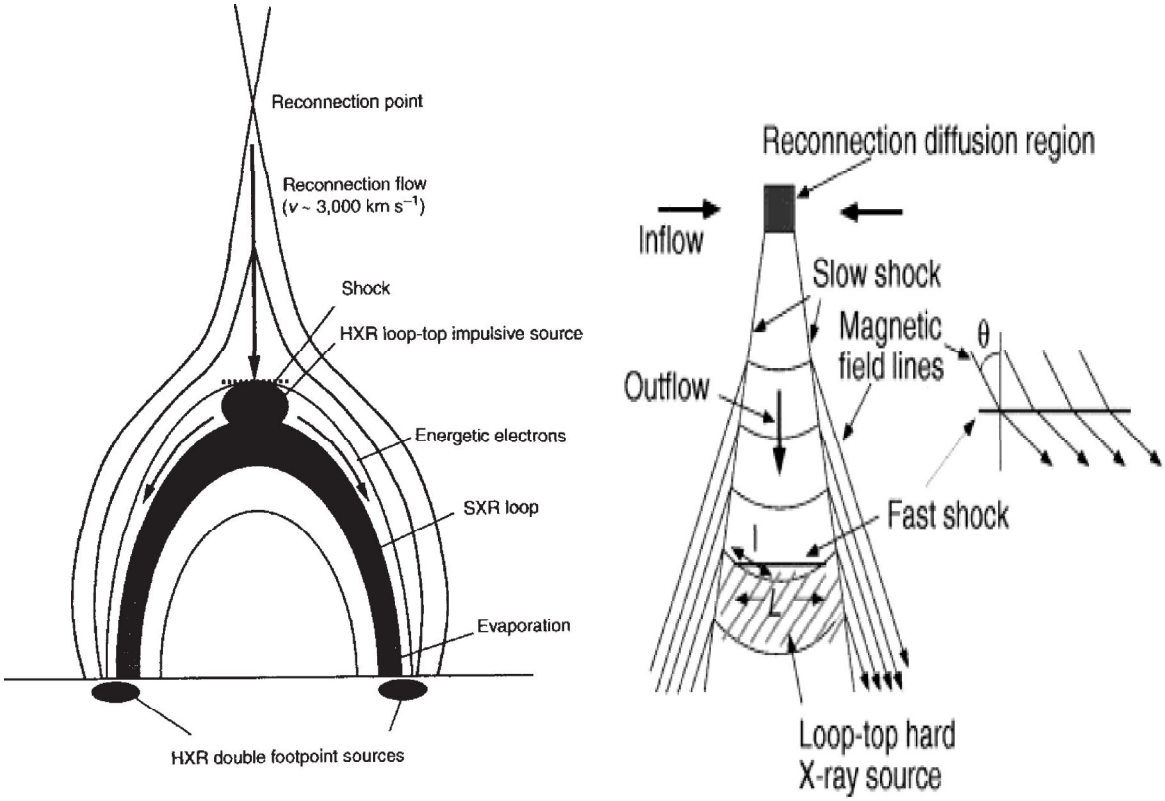

Figure 1.6: Standard model of HXR emission in solar corona (Masuda et al. 1994) and the shock geometry in the reconnection outflow region (Tsuneta & Naito 1998).

acceleration process. While particles that are scattered multiple times across a shock structure experience diffusive shock acceleration, or sometimes is called as 'shock surfing acceleration'. The latter type of diffusive shock acceleration is not much different from stochastic acceleration (Jones 1994), which is a second-order Fermi acceleration process.

The shock acceleration of solar energetic particles events (SEPs) was first proposed by Wild et al. (1963) who interpreted the metric type II burst as evidence for a coronal shock wave (Kallenrode 2003). With the magnetic field topology deduced from observation, Masuda et al. (1994) suggested that the looptop HXR source is a demonstration of fast magnetosonic shock, and this shock generated the observed footpoints and looptop high energy electrons (see Fig. 1.6 left).

Fermi acceleration has been applied to solar flare loops that trap high-energetic protons (Bai et al. 1983), as well as to reconnection outflows in solar flares (Somov & Kosugi 1997, Tsuneta & Naito 1998). The geometry of the later model is demonstrated in Fig. 1.6 (right). Except the intermediate shocks, which is difficult to be observed but theoretically exists, fast shock and slow shock are proposed as efficient accelerators for the observed high energy particles in solar flares (Hoshino 2002, Kuramitsu 2005, Shiota 2005).

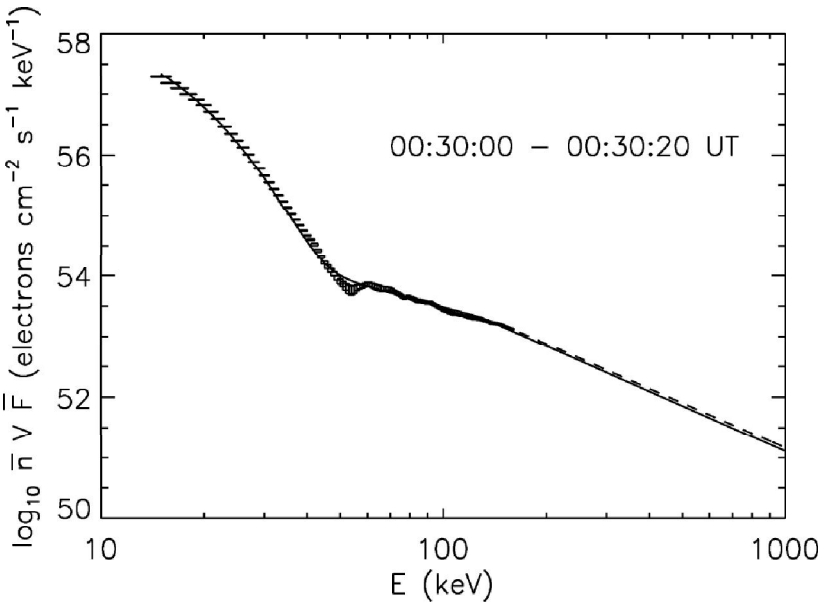

Figure 1.7: The basic broken power-law. A low-energy spectrum is consistent with a multi-thermal plasma with a broad temperature distribution, while the high energy spectrum is consistent with a non-thermal distribution (Piana 2003)

1.3.2 Particle Transport: Formation of Broken-Power-Law Spectrum

The two dimensional magnetohydrodymanics simulation (2D MHD) of the reconnection, which mimic the solar corona during flare, has revealed the exsistence of a fast magnetosonic shock sandwiched by two slow shocks in the reconnection outflow region (Shiota 2005). The dependence on heat conductivity of the physical variables in the outflow region, such as temperature, density, and velocity, are studied by Yokoyama & Shibata (1997). Plasma heating on the downstream side of fast shock is confirmed and believed to be the loop-top HXR source of flare.

The one dimentional particle-in-cell simulation (1D PIC) confirms the exsitence and efficiency of the fast magnetoshonic shock (Wu 1984). The shock surfing acceleration is found competent to produce the suprathermal electrons occurred in the shock transition region, where a series of largeamplitude electrostatic solitary waves (ESWs) are excited by Buneman instability under the interaction between the reflected ions and the incoming electrons (Hoshino 2002). Krauss-Varban (1989) have shown that the fast Fermi process in the de Hoffman-Teller frame (HTF) is equivalent to shock drift acceleration (SDA) in the normal incidence frame (NIF) where the upstream velocity is parallel to the shock normal.

The mentioned PIC simulations (Wu 1984) used the reflective boundary condition, which intended to represent the SXR loops that results in the waves and plasmas reflections. However the total reflective boundary can not include the skin depth effects of SXR loops and the real modification on acceleration from this effect is still an unknown.

The possible fast shock acceleration of plasma of the loop top HXR emission and the

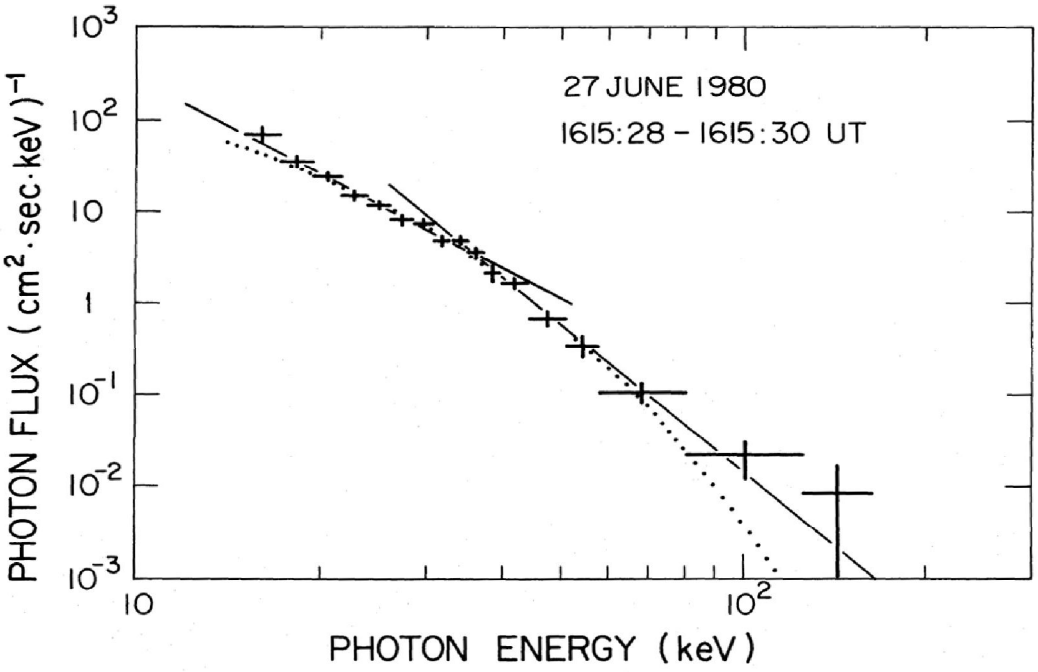

Figure 1.8: A broken power-law spectrum with a flattening in low-energy ($\leq 30keV$) range (Lin and Schwartz 1987).

explanation of coronal loop footpoints spectrum will be discussed in Chap. 4

The SMM measurements with HXRBS and GRS demonstrated that there are flare events in which the observed emission spectrum in the $20keV - 20MeV$ photon energy range cannot be described by a single-power-law function (Dennis 1988, Vestrand 1988, McTiernan & Petrosian 1991, Li 1995). The spectrum usually exhibits a harder tendency in the higher energy part than that of the lower energy range (Piana 2003). The space-averaged HXR spectrum of the broken-power law with a typical high energy hardening can be seen in Fig. 1.7. However, there are also numbers of observations that report the 'flattening of the spectrum' in the low energy range below $30keV$ (Lin and Schwartz 1987), as shown in Fig. 1.8. The fact that two or more indices are required for the spectrum fit indicates the observed emission via bremsstralung is caused by different population of high energy particles, or can it be a result of distribution evolution by a certain particle transport mechanism?

The observed 'broken' spectrum in the hard X-ray range can be formed as a result of superposition of radiation from two sources, each of which has its own 'single' power law spectrum and, perhaps, other differing parameters. However, the possible existence of an electron population with a 'broken' energy spectrum, resulting from the flare acceleration process, should also be considered (Lin and Schwartz 1987).

According to the latest TOF observations by Aschwanden & Schwartz (1996), the plasma acceleration time should be much shorter than the transport time, and the observation of subsecond pulses in hard X-rays suggests that particles of all energies are synchronized before they 'exit' the acceleration region. The proposed injection mechanism gives a physical picture that, supposed that we can put a probe at the exit of acceleration, the plasma distribution is a nonthermal or single power law, hence it is interesting to as-

certain the possibility if the broken power law is a natural result of particle transport in solar corona.

There are a number of literatures addressing on the return current influences of the particle transport in coronal loops (Karlicky 1993, Zharkova 1997, Bogachev & Somov 2007). These models discussed the effects of return-current-caused particle acceleration (Boswell 2006), and also the effects of magnetic mirror trap (Zharkova 2005), and the eventually resulted particle distribution evolution. However, with the inferred TOF observation the acceleration might not be so practical for observed broken power law HXR spectrum. Return current is necessary for the charge and current neutrality conservation in coronal loops, and the influence of the beam-generated return-current should be essential for the particle dynamics during the propagation.

Therefore, for plasma transport research we start from the instability-generated anomalous resistivity in a current carrying system. In Chap. 3 the influence of anomalous transport caused by electrostatic phase space structures will be addressed, and nonlinear estimation of the generated anomalous resistivity in a current system will be given therein. For the plasma transport in the collisionless coronal loop environment, the influence of return current on particle distribution evolution and the associated rich plasma physics will be discussed in Chap. 5.

2 Plasma Stability Analysis

2.1 Plasma Description in Multi-Fluid Limit

Charge seperation and the unilateral motion of single species in a plasma system play important roles in the wave and particle dynamics of the high frequency range ($\omega \ll \omega_{MHD}$) and also short wave length limit ($\lambda \ll \lambda_{MHD}$), and those special characteristics could account for many influential plasma instabilities which are out of the description of magnetohydrodynamics (MHD). To study the instability in warm magnetized plasma with relative drifts between different species, a set of multifluid equations for different species with Maxwell's equations are required (in cgs units) to formulate this system.

$$\frac{\partial N_j}{\partial t} + \nabla \cdot (N_j \vec{V}_j) = 0 \tag{2.1}$$

$$\frac{\partial \vec{V}_j}{\partial t} + \vec{V}_j \cdot \nabla \vec{V}_j + \frac{\nabla P_j}{m_j N_j} = \frac{e_j}{m_j}(\vec{E} + \frac{\vec{V}_j \times \vec{B}}{c}) \tag{2.2}$$

$$\frac{dP_j}{dt} = S_j^2 \frac{d}{dt}(m_j N_j) \tag{2.3}$$

$$\nabla \cdot \vec{B} = 0 \tag{2.4}$$

$$\nabla \cdot \vec{E} = 4\pi \sum e_j N_j \tag{2.5}$$

$$\nabla \times \vec{E} = -\frac{1}{c}\frac{\partial \vec{B}}{\partial t} \tag{2.6}$$

$$\nabla \times \vec{B} = \frac{4\pi}{c} \sum e_j N_j \vec{V}_j + \frac{1}{c}\frac{\partial \vec{E}}{\partial t} \tag{2.7}$$

In the system described above there are 11 physical quantities as free variables. The number density of species j, N_j, the three velocity components, V_{jx}, V_{jy}, V_{jz}, the thermal

pressure P_j, three magnetic field components B_x B_y B_z and three electric field components E_x E_y E_z. To have a self-consistent system, the number of physical equations should agree with the number of physical unknowns. In principle equation (2.4) is equivalent to equation (2.6), since a divergence of any vector-field curl is always zero ($\nabla \cdot (\nabla \times \vec{A}) = 0$). Taking divergence on equation (2.6) and (2.7), we found that they are equally defined already in equations (2.4) and (2.5). Hence we have two scalar equations, equations (2.1) and (2.3), and three triple-vertor equations, the equation (2.2), (2.6) and (2.7). In this multifluid system there are 11 unknowns with 11 equations, therefore this is a self-consistent solvable system.

Note that plasma environment we considered, the solar corona, has a low plasma number density that the collision cross sections of each species are small. The mean-free-path of coronal plasma is about one astronomical unit ($1AU$), hence the binary collision term in momentum equation (2.2) between different species is neglected, i.e. there is no momentum transfer via collisions. In a multifluid collisionless plasma, the interactions among species are correlated through the total electric field $\vec{E}$ and total magnetic field $\vec{B}$ that are generated by charge and current spatial distributions.

To analyze the system stability, we use the perturbation theory to divide every physical quantities into a background term with a small distrubance ($Q = Q_0 + q_1$). In homogeneous environment condition, the small perturbation term can be expressed as a propagating wave, which is of the form: $\exp i(\vec{K} \cdot \vec{r} - \omega t)$. Here $K = 2\pi/\lambda$ is the wave number of a specific Fourier wave component that has frequency $\omega = 2\pi\nu$. The linearized multifluid equations then are

$$n_j = N_j \frac{\vec{K} \cdot \vec{u}_j}{\omega_{*j}} \tag{2.8}$$

$$\omega_{*j}^2 \vec{u}_j - S_j^2 \vec{K}(\vec{K} \cdot \vec{u}_j) - i\omega_{*j} \frac{e_j}{m_j}(\delta\vec{E} + \frac{\vec{U}_j \times \vec{b}}{c}) - i\omega_{*j}\vec{u}_j \times \vec{\Omega}_j = 0 \tag{2.9}$$

$$\frac{e_j}{m_j}\delta\vec{E} = \frac{ic^2{\omega_{pj}}^2}{\alpha\omega\sigma_j}(\vec{K}\vec{K} \cdot - \frac{\omega^2}{c^2})\vec{j} \tag{2.10}$$

$$\frac{e_j}{m_j}\vec{b} = -\frac{ic{\omega_{pj}}^2}{\alpha\sigma_j}(\vec{K} \times \vec{j}) \tag{2.11}$$

$$\vec{j} = \sum_j \sigma_j(\vec{u}_j + \vec{U}_j \frac{\vec{K} \cdot \vec{u}_j}{\omega_{*j}}) \tag{2.12}$$

where the notations σ_j, ω_{*j} and α are defined as below

$$\sigma_j = N_j e_j \tag{2.13}$$

$$\omega_{*j} = \omega - \vec{K} \cdot \vec{U}_j \tag{2.14}$$

$$\alpha = \omega^2 - c^2 K^2 \tag{2.15}$$

Equation (2.10) is the wave equation which is used to solve dispersion relation, and it is also expressed as

$$(\frac{c^2}{\omega^2}\vec{K}\vec{K} - \frac{c^2K^2}{\omega^2}\underline{\underline{I}}) \cdot \delta\vec{E} + \underline{\underline{I}} \cdot \delta\vec{E} + i\frac{4\pi}{\omega}\vec{j} = 0 \tag{2.16}$$

where $\underline{\underline{I}}$ is a unit tensor. To obtain the dispersion relation we replace the terms $\vec{u}_j$ and $\vec{K} \cdot \vec{u}_j$ in equation (2.12) by an inner product of a tensor with $\delta\vec{E}$, then replace the term $\vec{j}$ in equation (2.16). The detailed derivation can be found in appendix A, here we just use the derived results after a complicated algebra.

$$(\vec{K} \cdot \vec{u}_j) = \frac{i\omega_{*j}\frac{e_j}{m_j}\left[\vec{K} + \frac{K^2}{\omega}\vec{U}_j - \frac{(\vec{K}\cdot\vec{U}_j)}{\omega}\vec{K} + \frac{i(\vec{K}\cdot\vec{U}_j - \omega)(\vec{K}\times\vec{\Omega}_j)}{\omega_{*j}\omega} + \frac{(\vec{K}\cdot\vec{\Omega}_j)\vec{\Omega}_j}{\omega_{*j}^2}\right] \cdot \delta\vec{E}}{\omega_{*j}^2 - S_j^2K^2 + \frac{S_j^2(\vec{K}\cdot\vec{\Omega}_j)^2}{\omega_{*j}^2} - \Omega_j^2} \tag{2.17}$$

$$\begin{aligned}(\omega_{*j}^2 - \Omega_j^2)\vec{u}_j = &\left(S_j^2\vec{K} + i\frac{S_j^2}{\omega_{*j}}(\vec{K}\times\vec{\Omega}_j) - \frac{S_j^2}{\omega_{*j}^2}(\vec{K}\cdot\vec{\Omega}_j)\vec{\Omega}_j\right)(\vec{K}\cdot\vec{u}_j) + \\ &\left[i\omega_{*j}\frac{e_j}{m_j}\left(\underline{\underline{I}} + \frac{\vec{K}\vec{U}_j}{\omega} - \frac{\vec{U}_j\cdot\vec{K}}{\omega}\underline{\underline{I}}\right) - \frac{e_j}{m_j}\left(\frac{(\vec{K}\times\vec{\Omega}_j)}{\omega}\vec{U}_j + i\frac{\vec{\Omega}_j\vec{\Omega}_j}{\omega_{*j}}\right)\right]\cdot\delta\vec{E} \\ &+\frac{e_j}{m_j}(1 - \frac{\vec{K}\cdot\vec{U}_j}{\omega})\underline{\underline{A}}\cdot\delta E\end{aligned} \tag{2.18}$$

where

$$\begin{pmatrix} 0 & -\Omega_{zj} & \Omega_{yj} \\ \Omega_{zj} & 0 & -\Omega_{xj} \\ -\Omega_{yj} & \Omega_{xj} & 0 \end{pmatrix} \cdot \delta\vec{E} = 0; \underline{\underline{A}} \cdot \delta\vec{E} = \vec{\Omega}_j \times \delta\vec{E}$$

replace $\vec{K} \cdot \vec{u}_j$ and $\vec{u}_j$ in equation (2.17) and (2.18) to (2.16), the wave equation can be expressed as

$$\left\{(\frac{c^2}{\omega^2}\vec{K}\vec{K} - \frac{c^2K^2}{\omega^2}\underline{\underline{I}}) + \underline{\underline{I}} - \sum_j \frac{\omega_{*j}\omega_{pj}^2}{\omega}\right. \tag{2.19}$$

$$\left[\frac{\vec{U}_j}{\omega_{*j}}+\frac{(S_j^2\vec{K}+i\frac{S_j^2}{\omega_{*j}}(\vec{K}\times\vec{\Omega}_j)-\frac{S_j^2}{\omega_{*j}^2}(\vec{K}\cdot\vec{\Omega}_j)\vec{\Omega}_j)}{\omega_{*j}^2-\Omega_j^2}\right]$$

$$\left[\frac{(\frac{\omega_{*j}}{\omega}\vec{K}+\frac{K^2\vec{U}_j}{\omega}-i\frac{(\vec{K}\times\vec{\Omega}_j)}{\omega}-\frac{(\vec{K}\cdot\vec{\Omega}_j)\vec{\Omega}_j}{\omega_{*j}^2})}{\omega_{*j}^2-S_j^2K^2+\frac{S_j^2(\vec{K}\cdot\vec{\Omega}_j)^2}{\omega_{*j}^2}-\Omega_j^2}\right]$$

$$+\sum_j i\frac{\omega_{pj}^2}{\omega}\left[\frac{i\omega_{*j}(\frac{\omega_{*j}}{\omega}\underline{\underline{I}}+\frac{\vec{K}\vec{U}_j}{\omega})-(\frac{(\vec{K}\times\vec{\Omega}_j)}{\omega}\vec{U}_j+i\frac{\vec{\Omega}_j\vec{\Omega}_j}{\omega_{*j}})+\frac{\omega_{*j}}{\omega}\underline{\underline{\Lambda}}}{\omega_{*j}^2-\Omega_j^2}\right]\Bigg\}\cdot\delta\vec{E}=0$$

This is the general dispersion relation of a multifluid plasma, in which a warm magnetized plasma with bulk velocity of each species is considered. No further assumptions are made except the drift velocity is parallel to the background magnetic field ($\vec{B}//\vec{U}$).

To find the eigen solutions of this governing equation, we look for a set of specific $\vec{K}$ and ω that makes the determinant of the leading tensor zero. We expand the leading tensor in equation (2.19) into a nine-components format.

$$\begin{pmatrix} a_1 & a_2 & a_3 \\ b_1 & b_2 & b_3 \\ c_1 & c_2 & c_3 \end{pmatrix}\cdot\delta\vec{E}=0$$

Eigen values are found when the condition that the determinant is equal to zero is satisfied.

$$\left|\begin{pmatrix} a_1 & a_2 & a_3 \\ b_1 & b_2 & b_3 \\ c_1 & c_2 & c_3 \end{pmatrix}\right|=0$$

Without losing the generality we set a geometry with the magnetic field $\vec{B}=B_0\hat{z}$ and the wave vector $\vec{K}=K_x\hat{x}+K_z\hat{z}$. To look for a compact expression and a symmetric form of the off-diagonal terms, the tensor can be rearranged as

$$\begin{pmatrix} K_{xx}-n^2cos^2\theta & K_{xy} & K_{xz}+n^2cos\theta sin\theta \\ K_{yx} & K_{yy}-n^2 & K_{yz} \\ K_{zx}+n^2cos\theta sin\theta & K_{zy} & K_{zz}-n^2sin^2\theta \end{pmatrix}\cdot\delta\vec{E}=0 \tag{2.20}$$

where $n=Kc/\omega$ is the index of refraction, θ is the angle between wave vector $\vec{K}$ and magnetic field $\vec{B}$. The nine-components of dielectric tensor $\underline{\underline{K}}$ are

$$K_{xx}=1-\sum_j\left[\frac{\omega_{pj}^2\omega_{*j}^2(\omega_{*j}^2-S_j^2K^2cos^2\theta)}{\omega^2[\omega_{*j}^2(\omega_{*j}^2-S_j^2K^2)-\Omega_j^2(\omega_{*j}^2-S_j^2K^2cos^2\theta)]}\right]$$

$$K_{yx}=\sum_j\left[\frac{i\omega_{pj}^2\Omega_j\omega_{*j}(\omega_{*j}^2-S_j^2K^2cos^2\theta)}{\omega^2[\omega_{*j}^2(\omega_{*j}^2-S_j^2K^2)-\Omega_j^2(\omega_{*j}^2-S_j^2K^2cos^2\theta)]}\right]$$

$$K_{zx} = -\sum_j \left[\frac{\omega_{pj}^2 \omega_{*j}^2 S_j^2 K^2 sin\theta cos\theta}{\omega^2[\omega_{*j}^2(\omega_{*j}^2 - S_j^2 K^2) - \Omega_j^2(\omega_{*j}^2 - S_j^2 K^2 cos^2\theta)]} \right]$$

$$K_{xy} = -\sum_j \left[\frac{i\omega_{pj}^2 \Omega_j \omega_{*j}(\omega_{*j}^2 - S_j^2 K^2 cos^2\theta)}{\omega^2[\omega_{*j}^2(\omega_{*j}^2 - S_j^2 K^2) - \Omega_j^2(\omega_{*j}^2 - S_j^2 K^2 cos^2\theta)]} \right]$$

$$K_{yy} = 1 - \sum_j \left[\frac{\omega_{pj}^2 \omega_{*j}^2(\omega_{*j}^2 - S_j^2 K^2)}{\omega^2[\omega_{*j}^2(\omega_{*j}^2 - S_j^2 K^2) - \Omega_j^2(\omega_{*j}^2 - S_j^2 K^2 cos^2\theta)]} \right]$$

$$K_{zy} = -\sum_j \left[\frac{i\omega_{pj}^2 \Omega_j \omega_{*j} S_j^2 K^2 sin\theta cos\theta}{\omega^2[\omega_{*j}^2(\omega_{*j}^2 - S_j^2 K^2) - \Omega_j^2(\omega_{*j}^2 - S_j^2 K^2 cos^2\theta)]} \right]$$

$$K_{xz} = -\sum_j \left[\frac{\omega_{pj}^2 \omega_{*j}^2 S_j^2 K^2 sin\theta cos\theta}{\omega^2[\omega_{*j}^2(\omega_{*j}^2 - S_j^2 K^2) - \Omega_j^2(\omega_{*j}^2 - S_j^2 K^2 cos^2\theta)]} \right]$$

$$K_{yz} = \sum_j \left[\frac{i\omega_{pj}^2 \Omega_j \omega_{*j} S_j^2 K^2 sin\theta cos\theta}{\omega^2[\omega_{*j}^2(\omega_{*j}^2 - S_j^2 K^2) - \Omega_j^2(\omega_{*j}^2 - S_j^2 K^2 cos^2\theta)]} \right]$$

$$K_{zz} = 1 - \sum_j \left[\frac{\omega_{pj}^2 [\omega_{*j}^2(U_j^2 K^2 + U_j \omega_{*j} K cos\theta + \omega\omega_{*j}) - \Omega_j^2 \omega^2 - S_j^2 \omega_{*j}^2 K^2 sin^2\theta]}{\omega^2[\omega_{*j}^2(\omega_{*j}^2 - S_j^2 K^2) - \Omega_j^2(\omega_{*j}^2 - S_j^2 K^2 cos^2\theta)]} \right]$$

It is interesting to notice the symmetry in the dielectric tensor that, $K_{xy} = -K_{yx}$, $K_{xz} = -K_{zx}$ and $K_{zy} = -K_{yz}$.

2.1.1 Simplified Case: Waves in Cold Plasma

Without an energy souce, such as a relative drift velocity betwen species, there is only plasma oscillation in system, indicating frequency ω is always a real value. However plasma becomes unstable when free energy is supplied and the wave amplitude from small distrubances can grow. To classify various wave modes existing in this system, we start from a simplified case that a cold plasma ($S_j = 0$: sound speed) and zero drift ($\vec{U} = 0$) are assumed. The wave equation (2.20) is reduced to the Altar-Appleton dispersion relation.

$$\begin{pmatrix} S - n^2 cos^2\theta & -iD & n^2 cos\theta sin\theta \\ iD & S - n^2 & 0 \\ n^2 cos\theta sin\theta & 0 & P - n^2 sin^2\theta \end{pmatrix} \cdot \delta\vec{E} = 0 \tag{2.21}$$

The dielectric components S, D and P are reduced to cold plasma forms

$$S = 1 - \sum_j \left[\frac{\omega_{pj}^2}{\omega^2 - \Omega_j^2} \right]$$

$$D = - \sum_j \left[\frac{\omega_{pj}^2 \Omega_j}{\omega(\omega^2 - \Omega_j^2)} \right]$$

$$P = 1 - \sum_j \left[\frac{\omega_{pj}^2}{\omega^2} \right]$$

Eigen modes are found by letting the determinant equal to zero; hence the dispersion relation can be further expanded into a polynomial form

$$An^4 - Bn^2 + C = 0 \tag{2.22}$$

where

$$A = S\,sin^2\theta + P cos^2\theta \tag{2.23}$$

$$B = RL sin^2\theta + PS\,(1 + cos^2\theta) \tag{2.24}$$

$$C = PRL \tag{2.25}$$

Two extra notations used here, $R \equiv S + D$ and $L \equiv S - D$, define the right-handed and left-handed polarized waves, which are respectively efficient at electron and ion cyclotron accelerations perpendicular to the background magnetic field. The dispersion can also be expressed in terms of the angle θ

$$tan^2\theta = -\frac{P(n^2 - R)(n^2 - L)}{(S n^2 - RL)(n^2 - P)} \tag{2.26}$$

For the waves propagating along $\vec{B}_0$ ($\theta = 0$), it demands the numerator of equation (2.26) vanish. Hence there are three wave modes
(a) $P = 0$ (Plasma Oscillations)
(b) $n^2 = R$ (wave with Right-handed polarization)
(c) $n^2 = L$ (wave with Left-handed polarization)

For perpendicular propagation, i.e. $\theta = \pi/2$, the denominator should vanish. There are two waves
(a) $n^2 = P = 0$ (Ordinary wave)
(b) $n^2 = RL/S$ (Extraordinary wave)

The plasma waves in warm plasma are basically the thermal extension of waves in cold plasma limit. The detailed description of pure warm plasma waves without instability can be found in the textbook by Swanson (1989).

2.2 Current Driven Instabilities

Form the kinetic point of view on the plasma stability, a Maxwellian distribution is the only solution of a thermal equlibrium state, or for a less strict constraint, a local thermal equilibrium is required. As the tendency of a natural system, the lowest energy state is always preferred for the direction of system evolution. With a relative drift of different species that comprise the plasma, a free energy source is provided and the plasma distribution is biosed from a thermal equilibrium. In a current carrying system, or sometimes even in a current-free plasma system, several kinds of instabilities can be driven to work collectively to reduce the free energy source back to a marginal stability condition. The physical explanation of the generation of current driven instability is as follow. In collisional condition the lowest energy state, the thermal equlibrium, is achieved when the binary collisions creat the viscosity, or electric resistivity in charged particle envirnment, which converts the drift kinetic energy to thermal energy of each species. In collisionless plasmas, the localized electric fields generated by electrostatic instabilities play the role as obstacles that provides the effective collisions with bulk drifting charged particles. The bulk energy of charged particles is used to amplify the locally generated electrostatic waves, and when the amplitude of these structures is sufficiently large to influence the kinetics of charged particles, an effective electric resistivity is created to bring the plasma environment back to equlibrium.

2.3 The Identical Nature of Ion Acoustic and Buneman Instability

In 1946, Landau (1946) found the Vlasov-Maxwellian equations can be treated and solved as an initial value problem rather than using the Fourier transform by Vlasov (1945). The original difficulty of the occurrence of inconsistent solutions, which is caused by maintaining only the principal values when integrating in the complex velocity space around the sigularity points, is avoided by applying the Laplace transform of the time variable in Vlasov equation (see, e.g. J. Baumjohann (1997)). From the Landau solution with both the ion and electron thermal motions, i.e. $(m_i/m_{el} \neq \infty)$, the ion-acoustic instability is recognized as a wave-particle resonance when the relative bulk velocity of electrons is close to the ion-acoustic speed $c_s = \sqrt{\kappa T_{el}/m_i}$.

Buneman (1958) in the year 1958, with the cold multi-fluid approximation, discovered that the a current-driven instability occurs when the phase velocity of a wave perturbation is close to the electron drift $\omega/k \simeq V_{de}$, and this mode has a collective nature of Coulomb interaction, the so-called Buneman instability. The Buneman instability has been claimed, even in many contemporary works, as an essentially different mode from the ion-acoustic instability (Fredrick 1970, Mantei 1976, Mascheroni 1977, Sato 1980). Some multi-fluid models of warm plasma try to include the Landau resonance effect (Lapuerta 2001) in the energy equation. Having the concept that these two modes are different, sometimes the Buneman and ion-acoustic modes are compared within the same parameter range (Sukovatov 2004). Also with a careless discrepency, the Buneman mode is also misinterpreted as an ion-acoustic mode with its conventional instability criterion $\omega/k \simeq c_s$ (Jovanovic 2004).

We start from a fully kinetic consideration to ascertain the current-driven instability in a different range of electron drift velocity V_{de}. We intend to demonstrate how these two modes share the same wave-particle interaction nature, and they are just the two revealments of the same instability.

Starting from the classical Landau-Laplace procedure (Landau 1946), where the Laplace transform on the time variable t in Vlasov equation has been used rather than the Fourier transform, the solutions of Vlasov equation are contributed by the sum of residues, which demands the dispersion relation become zero.

$$D(\vec{k},\omega) = 1 + \sum_j \frac{\omega_{pj}^2}{k^2} \int_{-\infty}^{\infty} d^3v \frac{\vec{k}\cdot\partial F_j/\partial\vec{v}}{\omega - \vec{k}\cdot\vec{v}} = 0 \tag{2.27}$$

The Laplace transform portrayed that the considered condition is an initial value problem. More importantly the Laplace transform results in a conclusion that the complex velocity space integration should go under the poles (Swanson 1989), and also the principal of causality is reflected explicitly in this transform (Krotscheck 1978, Diaz 1981, Stoof 1993). The wave-particle Landau resonance effect, which is demonstrated as a sigularity in the denominator $(\omega - \vec{k}\cdot\vec{v})$, is expressed when the denominator approaches zero. In particular, the nature of Landau resonance is due to those particles whose velocity nearly matches the wave phase velocity, either thermal velocity or oscillation velocity, and those particles exchanging energy with waves.

The solution of Eq. (2.27) is obtained when a set of frequencies $\omega(k) = \omega_r(k) + i\gamma(k)$ is found with a given $\vec{k}$. According to the residue theory (see, e.g. Arfken (1995)), for the velocity integration containing sigularities, there are three possible integration paths, depending on the location of sigularities in the complex velocity space.

The three possible paths are: (1) $\gamma > 0$ instability, (2) $\gamma < 0$ damping and (3) $\gamma = 0$ wave. Then the element of integration in Eq. (2.27) can be expressed as

$$\frac{\omega_{pj}^2}{k^2}\int_{-\infty}^{\infty} d^3v \frac{\vec{k}\cdot\partial F_j/\partial\vec{v}}{\omega - \vec{k}\cdot\vec{v}} = \frac{\omega_{pj}^2}{k^2}\begin{cases} \displaystyle\int_{-\infty}^{\infty} d^3v \frac{\vec{k}\cdot\partial F_j/\partial\vec{v}}{\omega - \vec{k}\cdot\vec{v}}, & \gamma > 0 \Leftarrow \text{path (1)} \\ \displaystyle P\int_{-\infty}^{\infty} d^3v_r \frac{\vec{k}\cdot\partial F_j/\partial\vec{v}}{\omega - \vec{k}\cdot\vec{v}} + 2\pi i \frac{\partial F_j}{\partial\vec{v}}\Big|_{\frac{\omega}{k}=v}, & \gamma < 0 \Leftarrow \text{path (2)} \end{cases}$$

We are not interested in pure wave behavior here, i.e., $\gamma = 0$, then two integration results of Landua contour are shown in the above expression. For instability, the imaginary part of frequency is positive, therefore the pole in the contour is in the upper plane of velocity integration, and the whole integration stays the same. However, if we expect damping to take place, i.e. the imaginary part of frequency is negative, the integration then consists two parts, the pricipal integration along real velocity axis and the residues of sigularity poles in the lower plane of velocity integration. Because before starting solve $D(\vec{k},\omega) = 0$, there is no way to know the imaginary part γ is positive or negative, we have to select the expected phenomena is either instability $\gamma > 0$ or damping $\gamma < 0$. With the selected integration path, we obtain a set of $\omega(k) = \omega_r(k) + i\gamma(k)$ by solving Eq. (2.27).

The most important step then is to check if the obtained $\omega(k) = \omega_r(k) + i\gamma(k)$ satisfies our path selection. If the obtained growth rate is $\gamma(k) < 0$ from integration path (1), which obviously violates the assumption, we may conclude that only the assumption (2) and

path (2) are true for the specific $\vec{k}$ in the plasma setup. By the same token, the obtained growth rate $\gamma(k) > 0$ is only true for assumption (1) and integration path (1). Though it is sometimes misinterpreted, the significance of the Landau contour should be addressed at this point. The integration either along path (1) or path (2) is a complete expression of kinetic theory and it is equivalent to the original velocity integration in Eq. (2.27), and the whole information of **Landau resonance** is preserved.

With the merit of Taylor expansion on the above Cauchy integral, the Landau contour integration can also be expressed in terms of *plasma dispersion function* $Z(\xi_j)$, which is sometimes also called *Fried-Conte function* because Fried and Conte first tabulated in 1961. Assume a Maxwellian distribution function for every species in plasma.

$$F_j(\vec{v}) = \left(\frac{m_j}{2\pi T_j}\right)^{3/2} exp\left(-\frac{m_j}{2T_j}(\vec{v} - \vec{V}_j)^2\right)$$

The velocity integration in original dispersion relation Eq. (2.27) is expressed as

$$\frac{\omega_{pj}^2}{k^2}\int_{-\infty}^{\infty} d^3v \frac{\vec{k}\cdot\partial F_j/\partial\vec{v}}{\omega - \vec{k}\cdot\vec{v}} = \frac{2\omega_{pj}^2}{k^2 v_{Tj}^2}\left[1 + \xi_j Z(\xi_j)\right]$$

where

$$Z(\xi_j) = \pi^{-1/2}\int_{\infty}^{-\infty} dx \frac{exp(-x^2)}{x - \xi_j}; \qquad \xi_j = \frac{\omega - \vec{k}\cdot\vec{V}_j}{k v_{Tj}}$$

For a quasi-cold plasma ($v_{Tj} \approx 0$, hence $\xi_j \geq 1$) in plasma dispersion function $Z(\xi_j)$, the plasma dispersion function $Z(\xi_j)$ for species j is expanded as

$$Z(\xi_j) \simeq \left[-\frac{1}{\xi_j} - \frac{1}{2\xi_j^3} - \frac{3}{4\xi_j^5} - ...\right] + \sigma\pi^{1/2} i exp(-\xi^2) \tag{2.28}$$

where σ depends on the location of sigularity poles that exists in the upper or lower plane of complex velocity space.

$$\sigma = \begin{cases} 0, & \gamma > 0 \quad \Leftarrow \text{Instability} \\ 1, & \gamma = 0 \quad \Leftarrow \text{Wave} \\ 2, & \gamma < 0 \quad \Leftarrow \text{Damping} \end{cases}$$

Replacing the velocity integration of distribution by the expansion of Fried-Conte function $Z(\xi_j)$, we obtain the general electrostatic dispersion relation.

$$D(k, \omega_r + i\gamma) = 1 + \frac{2\omega_{pi}^2}{k^2 v_{Ti}^2}[1 + \xi_i Z(\xi_i)] + \frac{2\omega_{pe}^2}{k^2 v_{Te}^2}[1 + \xi_e Z(\xi_e)] = 0 \tag{2.29}$$

This is the *general kinetic dispersion relation* for electrostatic perturbations, i.e. it can be applied to instability, wave or damping cases. To point out the nature of wave-particle interaction, indeed, the term "Landau damping" is used for situations when the growth rate $\gamma(k) < 0$, i.e. the damping cases. Nevertheless, the general term "Landau resonance" describes the wave-particle interaction when the wave with phase-velocity $V_{ph} = \omega/k$ is

equal to particle velocity, therefore it applies to any value of growth rate $\gamma(k)$, instability or damping.

It is well-known that under thermal equilibrium condition all waves will tend to damp out. However, if there is one species of plasma flow through another species, the distribution function is deflected from equilibrium and phase-space instability is supposed to appear and draw the plasma distribution back to original thermal equilibrium state. With the interest of instability in plasma, the velocity integration along path (1) is chosen and the coefficient σ in Eq. (2.28) is equal to zero as a natural consequence that all poles locate in the upper plane.

Ion acoustic wave becomes unstable when the electron bulk velocity (drift) is larger than ion sound wave. And through Landau resonance effect, the thermal electrons which have similar velocity as ion sound velocity give their kinetic energy and contribute to the wave amplification.

However from fluid approach, O. Buneman in 1958 discovered the famous fluid-like electrostatic streaming instability. The Buneman instability was identified by O. Buneman with a consideration of collective Coulomb interaction (which is determined, small-angle collision) between plasma particles, since the colse (large-angle) collisions are rare. Hence via this process, the kinetic energy of electron bulk motion can be converted into wave fluctuation energy. With the consideration of a collective Coulomb interaction, the cold plasma assumption was made, then the dispersion relation proposed by Buneman from fluid equation is

$$D(k, \omega_r + i\gamma) = 1 - \frac{\omega_{pi}^2}{\omega^2} - \frac{\omega_{pe}^2}{(\vec{k} \cdot \vec{V}_{de} - \omega)^2} = 0 \tag{2.30}$$

The cold plasma assumption, on the other hand, is equivalent to the condition when electron drift is much larger than its thermal velocity.

From kinetic point of view, plasma with temperature indicates particle can move randomly and have statistically a Maxwellian distribution. However in cold ummagnetized plasma limit, the only motion that plasma charged particle experiences is the harmonic oscillation at the plasma frequency $\omega_{pj} = (4\pi n_j e^2/m_j)^{1/2}$, independent of the wave length. Equations (2.29) and (2.30) explain the limits of wave-particle energy exchange mechanism for a partial range in velocity distribution or a collective Coulbomb interaction of plasma species. This limit approach gives a mistaken impression that the Buneman instability, which is derived from the cold fluid equations in Eq.(2.30), is different from the kinetic ion-acoustic instability essentially. In order to verify that the fluid-like Buneman instability is also caused by kinetic Landau resonance, we should start from kinetic theory, the kinetic dispersion relation Eq.(2.27).

For current driven instabilities we consider two species, the drifting electrons and background ions. We preserve the first two terms in the dispersion function expansion Eq.(2.28), and this process mimics the fact that the thermal velocity is very small compared to any wave phase velocity and drift velocity, i.e. the cold plasma approximation. The ion and electron elements in Eq. (2.29) can be approximated as

$$1 + \xi_i Z(\xi_i) \approx 1 + (-1 - \frac{1}{2\xi_i^2}) = -\frac{1}{2\xi_i^2} \tag{2.31}$$

$$1 + \xi_e Z(\xi_e) \approx 1 + (-1 - \frac{1}{2\xi_e^2}) = -\frac{1}{2\xi_e^2} \tag{2.32}$$

where

$$\xi_i = \frac{\omega}{kv_{Ti}}; \xi_e = \frac{\omega - \vec{k} \cdot \vec{V}_e}{kv_{Te}}$$

The distribution functions of the drifting electrons and background ions are as follows.

$$F_e(\vec{v}) = \left(\frac{m_e}{2\pi T_e}\right)^{3/2} exp\left(-\frac{m_e}{2T_e}(\vec{v} - \vec{V}_e)^2\right) \tag{2.33}$$

$$F_i(\vec{v}) = \left(\frac{m_i}{2\pi T_i}\right)^{3/2} exp\left(-\frac{m_i}{2T_i}v^2\right) \tag{2.34}$$

With the distributions in Eqs. (2.33) and (2.34), the normalized Doppler-shifted phase-velocity ξ_i and ξ_e in Eqs. (2.31) and (2.32) can be now replaced in Eq. (2.29). Then we have

$$\begin{aligned} D(k, \omega_r + i\gamma) &= 1 + \frac{2\omega_{pi}^2}{k^2 v_{Ti}^2}(-\frac{k^2 v_{Ti}^2}{2\omega^2}) + \frac{2\omega_{pe}^2}{k^2 v_{Te}^2}(-\frac{k^2 v_{Te}^2}{2(\omega - \vec{k} \cdot \vec{V}_e)^2}) \\ &= 1 - \frac{\omega_{pi}^2}{\omega^2} - \frac{\omega_{pe}^2}{(\vec{k} \cdot \vec{V}_e - \omega)^2} = 0 \end{aligned} \tag{2.35}$$

Apparently, the above equation has the same expression as the one proposed by Buneman (1958). Hence, it proves that the Buneman instability is just the ion-acoustic instability in cold plasma limit, which demands the thermal velocity is much less than electron bulk velocity ($V_{te} \ll V_{de}$) and the Landau resonance effect is also preserved.

Although it has been claimed that no Landau resonance effect in fluid-like Buneman instability (Lapuerta 2001, Melrose 1986, Ahedo 2001), the misinterpretation should be corrected. From kinetic point of view, Landau resonance occurs due to the energy exchange between a wave with phase velocity $V_{ph} = \omega/k$ and particles in the plasma with velocity approximately equal to V_{ph}, either the particle thermal velocity or the plasma oscillation velocity of simple harmonic motion. The Landau resonance of ion-acoustic instability describes that the wave resonates with the particles of same themal velocity, while the Landau resonance of Buneman instability indicates the wave resonates with the particles with Langmuir oscillating velocity.

In cold plasma case, any perturbation will cause the particles to oscillate at the plasma frequency $\omega_{pj} = (4\pi n_j e^2/m_j)^{1/2}$, independent of the wave number k (or wavelength λ). The phase velocity of waves differs according to individual wave number, although the group velocity is zero. Buneman instability takes place when there is a bulk motion of electrons. From Eq. (2.35) and Fig. (2.1) we can see that the instability is caused by the phase-mixing of the backward-propagating electron Langmuir wave and ion Langmuir oscillation. The wave-particle interaction process is as follows. When a perturbation appears in this current carrying system, mathematically the perturbation can be decomposed into waves of different wavelength, although for ions the frequency is always ion

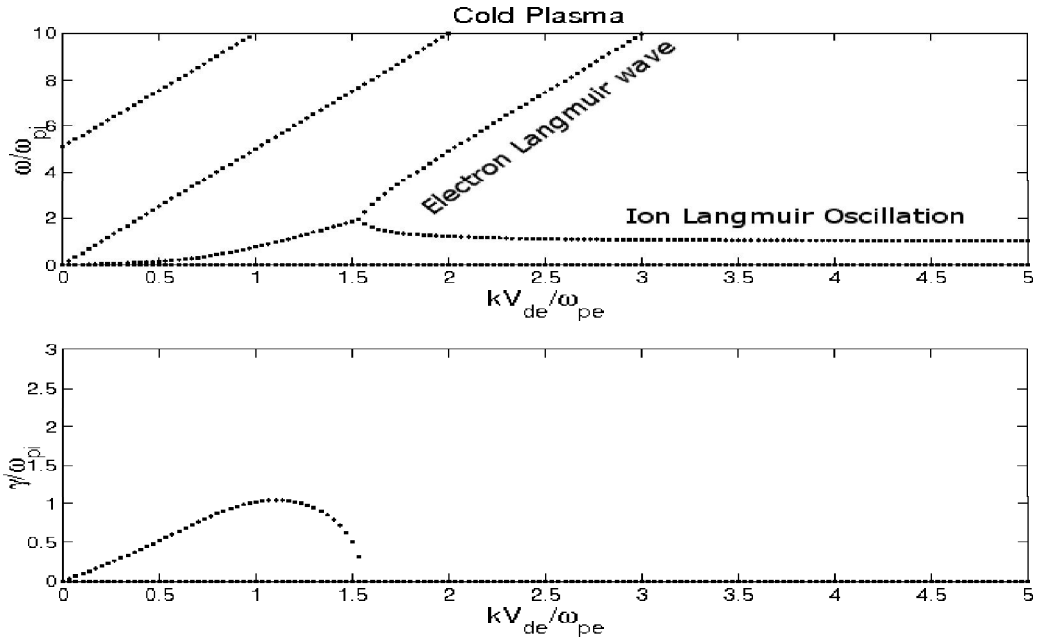

Figure 2.1: The dispersion curves of cold plasma from Eq.(2.35).

plasma frequency and for electrons it is the Doppler-shifted electron Langmuir frequency. We should remember that in Eq. (2.35) the Landau resonance effect is included because we started from kinetic theory and the wave-particle interaction is expressed explicitly in the denominator of Eq. (2.27). At the resonance, the Langmuir-oscillating ions at specific wavelength have the same phase-velocity as the backward Doppler-shifted electron Langmuir wave. As a consequence the negative-energy electron Langmuir wave transfers energy to amplify ion Langmuir oscillations, and this is a collective behavior because whole ions oscillate at the same frequency.

With thermal effects, the electron and ion Langmuir waves start to propagate and their group velocities become electron-acoustic and ion-acoustic velocities. In this consideration the higher terms in Eq.(2.28) should be retained, since these two terms ξ_i and ξ_e are not so small anymore. According to this argument, we preserve three terms in Eq.(2.28), and the two elements ξ_i and ξ_e become

$$1 + \xi_i Z(\xi_i) \approx 1 + (-1 - \frac{1}{2\xi_i^2} - \frac{3}{4\xi_i^4}) = -\frac{1}{2\xi_i^2}(1 + \frac{3}{2\xi_i^2}) \tag{2.36}$$

$$1 + \xi_e Z(\xi_e) \approx 1 + (-1 - \frac{1}{2\xi_e^2} - \frac{3}{4\xi_e^4}) = -\frac{1}{2\xi_e^2}(1 + \frac{3}{2\xi_e^2}) \tag{2.37}$$

because ξ_i and ξ_e are still larger than unity, they can be further approximated to

$$1 + \xi_i Z(\xi_i) \approx -\frac{1}{2\xi_i^2}(1 - \frac{3}{2\xi_i^2})^{-1} = -\frac{k^2 v_{Ti}^2}{2\omega^2}(1 - \frac{k^2 C_{si}^2}{\omega^2})^{-1} \tag{2.38}$$

$$1 + \xi_e Z(\xi_e) \approx -\frac{1}{2\xi_e^2}(1 - \frac{3}{2\xi_e^2})^{-1} = -\frac{k^2 v_{Te}^2}{2\omega^2}\left((1 - \frac{kV_{de}}{\omega})^2 - \frac{k^2 C_{se}^2}{\omega^2}\right)^{-1} \tag{2.39}$$

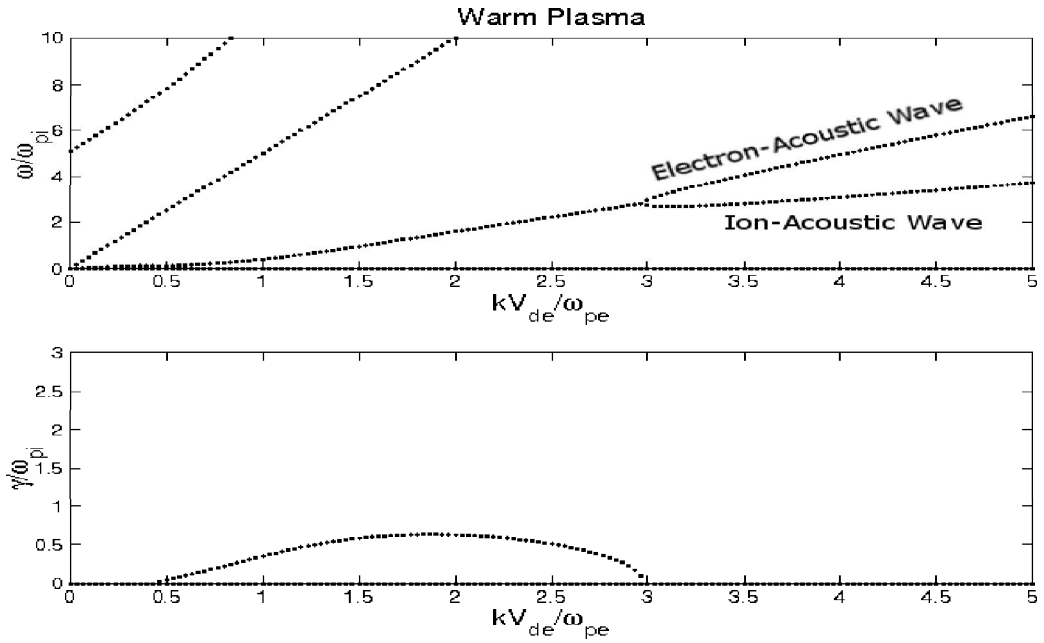

Figure 2.2: The dispersion curves of warm plasma from Eq.(2.40).

Replacing Eq.(2.38) and (2.39) into the dispersion relation Eq.(2.29), the obtained equation is exactly the one derived from warm multifluid equations (Aggarwal 1979), the Buneman mode in warm plasma.

$$D(k, \omega_r + i\gamma) = 1 - \frac{\omega_{pi}^2}{\omega^2 - k^2 C_{si}^2} - \frac{\omega_{pe}^2}{(\omega - kV_{de})^2 - k^2 C_{se}^2} = 0 \tag{2.40}$$

In Fig.(2.2) we can see the original ion Langmuir oscillation starts to propagate because of the thermal effects, and the group velocity $d\omega/dk$ of ion branch is the ion-acoustic velocity.

If the thermal velocity compare to wave phase velocity is not so small, as shown above, more higher order terms should be considered. From this derivation we can see clearly the fluid-like Buneman instability , shown in Eqs.(2.28) and (2.40), is only the approximation of ion-acoustic mode when thermal effects are not so important. Both of these instabilities share the same nature of wave-particle interaction, i.e. the Landau resonance effect, and this is clearly shown because we started from the full kinetic consideration. The denominator in velocity integration depicts the truth that wave-particle resonance takes place when phase velocity is close to particle velocity, either partially in thermal distribution or as-a-whole in cold plasma limit. That is comprehensible that the multifluid dispersion relation fails to describe the indivudual thermal motion of particles, but treats plasma as a collective object. Therefore the Buneman and ion-acoustic modes are the same instability, which share the same Landau resonance effects but demonstrate in different drift velocity limits.

3 Current Driven Low-Frequency Electrostatic Waves in the Solar Corona

3.1 Introduction

The solutions of important solar physical problems like the heating of the corona, reconnection and electron acceleration are thought to be closely related to low-frequency plasma waves (Priest & Forbes 2000). Coronal plasma waves can be driven, e.g., by electron beams in current-carrying system. Indeed, the existence of current concentrations in the solar atmosphere can be inferred from observed properties of the solar magnetic field (Sui & Holman 2003) and from the observed plasma motion in the photosphere (Büchner 2006a). There it was shown that the strongest currents are generated in the direction parallel to the solar magnetic field. They reach their highest concentration at sites of considerable connectivity changes of the magnetic field along the magnetic arcs which are anchored in the moving photospheric plasma. With the ongoing concentration of coronal currents the corresponding current carrier velocity exceeds the threshold of plasma instabilities. The excited waves can cause an effective dissipation of the current energy which leads to a violation of the frozen-in condition of magnetic fields and allows magnetic reconnection in principle (Büchner & Daughton 2007, Leonid & Kulsrud 2006). The problem of reaching a sufficient amplitude of the turbulence to achieve the necessary amount of anomalous resistivity in current sheets was well described in the past (Coroniti 1985, Treumann 2001).

Several candidate mechanisms have been proposed for the microscopic origin of anomalous resistivity. Anomalous transport can be created due to ion-acoustic turbulence (Bychenkov et al. 1988), due to the kinetic Alfven wave instability (Voitenko 1995, Bellan 1999), lower-hybrid drift waves (Davidson & Gladd 1975) and lower-hybrid waves (Ott et al. 1972). Waves in lower hybrid frequency range driven by modified two-stream instability have been studied recently by means of quailinear theory (McMillan & Cairns 2006) and kinetic simulation (McMillan & Cairns 2007). Theoretical approach to study of turbulence evolution and calculation of nonlinear saturation level, as well as derivation of anomalous transport properties is usually proceeded by means of quasi-linear theory (Vedenov 1963).

The results of the quasi-linear approach to the problem of anomalous resistivity was recently summarized by Yoon & Lui (2006) and obtained for two limiting cases of current-driven instabilities, for the Buneman instability of parallel to the magnetic field propa-

gating waves if the electrons stay unmagnetized (Buneman 1959) and for the modified two-stream instability (MTSI) in the case where the electrons are highly magnetized and the waves propagate mainly perpendicular to the magnetic field (Ott et al. 1972)). Currently, however, it was shown that it is important to consider the non-linear evolution of plasma waves since structures may be formed, which enhance the collisionless dissipation (Büchner & Elkina 2006). Some efforts have been done to incorparate anomalous resistivity model into overall dynamics of current sheet. Reconnection model with ion-acoustic turbulent-induced resistivity have been proposed by Coroniti (1985) and Uzdensky (2003).

While modern multi-spacecraft observations could proof the existence of transport due to plasma waves in collisionless current sheets of the Earth's magnetosphere (Panov et al. 2006), it is impossible to directly observe plasma waves and their consequences in the solar corona. Hence theoretical investigations are needed to clarify the excitation conditions, the possible nonlinear evolution of waves in the corona.

Here in this paper we investigate which modes most probably are excited by currents in the solar corona. In order to find the linear dispersion properties of waves driven by parallel currents we developed a solver for the set of multi-fluid equations. We consider an electron-beam plasma model of the solar corona we take into consideration electron inertia and thermal effects. This approach permits us to study phenomena which are relevant down to scales of the order of $\sim c/\omega_{pe}$ and characteristic times up to ω_{pe}^{-1}, where ω_{pe} is the plasma frequency. For the most unstable waves we then estimate the achievable collisionless dissipation rate assuming trapping as the leading saturation mechanism.

First, in Section 3.2, we describe our plasma model for solar coronal current flows and discuss the limits of applicability of a multi-fluid approach. Then we solve the dispersion relation for appropriate solar coronal parameters. Section 3.3 is devoted to a parametric study of the plasma instability of parallel and obliquely propagating unstable waves generated by currents flowing parallel to the solar magnetic field. Finally, in Section 3.4, we present an estimate of the collisionless dissipation rate resulting from the two main modes identified by the linear dispersion analysis and section 3.5 contains our conclusions.

3.2 Multi-Fluid Linear Dispersion Analysis

The multi-fluid equations describing electrons drifting parallel to an external magnetic field against a thermal ion background at rest is given by

$$\frac{\partial N_\alpha}{\partial t} + \nabla \cdot (N_\alpha \vec{V}_\alpha) = 0 \tag{3.1}$$

$$\frac{\partial \vec{V}_\alpha}{\partial t} + \vec{V}_\alpha \cdot \nabla \vec{V}_\alpha + \frac{\nabla P_\alpha}{m_\alpha N_\alpha} = \frac{q_\alpha}{m_\alpha}(\vec{E} + \frac{\vec{V}_\alpha \times \vec{B}}{c})$$

Here we used the following notation V_α for the drift velocity of particle specie, P_α for the pressure, m_α for the mass. $k_{||}$ is the component of the wave vector $\vec{k}$ parallel to a homogeneous and constant external magnetic field B_0, k_B is the Boltzmann constant $\omega_{p\alpha} = \sqrt{(4\pi e^2 n_\alpha / m_\alpha)}$ are plasma frequencies of electrons and ions, respectively, $\lambda_{De} = v_{te}/\omega_{pe}$ is the Debye length. N_α are the plasma species' number densities.

As noted, on the right-hand side of momentum equation the binary-collision viscous term ($\frac{R_{\alpha\beta}}{N_\alpha m_\alpha}$) is neglected since the mean free path of solar coronal plasma is much larger than the sacle length of coronal loop, and interesting phenomena of wave particle resonance such as Landau damping is negligible in the considered wavelength range. In the visous term $R_{\alpha\beta}$ is the momentum transfer rate from species β to α. The gravitational term (g) is also neglected for the simplicity of consideration.

Instabilities as well as the resulting generation of anomalous resistivity are irreversible thermaldynamics processes, which we expect energy could exchange with surroundings, hence the isothermal equation of state is a reasonable assumption. The general isotropic energy equation

$$\frac{dP_\alpha}{dt} = c_{s\alpha}^2 \frac{d}{dt}(m_\alpha N_\alpha) \tag{3.2}$$

where $c_{s\alpha}^2 = T_\alpha / m_\alpha$ is the sound velocity with the isothermal specific heats ratio: $\gamma_\alpha = 1$

The multi-fluid equations 3.1 and 3.2 have to be solved together with the Maxwell equations for the electromagnetic field

$$\begin{aligned} \nabla \times \vec{B} = \frac{4\pi}{c} \sum q_\alpha N_\alpha \vec{V}_\alpha + \frac{1}{c}\frac{\partial \vec{E}}{\partial t} \qquad \nabla \times \vec{E} = -\frac{1}{c}\frac{\partial \vec{B}}{\partial t} \\ \nabla \cdot \vec{E} = 4\pi \sum q_\alpha N_\alpha \qquad \nabla \cdot \vec{B} = 0 \end{aligned} \tag{3.3}$$

In warm plasmas thermal effects contribute to wave dispersion. In order to determine the limits of applicability of the fluid equations 3.1 let us consider the resonance condition for wave-particle interactions that is beyond the scope of a fluid description. In fact, wave-particle interactions become relevant when the argument of the plasma dispersion function, derived for a linearized Vlasov equation, diverges (Gary et al. 1984). At $k \times B_0 = 0$, i.e. for parallel propagating waves with wave frequency ω_s the corresponding resonant factors are given by

$$\xi_\alpha^s = \frac{\omega_s - \vec{k}\vec{V}}{\sqrt{2}|k_x| v_{t\alpha}} \tag{3.4}$$

Resonant particles can gain energy by Landau-damping of the plasma waves. Particles can be considered non-resonant (Gary et al. 1984) as long as $|\xi_\alpha^s| \gg 1$, practically, as long as the wave's phase velocity differs by more than a thermal speed from the center of the distribution function. We will take this into account to estimate the limits of applicability of our solutions of the "warm" plasma set of multi-fluid and Maxwell equations (3.1 and 3.3).

At the linear stage each physical quantity can be expressed as a sum of an average and a small perturbation term. Let us look for solutions in form of a planar wave ($A = A_0 + A_1 \exp \imath(\vec{k} \cdot \vec{X} - \omega t)$). Then the linearized plasma equations become

$$n_\alpha = N_\alpha \frac{\vec{k}\cdot\vec{u}_\alpha}{\omega_{*\alpha}} \tag{3.5}$$

$$\omega_{*\alpha}^2\vec{u}_\alpha - c_{s\alpha}^2\vec{k}(\vec{k}\cdot\vec{u}_\alpha) - i\omega_{*\alpha}\frac{q_\alpha}{m_\alpha}\left(\delta\vec{E} + \frac{\vec{U}_\alpha\times\vec{b}}{c}\right) - i\omega_{*\alpha}\vec{u}_\alpha\times\vec{\Omega}_\alpha = 0 \tag{3.6}$$

and the Maxwell equations become

$$\frac{q_\alpha}{m_\alpha}\delta\vec{E} = \frac{ic^2{\omega_{p\alpha}}^2}{\alpha\omega\sigma_\alpha}\left(\vec{k}\vec{k}\cdot - \frac{\omega^2}{c^2}\right)\vec{j} \quad and \quad \frac{q_\alpha}{m_\alpha}\vec{b} = -\frac{ic{\omega_{p\alpha}}^2}{\alpha\sigma_\alpha}(\vec{k}\times\vec{j}) \tag{3.7}$$

where

$$\vec{j} = \sum_\alpha \sigma_\alpha\left(\vec{u}_\alpha + \vec{U}_\alpha\frac{\vec{k}\cdot\vec{u}_\alpha}{\omega_{*\alpha}}\right) \tag{3.8}$$

Here $\omega_{*\alpha} = \omega - \vec{k}\cdot\vec{U}_\alpha$ is the wave frequency Doppler shifted as in a moving with the drift velocity frame and $\alpha = \omega^2 - c^2k^2$. Notations Ω_α and σ_α are cyclotron frequency and charge density, which are defined as $(q_\alpha\vec{B}/cm_\alpha)$ and $N_\alpha q_\alpha$. Since here we focus on low-frequency electrostatic waves Faraday's law implies that the wave vector is parallel to the perturbed electric field ($\vec{k} \parallel \delta\vec{E}$), hence $\vec{b} = (c/\omega)\vec{k}\times\delta\vec{E}$=0. The resulting linear dispersion relation of electrostatic waves is (see, e.g., Aggarwal (1979)):

$$F(\omega,\vec{k}) = \sum_\alpha \frac{\omega_{p\alpha}^2(\Omega^2\cos^2\theta - \omega_{*\alpha}^2)}{\omega_{*\alpha}^2(\Omega_\alpha^2 - \omega_{*\alpha}^2) - c_{s\alpha}^2(k\cdot\Omega_\alpha^2\cos^2\theta - k^2\cdot\omega_{*\alpha}^2)} = 1 \tag{3.9}$$

In a cold unmagnetized plasma with $c_{s\alpha} = 0$ the Buneman instability dominates, the long wavelength limit of the general ion acoustic instability in case of finite plasma temperatures. For the parallel propagation direction with the electron drift velocity V_{de}, one obtains the dispersion analyzed by Buneman (Buneman 1958):

$$\frac{\omega_{pi}^2}{\omega^2} + \frac{\omega_{pe}^2}{(\omega - \vec{k}\cdot\vec{V}_{de})^2} = 1 \tag{3.10}$$

Assuming a small growth rate $\gamma \ll \omega$ equation (3.10) yields for the fastest growing wave mode $\omega = \omega_m + i\gamma_m$

$$\omega_m = \frac{1}{2}\left[1 + \frac{1}{2}\left(\frac{m_e}{2m_i}\right)^{1/3}\right] \tag{3.11}$$

$$\gamma_m = -\frac{1}{2}\sqrt{3}\left[\left(1 - \frac{1}{2}\left(\frac{m_e}{2m_i}\right)^{1/3}\right)\right] \tag{3.12}$$

In the cause of a Buneman instability the energy is exchanged by a resonance with Langmuir oscillations in the electron reference frame. Hence the Doppler-shifted Langmuir oscillations ($\omega \simeq (kV_{de}\cos\theta - \omega_{pe})$) of the negative energy branch exchange wave energy with an ion plasma oscillations at the characteristic frequency ($\omega = \omega_{pi}$).

The instability against waves, propagating almost perpendicular to the magnetic field, is usually called "Modified Two-Stream Instability (MTSI) (Buneman 1963, Ott et al. 1972). Assuming magnetized electrons and unmagnetized ions the dispersion relation (3.9) reduces for propagation angles $\theta \simeq 90^o$ to

$$\frac{\omega_{LH}^2}{\omega^2} + \frac{m_i}{m_e}\frac{\omega_{LH}^2\cos^2\theta}{(\omega - k_\parallel V_{de})^2} = 1 \tag{3.13}$$

Solving (3.13) one finds that the fastest growing mode occurs at

$$\omega \simeq \omega_{LH} \qquad \gamma \simeq \frac{\omega_{LH}}{2} \tag{3.14}$$

Here ω_{LH} is the lower-hybrid frequency given by

$$\omega_{LH} = \omega_{pi}\left(1 + \frac{\omega_{pe}^2}{\Omega_e^2}\right)^{-1/2} \tag{3.15}$$

In case of $\omega_{pe}^2 \gg \Omega_e^2$, i.e. in weakly magnetized plasmas, the lower-hybrid frequency reduces to $\omega_{LH} \simeq \sqrt{\Omega_e\Omega_i}$. However, in the general case of an arbitrary propagation the dispersion relation (3.9) can be solved only numerically.

3.3 Parametric Investigation for Solar Coronal Conditions

At the present time the plasma parameters of the solar corona and the coronal magnetic field strength are not very well known, yet. On the other hand, as shown in section 3.2 the magnetization, expressed in terms of the ratio of the characteristic frequencies Ω_e^2 and ω_{pe}^2, plays a crucial role in determining the stability properties of a current driven plasma. Let us consider a range, e.g. for the plasma beta, the ratio of plasma over magnetic pressure, from $\beta = 16\pi nkT/B^2 \cong 14$ to $\beta \ll 1$ (Gary & Alexander 1999). Numerical simulations have shown that critical current concentrations can be found in the lower corona (Büchner 2006a). The coronal plasma is fully ionized with a typical average electron and ion temperatures of the order of $T_e \cong 10^6 K$, so we will consider isothermal plasma conditions $T_e = T_i$. At a height of, say, 5 $Mm = 5 \times 10^6 m$ above the photosphere the number density of the quasi-neutral plasma has dropped down to about $n_{e,i} = 1 \times 10^9 cm^{-3}$ while the magnetic field strength can change in a wide range, say, from 100 to 2500 G. The corresponding plasma beta is $\beta = 3\times10^{-4} - 3\times10^{-2}$ and the characteristic frequency ratio Ω_e/ω_{pe} is in the range 0.15 – 1.5. From simulations one can estimate a current carrier velocity and relate it to an electron bulk velocity V_{de}, which has to exceed the electron thermal velocity in order to trigger an ion-acoustic type instability in the solar corona

Table 1

Parameters	Corona(Active Region)	Flare
$n_e(cm^{-3})$	1×10^9	1×10^{10}
$T_e(K)$	1×10^6	3×10^7
$T_i(K)$	1×10^6	3×10^6
$B(G)$	$100 \div 2500$	100
$\beta = P_{thermal}/P_{magnetic}$	$0.0003 \div 0.03$	0.1
Ω_e/ω_{pe}	$1.5 \div 0.15$	0.32

(Büchner 2006b). Within these parameter ranges (Table 1) we investigate the properties of current-driven instabilities numerically by solving equation (3.9).

First, let us consider the dependence on the actual magnetic field strength. Fig. 3.1 depicts the solution of the multi-fluid dispersion relation (3.9) for a fixed electron bulk velocity $V_{de} = 1.5v_{te}$ and for waves propagating at an angle $\theta = 20^o$ with respect to the magnetic field. Shown are the solutions for three different degrees of magnetization ($\Omega_e/\omega_{pe} = 0.5,\ 1.0,\ 1.5$). The figure also demonstrates the relation of the dispersion branches $\omega(k)$ to the eigenmodes of the plasma, the Doppler shifted Langmuir (LW) and electron-cyclotron (EC) wave with positive wave energy and the Doppler shifted Langmuir (LW^*) and electron-cyclotron (EC^*) wave with negative wave energy. The growth rate γ is depicted by a dashed line and the corresponding real frequency by a dotted line. Fig. 3.1 shows that the coupling with the Doppler shifted Langmuir waves (LW^*) occurs in the range $k_{\|} = 0.8 - 1.25$. The strength of the coupling with the Doppler shifted electron cyclotron wave depends strongly on Ω_e/ω_{pe}. The different branches of instability can be identified by considering the excitation mechanisms. In fact, the instability will be excited by a coupling between negative (Doppler-shifted Langmuir and electron cyclotron) energy waves and positive energy ion plasma waves. Doppler-shifted electron cyclotron wave exists in a magnetized plasma due to an anomalous Doppler effect (Nezlin 1976). These two negative energy wave modes interact with the ion wave. Hence two branches of instability have to be expected. Originally, the instabilities and waves were named for specific conditions. The Buneman mode is identified for a parallel propagating wave. Upper-hybrid (UH) wave modes (characteristic frequency: $\omega_{UH} = (\omega_{pe}^2 + \Omega_e^2)^{1/2}$) and lower-hybrid waves ω_{LH} (see equation 3.15) are defined as waves propagating in the direction perpendicular to the magnetic field. Generalizing these two instability modes, derived for one-dimensional wave propagation directions, to the general case of arbitrary propagation angles, we unify the confusing terminology which is used in the literatures. In fact, for perpendicular propagation directions $\Omega_e \geq \omega_{pe}$ and $\theta = \pm\pi/2$ Langmuir waves become UH waves while electron cyclotron waves become LH waves. In the case $\Omega_e \leq \omega_{pe}$ and $\theta = \pm\pi/2$ Langmuir waves approach LH waves and electron cyclotron waves approach the UH wave branch.

In this range the two primary unstable modes, the MTSI mode and Buneman mode, are well pronounced, although their names are obtained in the cold plasma limit (see Section 3.2). The MTSI mode is due to a lower-hybrid frequency resonance in the perpendicular direction while the Buneman instability corresponds to oscillations near the ion plasma frequency for all propagation directions. As one can see from the left panel in Fig. 3.1, in the case of weaker magnetic fields $\Omega_e/\omega_{pe} = 0.5$ the Buneman instability occurs at shorter wavelength rather than the MTSI. With increasing magnetization, how-

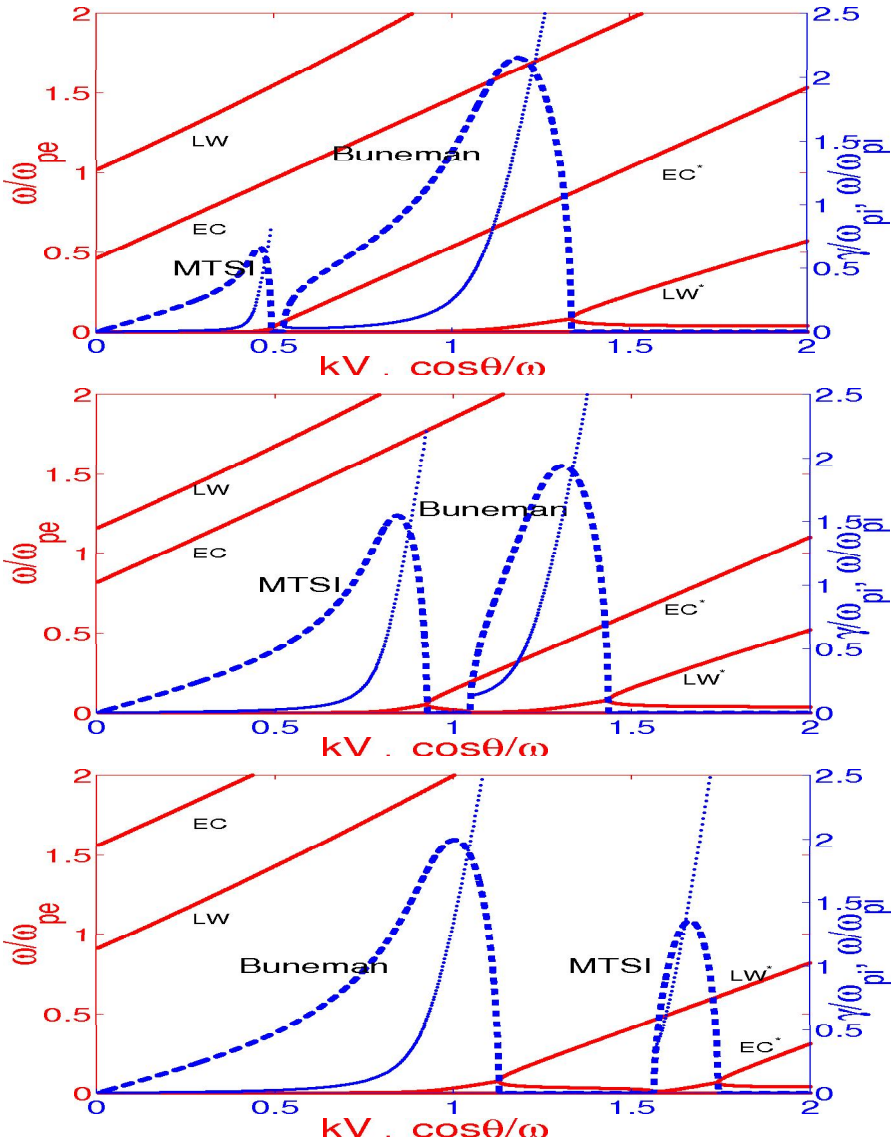

Figure 3.1: (Color online) Wave dispersion for different magnetic field strengths $\Omega_e/\omega_{pe} = 0.5,\ 1.0,\ 1.5$, for a propagation angle $\theta = 20^o$ with respect to the magnetic field. The electron bulk velocity is $V_{de} = 1.5 \cdot v_{te}$. Solid lines depict the branches $\omega(k)$, related to the Doppler shifted Langmuir and electron-cyclotron waves of positive wave energy branch (LWandEC), and of negative wave energy branch (LW^*andEC^*). The dashed line depicts the corresponding growth rate γ, the real frequency is depicted by a dotted line. is shown by dotted line.

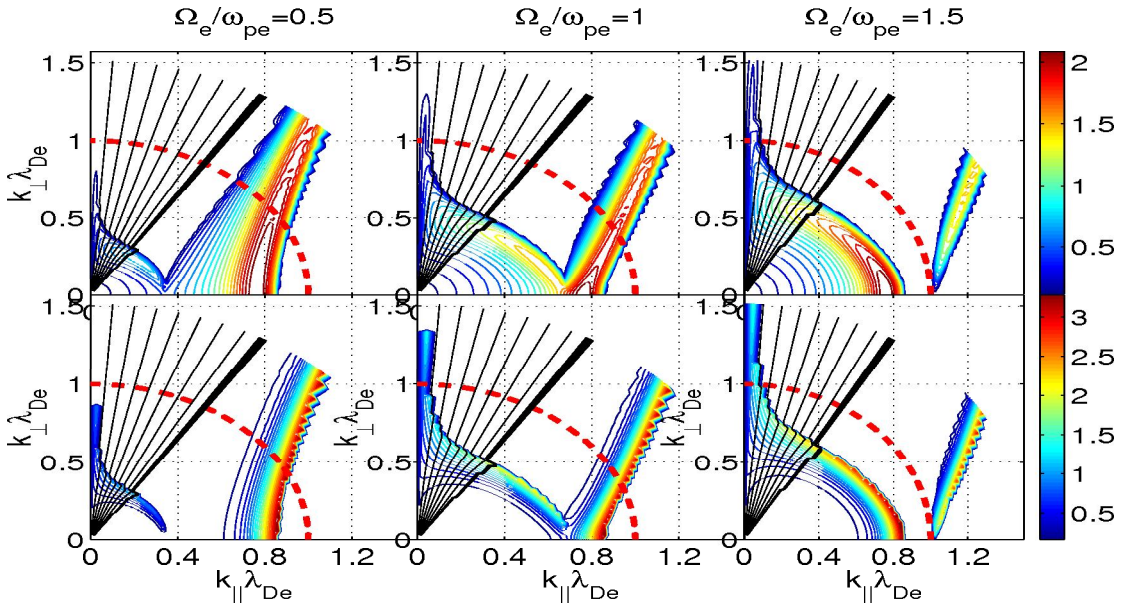

Figure 3.2: (Color online) Directional dependence ($k_{\|}\lambda_{De}$ vs. $k_{\perp}\lambda_{De}$) of the normalized growth rate γ/ω_{pi} (upper panel) and of the real frequency ω/ω_{pi} of low-frequency electrostatic waves propagating at arbitrary angles with respect to the magnetic field in the solar corona. As in Fig. 3.1, the results are shown for three different magnetization levels $\Omega_e/\omega_{pe} = 0.5,\ 1,\ 1.5$, an electron drift velocity $V_{de} = 1.5v_{te}$ and temperatures $T_e = T_i$. The solid contours indicate the resonance regions $\xi_e \simeq 1$, where strong resonant wave-particle interactions will take place and the multi-fluid approach breaks down. The red dashed line depicts the short wavelength limit (large $k_{\|}\lambda_{De}$), where kinetic plasma effects, e.g., collisions, must be taken into account.

ever, the spatial spectrum of the MTSI driven waves shifts toward the shorter wavelengths range, while the wave spectrum due to the Buneman instability in parallel direction practically does not shift in the wave number space at all.

Fig. 3.2 depicts the directional dependence, i.e. the dependence on $k_{\|}\lambda_{De}$ and $k_{\perp}\lambda_{De}$, of the growth rate γ/ω_{pi} (upper panel) and the real frequency ω/ω_{pe} for low-frequency electrostatic waves propagating at arbitrary angles with respect to the magnetic field in the solar corona. As in Fig. 3.1 the results shown for three different magnetization levels $\Omega_e/\omega_{pe} = 0.5,\ 1,\ 1.5$ were obtained assuming an electron drift velocity $V_{de} = 1.5 \cdot v_{te}$ and temperatures $T_e = T_i$. The solid contours indicate the resonance regions $\xi_e \simeq 1$, where strong resonant wave-particle interactions will take place and the multi-fluid approach breaks down. The red dashed line depicts the short wavelength limit (large $k_{\|}$), from where on kinetic plasma effects, e.g., collisions, must be taken into account. This two-dimensional spatial spectrum reveals that the fastest growing instability is due to a coupling with the Doppler shifted Langmuir waves, which propagate in the parallel direction (the Buneman mode in one dimensional propagation).

For the typical parameter range of the lower corona the oblique mode, the inner branch of the spectrum that couples to LH waves in the perpendicular propagation direction, exhibits the highest growth rate. Fig. 3.3 depicts the dependence of the growth rate of these fastest growing waves (inner branch) on electron drift velocity and plasma beta. Our

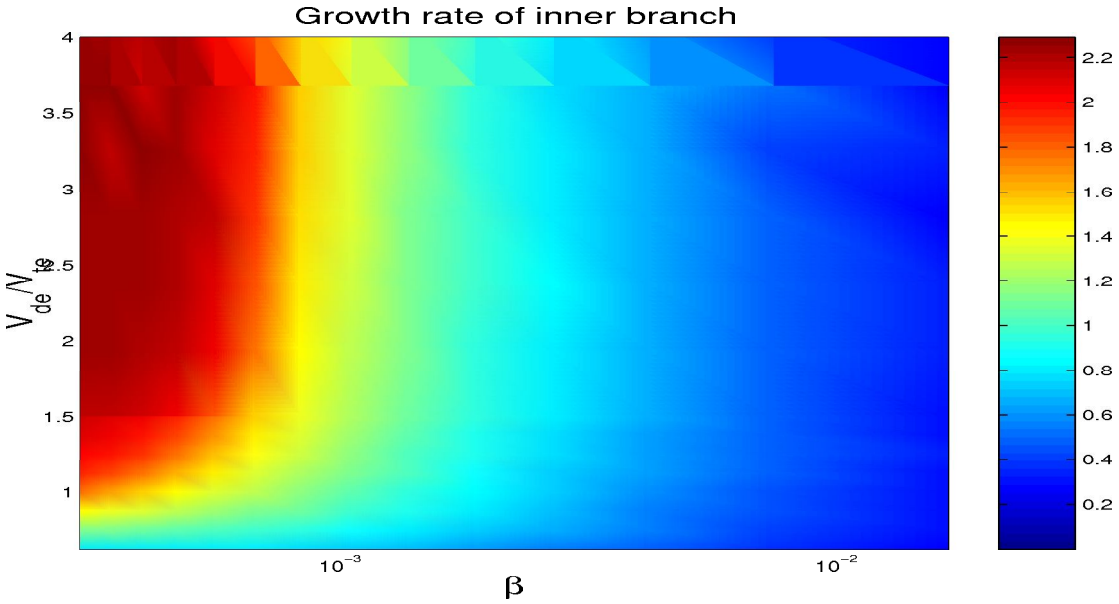

Figure 3.3: Normalized growth rate (γ/ω_{pi}) of the inner branch on dependence of the electron drift velocity, which is normalized to the electron thermal speed, and the plasma beta. The color coding depicts the normalized to the ion plasma frequency growth rate. The plasma parameters, except the electron drift velocity as a variable, are the same as those used in the other Figures.

multi-fluid analysis is valid only for sufficiently large electron bulk velocities, for which the wavelength of Buneman-unstable modes exceeds the Debye length so that kinetic effects can be neglected. Hence we show only results obtained for sufficiently large electron drift velocities exceeding the electron thermal speed. As it can be seen in Fig. 3.3 the wave growth is faster in low beta conditions in the lower corona, where the magnetic fields are strongest, and for larger electron bulk velocities. Fastest growing are parallel propagating waves (see the right panel in Fig. 3.2 that corresponds to $\Omega_e/\omega_{pe} = 1.5$) that correspond to the Buneman mode. On the other hand in weaker magnetic field regions with higher plasma beta and for slower electron bulk velocities the highest fastest growing waves of the inner branch are obliquely propagating (see the left panel in Fig. 3.2 that corresponds to $\Omega_e/\omega_{pe} = 0.5$).

Our linear instability analysis has revealed, therefore that the most unstable low-frequency electrostatic wave instabilities occur in the parallel propagation direction. These waves couple to Doppler shifted Langmuir oscillations although they belong to different branches for different magnetic field strength. For small plasma beta (strong magnetic fields) and strong drifts the MTSI mode growth becomes comparable to that of the Buneman mode. Since the MTSI mode propagates at oblique angles this information is lost in the usually used one-dimensional instability analyzes.

3.4 Nonlinear Saturation

The dc coronal heating, magnetic reconnection and particle acceleration require a sufficiently large amount of dissipation, e.g. resistivity, which would dissipate the coronal currents. Since binary collisions are inefficient in the collisionless corona, anomalous dissipation due to irreversible wave-particle interactions is needed (Büchner 2006b). Unfortunately, a self-consistent treatment of the saturation of the wave growth and the corresponding nonlinear evolution requires messy numerical kinetic simulations (Büchner & Elkina 2005).

Before such simulations are performed, let us first estimate the saturated wave power and the corresponding anomalous transport properties. Such estimate can be carried out by considering the momentum transfer between the current-driven plasma waves driven by non-resonant fluid instabilities, as described above, and the plasma (Davidson & Gladd 1975). This approach uses the fact that the saturation of non-resonant instabilities is not sensitive to the details of distribution functions. Instead, it depends mainly on macroscopic quantities, on the number density and the electron bulk drift momentum. The momentum conservation law of electrons can be written in the form of generalized Ohm's law for the electrostatic fluctuations, as one can find in the equation (19) of the reference by Yoon & Lui (2006).

$$\vec{E} + \frac{\vec{v} \times \vec{B}}{c} = -{n_o}^{-1} \int d\vec{k} \int d\omega \left\langle \delta n^e_{\vec{k},\omega} \delta \vec{E}_{\vec{k},\omega} \right\rangle = -{n_o}^{-1} \int d\vec{k} \left\langle \delta n^e_{\vec{k}} \delta \vec{E}_{\vec{k}} \right\rangle = \eta \vec{J} \tag{3.16}$$

where η denotes the anomalous resistivity and $\vec{J} = en_o\vec{V}_{de}$ is the current density of the drifting electrons. In order to estimate $< \delta n^e_{\vec{k}} \delta \vec{E}_{\vec{k}} >$, we carry out a Fourier transformation on $\delta n^e_{\vec{k}}$ and $\delta \vec{E}_{\vec{k}}$ with the use of linearized Poisson equation $q_\alpha \delta n_\alpha = -\chi_\alpha i k_x \delta E_x$, where χ_α is the electric susceptibility of species α.

One obtains the estimated anomalous resistivity during saturation

$$\eta = \frac{2}{m_e n V_{de}} \int dk Im(k_x \chi_e) W_k, \tag{3.17}$$

This equation is first derived in eq.(23) of the reference by Davidson & Gladd (1975). In the above expression $W_k = (1/2)\delta E^2_{0k} \exp(2\gamma_k t)$ is the spectral wave energy density of the electric field fluctuations. Let us estimate the maximum contributions to the integral in (3.17) for the Bunemann and the lower hybrid modes separately with η_B and η_{LH} as the contributions of the Bunemann and the lower hybrid waves. Using the analytical solution of the dispersion relation for the Buneman (3.10) and the modified two stream instabilities (3.13), we can estimate the anomalous resistivity resulting from the interaction of the two unstable wave modes with the electrons as follows

$$\eta_B = \frac{2}{n m_i V^2_{de}} \cdot \left(\frac{m_i}{m_e}\right)^{1/2} \cdot \frac{W^B_{sat}}{\omega_{pi}} \qquad \text{and} \qquad \eta_{LH} = \frac{2}{n m_i V^2_{de}} \cdot \frac{W^{LH}_{sat}}{\omega_{LH}} \tag{3.18}$$

Note that the wave growth saturates after an equilibrium is established between the electron friction force and the accelerating electric field. The corresponding momentum balance can be as Hirose (1978), Ishihara et al. (1981)

$$n_e m \frac{dV_e}{dt} = -\frac{n_e e^2}{m_e} \sum_k \frac{W_k \gamma_k k \omega_{*ke}}{[(\omega_{*ke} + \Omega_e)^2 + \gamma_k^2]^2} \tag{3.19}$$

Equation 3.19 allows one to estimate the change of the electron drift velocity ΔV_{de} as

$$\Delta V = \frac{e^2}{m^2} \frac{W_{sat} k_m \omega_{*k\alpha}}{[(\omega_{*k\alpha})^2 + \gamma_m^2]^2} \tag{3.20}$$

The saturation of narrow-spectra waves moves the system to a marginally stable state (Sizonenko & Stepanov 1971). Let us estimate the saturation level of the waves due to particle trapping in the potential wells of the fastest growing waves. The fastest growing mode saturates if $k_m|\Delta V| = \omega_m$, where ω_m is the maximum real frequency obtained from the dispersion relation. The electric wave power at saturation can, therefore, be estimated as

$$W_{sat} \simeq \frac{m^2 \omega_m \omega_{res}^3}{e^2 k_m^2} \tag{3.21}$$

where $\omega_{res} = -\omega_{pe} + \vec{k}_m \cdot \vec{V}_{de}$, For comparison, in cold plasmas the electrostatic saturation amplitude of purely parallel propagating waves is approximately as $W_{sat} \simeq 0.25 \cdot (m_e/m_i)^{1/3} n_e m_e V_{de}^2$ (Hirose 1978).

For the analytical solutions of the Buneman- and the modified two-stream instabilities (see Section 3.2) one can now obtain the saturation levels for the arising two unstable modes and compare them by calculating their ratio

$$\frac{W_{sat}^B}{W_{sat}^{LH}} = \frac{k_{m,LH}^2}{k_{m,B}^2} \sim 0.3 \Rightarrow \frac{\eta_B}{\eta_{LH}} = \left(\frac{m_i}{m_e}\right)^{1/2} \frac{\omega_{LH}}{\omega_{pi}} \frac{W_{sat}^B}{W_{sat}^{LH}} \simeq 8 \quad if \quad \Omega_e \simeq \omega_{pe} \tag{3.22}$$

Equation (3.22) indicates that for the moderate plasma magnetization condition $\Omega_e/\omega_{pe} \simeq 1$, typically for the lower solar corona, the contributions of anomalous transport from MTSI instability is of the same order of magnitude as the Buneman mode.

3.5 Conclusion

We investigated the dispersion properties of current-driven solar coronal plasma instabilities by solving the linearized multi-fluid plasma and the field equations. In particular we looked for low-frequency waves, which supposedly will carry most of the energy, released by the currents, and electrostatic waves, which interact most efficiently with the plasma particles. We did not restrict our analysis to either the perpendicular or the parallel wave propagation directions with regard to the external magnetic field.

We have performed a parametric study on the dependence of unstable waves linearly within the most probable parameter ranges of the solar coronal plasma. We have found that two basic low-frequency instabilities are excited and all transitions between them. In

order to identify the physical mechanisms of the instabilities we analyzed the dispersion properties of the system. It appeared that two negative-energy Doppler-shifted Langmuir and electron-cyclotron modes are excited that can couple to the positive energy plasma eigenmodes. This way a Buneman instability can be excited due to the coupling of ion-plasma oscillations with a Doppler-shifted Langmuir wave. Lower hybrid modes, on the other hand, result from a coupling of Doppler-shifted electron-cyclotron waves with the ion-plasma oscillations.

We further looked for the propagation direction dependence of the wave growth. We found that the Buneman- instability reaches the highest growth rates for a mode propagating parallel to magnetic field. Oblique modes form the longer wavelength part of the spectrum if $\Omega_e < \omega_{pe}$. They become comparable to the parallel modes for medium magnetic field strengths $\Omega_e \sim \omega_{pe}$.

Since the magnetic field strength of the corona varies over a wide range, we have especially addressed the influence of the actual plasma beta on the wave growth. Another important dependence, we have studied, is that of the electron bulk drift velocity, which can only indirectly, via numerical simulations, be inferred from solar observations.

According to our studies the modified two-stream instability (MTSI), which is negligible in weak magnetic fields, becomes significant in stronger magnetic fields. The resulting obliquely propagating waves can, therefore, be regarded as the most relevant mode in the corona above active regions.

In order to estimate the relevance of low-frequency electrostatic waves for the macroscopic dynamics of the solar corona we considered the possible saturation level of the growing waves. We found that for typical solar coronal parameters both, the fastest growing Buneman and the MTSI instabilities, reach about the same order of magnitude saturation level, i.e. although MTSI anomalous resistivity is smaller than Buneman resistivity, it still contributes considerable amount to the anomalous current dissipation. The absolute value can be judged upon by the corresponding "effective collision rate" which reaches up to $\nu \simeq 2(m_e/m_i)^{2/3}\omega_{pe} = 0.6\omega_{pi}$ (Hirose 1978) for the Buneman instability and a few fractions of this value for the MTSI. Since the saturation amplitude further depends on the electron bulk velocity it will vary within a range of $\nu_{eff} \subset 0.2\omega_{pi} - 1\omega_{pi}$. This is close to what is obtained earlier by one-dimensional Vlasov-code simulations of the Bunemann instability in strong magnetic fields and for a electron bulk drift velocity $V_{de} = 2.4v_{te}$. There an effective collision frequency $\nu_{eff} \simeq 0.5\omega_{pi}$ is obtained (Büchner & Elkina 2006).

Note that for the non-linear interaction of the current carriers with the fully developed two-dimensional spectrum of electrostatic coronal plasma waves one can expect a stronger anomalous resistivity and higher "effective collision rates" than those, estimated here and obtained by one-dimensional self-consistent turbulence simulations.

4 Looptop Fast Shock: The Secondary Acceleration

4.1 Introduction

Magnetic reconnection in solar corona is generally considered as the trigger mechanism and the primary energy source of solar flares, which is a catastrophic phenomena that releases the largest amount of photonic energy in our solar system. Observational evidence of coronal magnetic reconnection has been obtained considerably from the *Yohkoh* project in the last decade. Many reconnection models that based on the reconstructed magnetic topology, as well as the large scale MHD simulations of coronal loops (Shimizu et al. 2005, Yokoyama & Shibata 1997), are also proposed to explain the plasma dynamics during solar flares. The hard X-ray (HXR) observations of the coronal looptop and footpoints show that the charged particles, both electrons and ions, can reach hundreds keV or even up to MeV level during the impulsive stage of solar flare, and this corresponds to a very high particle velocity $v \geq 0.5c$ for electrons. However, the direct reconnection outflows are not readily observable. The first evidence of high-speed downflows above flare loops is observed by *Yohkoh*/ SXT during the 1999-Jan-20 flare, showing dark voids flowing downward from the loop cusp regions, with speeds of $v \approx 100 - 200 km \cdot s^{-1}$. In all probability, with the observational deduced plasma parameters above the loop cusp region, the Alfv́en velocity is only in the range of $v \approx 1000 - 3000 km \cdot s^{-1}$, which is still much less than the particle velocity observed from HXR emission.

To bridge the energy discrepancy between the theoretical (and also the observational case mentioned above) plasma outflow velocity and the plasma velocity observed from HXR spectrum, numerous secondary acceleration models have been proposed for the appearance of high energy particles in the context of solar flares. In principle, the secondary plasma acceleration mechanisms of the reconnection outflow can be categorized into three kinds: (1) DC electric field acceleration, (2) stochastic acceleration and (3) shock acceleration.

The DC electric field acceleration, which is further sub-classified as the super-Dreicer (Holman 1985, Tsuneta & Naito 1998) and the sub-Dreicer (Litvinenko & Somov 1995, Litvinenko 1996) accelerations, is mainly a particle acceleration by an assumed electrical potential jump between the reconnetion outflow and HXR emission sites. The primary difficulty of this mechanism is the existence of such a potential jump. Beside, any model with static or steady electric DC fields faces the problem that the electron beam current requires the counterstreaming return current, which severely limits the acceleration efficiency. Contrast to the DC field acceleration, stochastic acceleration is a mechanism that

plasma is accelerated by AC electromagnetic waves.

Since a broadband of wave spectrum is expected in the reconnection outflow, some waves can have constructive interference and others destructive interference with the particle gyromotion, via whistler waves (Steinacker 1992, Hamilton 1992) and lower hybrid waves (Benz 1987, McClements et al. 1990). The energy transfer between waves and particles is therefore a stochastic process. Basically, the concept of stochastic acceleration accomplishes some advantages over the concept of (large-scale) DC electric field acceleration, i.e. the accelerating fields occur on a microscopic scale and completely average out over a macroscopic volume, so that no return current problems occur, which require a strong filamentation of the acceleration region in DC electric field models. Nevertheless, the major quarrels of stochastic acceleration are on the exsitence of sufficiently strong wave turbulence in the outflow, which cannot be measured easily, and the inconsistency of this model to the HXR time-of-flight delay measurement.

The concept of shock acceleration in the solar flares context is mainly developed for type II radio bursts, for which the shock speed that propagates outward to interplanetary space can be estimated from the soft X-ray images and the inferred plasma frequency. In the realm of astrophysics, fast shock in the supernova remnants has been proposed as the particle accelerator for high energy protons and Galatic cosmic rays. Particle-in-cell (Lee et al. 2004) and hybrid simulations (Winske 1985, Burgess 2006) are performed the precise scenarios of shock accelerations for Earth's bow shock condition. The new aspect of shock acceleration of coronal plasma is from some observational and theoretical speculations, which indicate that a pair of slow shocks with a sandwiched fast shock can create a viable environment for the plasma acceleration in the reconnection outflow, and the accelerated plasma is further injected along magnetized coronal loop downward to create the chromospheric footpoints HXR emissions. The first observational evidence of the looptop fast shock is presented in the famous work by Masuda et al. (1994), in which the flare is observed by *Yohkoh* HXT and SXT and a clear looptop HXR source is identified. This HXR source located distinctively above the beneath SXR loop, which has a higher density and stronger magnetic field strength. The high plasma temperature $T \approx 2 \times 10^8 K$ of the looptop HXR source is speculated as a consequence of the fast shock heating, for which the waves are generated and reflected back from the obstacle-like SXR loop. A standing fast shock is formed between the reconnection site and the SXR loop by the wave steepening mechanism and its particular magnetic field geometry.

The existence of a looptop fast shock has also been confirmed in a large-scale two dimensional MHD simulation of coronal reconnection (Shimizu et al. 2005, Yokoyama & Shibata 1997). The plasma was heated at the downstream side of fast shock, revealed as a high temperature maxwellian distribution according to the MHD regime. However, from the flare HXR observations the spectrum of plasma distribution usually contains a supra-thermal tail which makes the distribution divert from Maxwellian. In general the plasma energy of the supra-thermal is much higher and the origin this supra-thermal particles is still one of the major issues in solar physics. To understand the acceleration mechanism, in addition to the MHD plasma heating mechanism caused by the conservation of magnetic moment from upstream to downstream of shock, we are interested in the fine structure of shock which is the main location that generates the supra-thermal tail of plasma distribution. In this transition region several drift microinstabilities are possible to exist according to the relative motion of the injected and the reflected plasma flows. With

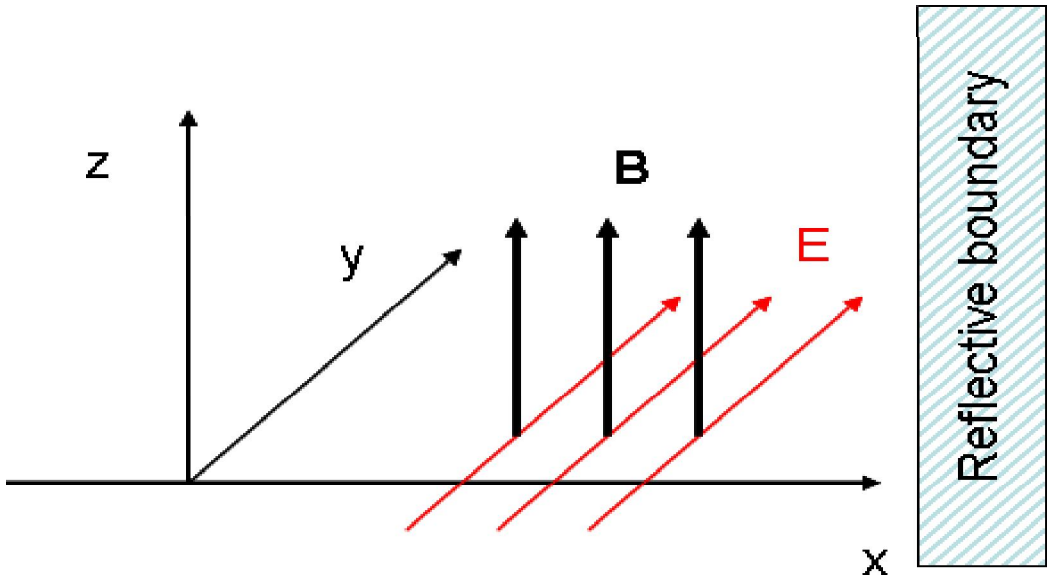

Figure 4.1: The 1D EM PIC simulation setup for fast shock study. A reflective boundary is set to exhibit the reflective characteristic of SXR loop, which has high density and strong magnetic field. Plasmas are pushed back at this boundary because of the small cycltron radii.

a high Mach number inflow, the reflected plasma streams backward against the injected plasma and eventually forms a sufficient condition for Buneman instability, which leads to a resulting fast heating. On the other hand, if we consider a preheated inflow electrons, an ion-acoustic instability can take over the plasma heating and acceleration. Likewise, a complete process, starting from Buneman instability and the accompanying electron heating to the following ion-acoustic instability, is also considered by Papadopoulos (1988). Since both of Buneman and ion-acoustic modes are mainly electrostatic in nature, the strong bipolar DC electric field of these modes are good sources of anomalous resistivity that can cause the plasma heating, and the steepened phase space structure at shock front becomes a perfect accelerator for the supra-thermal tail distribution. Levinson (1992) also discussed the self-generated whistler waves, and in later stage the lower hybrid instability, can accelerated plasma at a perfect parallel shock.

In this work, we perform a one dimensional electromagnetic particle-in-cell simulation (1D EM PIC) to study the plasma acceleration in a fast shock transition region and the plasma heating in the shock downstream side. In Sec. 4.2 we discuss the feasible plasma parameters that can represent the reconnection outflow condition in the cusp region of solar flare loops. In Sec. 4.3 the results of 1D EM PIC simulation are discussed. The plasma kinetic energy level after shock acceleration is also compared with the observed solar flare HXR spectrum. A brief summary is given in the conclusion.

4.2 The Investigation of Solar Flare Reconnection Outflow Parameters

Because of the plasma in the coronal reconnection outflow is of low density and temperature, it is difficult to retrieve the physical characteristics from the thermal or bremsstrahlung radiations. Therefore the plasma parameters of the reconnection outflow can only be assumed based upon the reconnection models, accompanying with the observation from the measurable sources in the flare surroundings.

In general, the plasma density at the base of corona ($H \approx 2500km$ above the photosphere) is higher (Aschwanden 2006), for coronal holes $n \approx (0.5 - 1.0) \times 10^8 cm^{-3}$, for quiet sun $n \approx (1.0-2.0)\times 10^8 cm^{-3}$ and for active regions $n \approx (0.2-2.0)\times 10^9 cm^{-3}$. However in the upper corona, which corresponds to the possible magnetic reconnection site, the plasma density drops to the range $n \approx 1 \times 10^7 cm^{-3}$. The magnetic field strength in the reconnection outflow region is also an unknown, we therefore have to find a reasonable value either from the beneath SXR loop or from the global MHD simulation result that corresponds to the reconnection outflow. As described in the previous part, the direct evidence of outflow speed is very rare and also an unnegligible uncertainty of the magnetic field strength, the plasma outflow speed in the work is basically assumed to the value of Alfvén speed outside of the current sheet diffusion region.

The plasma density, both for electrons and ions, is chosen to be $n = 1.56 \times 10^7 cm^{-3}$ as the lowest value measured in the 30 active region loops (Aschwanden 1999), and this mimics the ambient density near coronal current sheet. The magnetic field strength outside the reconnection difusion region, before the magnetic tension relaxation, is assumed to be $B = 90G$ and this is not an unresonable value for the compressed current sheet of the solar active regions, e.g. the magnetic modeling of the preflare configuration revealed that a highly sheared fluxtube erupted and triggered reconnection with the overlying large-scale magnetic field (Zhang et al. 2000). The Alfvén velocity with these density and magnetic field strength is then $v \approx 5 \times 10^4 km \cdot s^{-1}$, and this is the assumed reconnection outflow speed in our simulation. The temperature of the outflow ions and electrons are assumed to be equal, and their temperatures are $T_i = T_e = 0.3MK$ which would not generate HXR nor radio emissions and this is not shown in real solar observation. With this temperature, the Debye length $\lambda_{De} = \sqrt{T_e/4\pi n_e e^2}$ is about $1cm$. To save the simulation time, we assume the mass of ions is $m_i = 9m_e$, hence the sound speed is therefore $v_s = \sqrt{T_e/m_i} = 7.2 \times 10^2 km \cdot s^{-1}$.

The setup of our 1D EM PIC simulation is shown in Fig.4.1. Because the obstacle of the coronal reconnection outflow, the SXR loop, is of higher density and magnetic field strength, charged particles are basically reflected back from their small gyro radii in collisionless plasma. To describe the plasma injected into simulation domain carrying magnetic field with, we deploy an initial electric field transverse to plasma drift motion. When plasma travels across the electric field, according to Ampere's law, it automatically generated a magnetic field perpendicular to both plasma drift and electric field.

When the plasma flows together with perpendicular magnetic field and reached the simulation reflective boundary, plasma is pushed backward to upstream of the flow, and a fast magnetosonic shock is generated because of the kinetic current driven instabilities. In the nonlinear stage of instability development, plasma acceleration and heating become

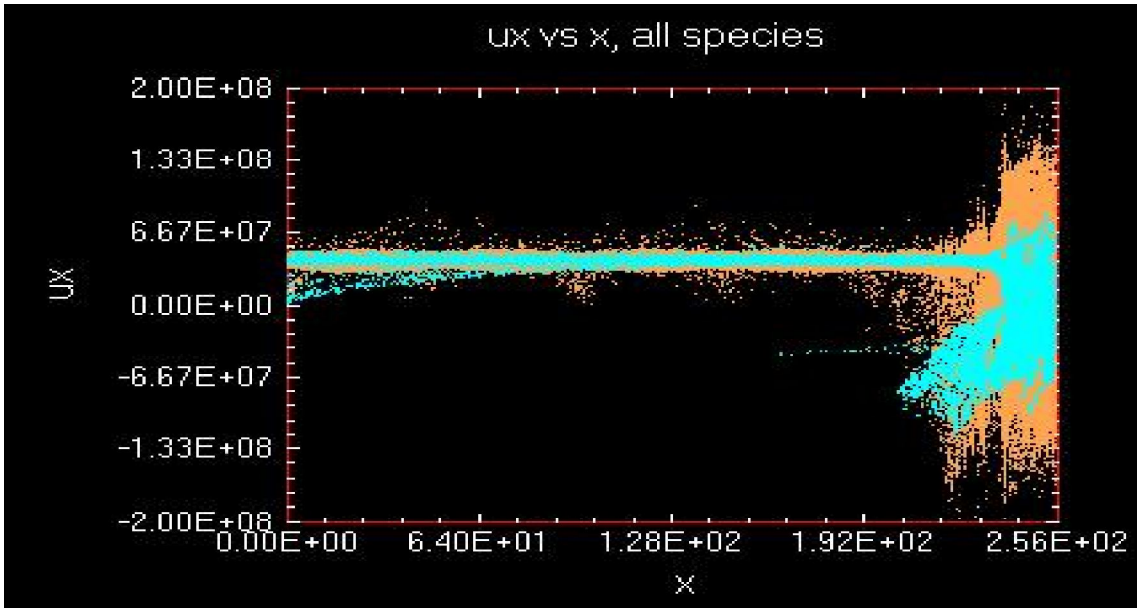

Figure 4.2: The phase space plot (X and UX) of electrons and ions in the final stage of simulation. The blue dots indicate ions and orange dots indicate electrons. It is clearly shown in the downstream of shock the temperature of electron and ions are much higher than the injected plasma.

the direct consequences of the kinetic effect of fast shock, which is the plasma dynamics revealed in kinetic approach but not in MHD shock study. The detailed kinematics of plasma acceleration is discussed in the next section.

4.3 Fast Shock Formation and Particle Acceleration

In our simulation, plasma that consists electrons and ions are injected from the left boundary. Because of a reflective boundary and the incoming magnetic field carried with plasma, magnetic field starts to accumulate from the reflective boundary and the reflected plasma drift together with the injected flow formulates the counterstreaming beams. Several phase space instabilities are possible to be triggered in this environment. With a strong relative motion, the electrostatic two-stream instability starts to appear. Electrostatic two stream instability is generally a wave-wave interaction between the two Doppler-shifted electron Langmuir waves, carried by incoming beam and reflected beam, and with exchanging momentum between these two species, hence the plasma phase-space structures are created.

For electrostatic stability analysis of a system that plasma dirft is perpendicular to the ambient magnetic field, the dispersion relation can be written as

$$1 = \Sigma\omega_{pj}^2(\omega_{*j}^2 - \Omega_j^2 cos^2\theta)[\omega_{*j}^4 - \omega_{*j}^2(K^2S_j^2 + \Omega_j^2) + K^2S_j^2\Omega_j^2 cos^2\theta]^{-1} \tag{4.1}$$

where θ is the angle between plasma drift and magnetic field, and S_j is the sound speed of species j.

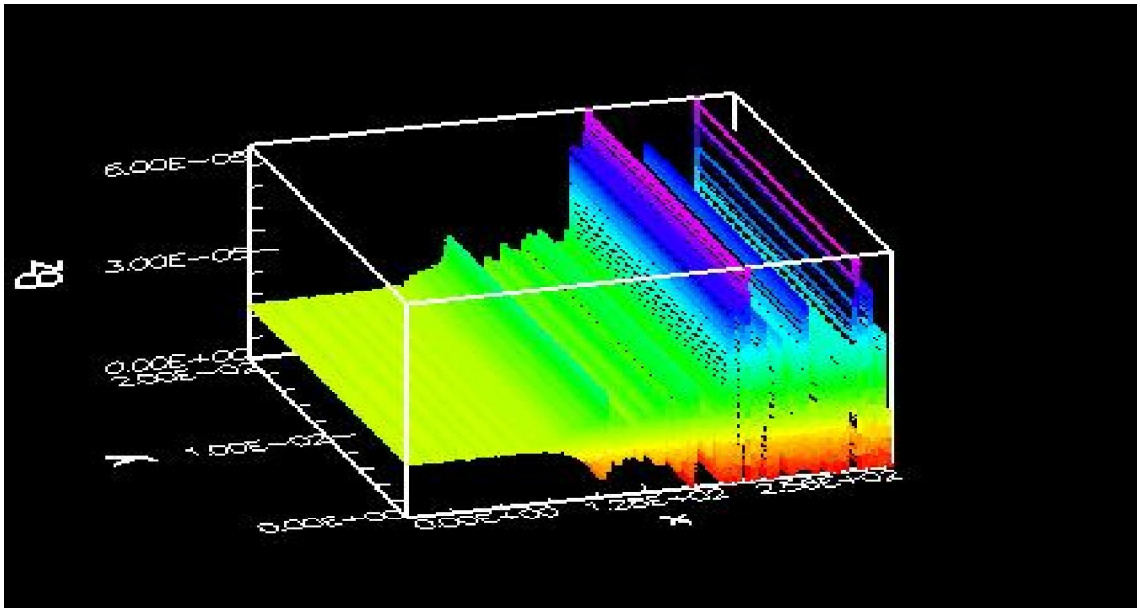

Figure 4.3: The magnetic field intnesity that is perpendicular to the plasma drifts. In the region close to to reflective boundary the magnetic field accumulates, showing a signature of fast magnetosonic shock.

From the injected plasma parameters as described, the strong plasma heating is observed in the late stage of simulation when the reflected beams interact with the injected beams. The original quasi-nonthermal plasma with temperature $T_i = T_e = 0.3MK$ is heated up to the level of $T \approx 100 - 1000MK$. This is shown clearly in Fig. 4.2. And also because of the generated strong electric field in the shock structure, the original injection plasma with $E = 7keV$ bulk kinetic energy is accelerated to $E \approx 120keV$. The temperature is the common observed coronal plasma temperature above active regions, and the bulk kinetic energy the accelerated plasma is also the typical value that is retrieved from the coronal footpoints HXR emission.

The magnetic field perpendicular to the plasma flow is shown in Fig. 4.3. This value is much larger comparing to the magnetic field along the drift direction, indicating this is a quasi-perpendicular shock. In the figure it shows that the magnetic field is accumulated in the shock and downstream region, which exhibits a signature of fast magnetosonic shock.

Since the simulation is of one dimensional assumption, we excluded the effect that plasma can flow out of the region freely along magnetic field line and the related injection mechanism is not considered. In a two dimensional configuration the location of fast shock can stay more or less the same distance from the obstacle, however in a one dimensional configuration the shock is propagating back to the injection boundary.

4.4 Conclusion

The plasma acceleration via a fast shock is investigated for solar corona parameters. With a reflective boundary that mimics the coronal SXR loop, the magnetic field carried by the injected plasma flow accumulated, and the reflected beam generates drift instabilities in

the shock find structures. Similar to many previous previous shock acceleration studies, which are mainly applied to explain the observed high energy ions in supernova remnants, we found the ion and electron heatings in the downstream of shock transition region.

For the simulation setup, the parameters of the injected plasma flow are basically assumed from the observations of the ambient environment, since the values from direct observations are difficult to obtain in this frequency range. The assumed velocity of the plasma flow is basically the Alfvén velocity outside the reconnection diffusion region.

A fast shock is generated between the injection and the reflective boundaries. The fast shock is efficient in accelerating charged particles, the original plasma with bulk energy of $7keV$ can be eventually accelerated up to $120keV$. Although the injection mechanism from the downstream to loop footpoints is not discussed in this one dimensional simulation, the energy level in the late stage shows the fast shock acceleration is a very good accelerator to explain the observed HXR spectrum.

5 Transport due to Current-Free Electrostatic Double Layers

5.1 Introduction

The forward-fitting of Hard X-Ray (HXR) observations provide a number of energetic electrons and the instantaneous electron flux of solar flares(Aschwanden 1999). The HXR emission from a flare can be characterised by its location either as coronal or as chromospheric. The coronal emission provides relatively low energy photons ($\leq 30keV$). Its characteristics are consistent with a hot quasi-thermal plasma radiation. The chromospheric 'footpoint' emission, on the other hand, is thought to be generated by a vast number of non-thermal particles accelerated during a flare (Fletcher 2005).

The electron spectra, deduced from the HXR observations, exhibit different power-law indices at the footpoints and in the upper corona. The footpoint X-ray fluxes, obtained by HXIS in a range of 16-30 keV (MacKinnon 1985), were found to be only $15-28\%$ of the fluxes obtained by extrapolating the same energy range from HXRBS spectra at higher energies of 25-300 keV (Zharkova 1997). These results indicate that electron dissipation must occur during the propagation, especially of the lower energy electrons, while the higher energy part electron spectrum stays approximately unchanged.

In a fully ionized plasma, a magnetic field is induced by the injected energetic electron-beam. According to Faraday's induction law, the magnetic field flux maintains as a constant in a perfectly-conducting environment. Hence, a backward propagating electron-beam is therefore generated by the induced electromotive force to cancel the flux change, and the generated return current compensates the injected beam current (Zharkova 1997).

In collisional model with Ohmic heating, return current energy losses in a fully ionised coronal plasma were shown to have a noticeable effect on the injected beam dynamics in depth, particularly at the chromospheric level (Emslie 1980). Hence, the electron interaction with induced electric fields may govern the beam dynamics. As a result, less energetic electrons might not reach the deep chromosphere, but loose their energy already in the lower corona (Aschwanden 2002).

The type of the excited electrostatic instabilities depends on the composition of beams and return-currents (Davidson 1983), i.e. on the ratio of their fluxes. The evolving unstable plasma waves can result into particle anomalous transport at nonlinear stage. Assuming a collisional thick target model (Brown 1971), the spectrum obtained from the solar flare on 23 July 2002, for example, suggested an instantaneous electron flux of more than $2\times10^{36}s^{-1}$ above 20 keV for 100 s (Holman et al. 2003). Taking the RHESSI source sizes, a conservative lower limit for the electron flux is $2.6\times10^{18}cm^{-2}s^{-1}$. For a beam speed of

the order of $10^{10} cms^{-1}$, this implies a beam-electron number density of $2.6 \times 10^{8} cm^{-3}$. In all likelihood the area is a factor of 5 to 10 lower, and the electron flux per unit area is 5-10 times higher (Fletcher 2005). This means that beam number density and the coronal background number density are, perhaps, comparable.

A stability analysis of a dilute beam plasma system ($10^{-4} < n_b/n_p < 10^{-1}$) of the excitation of Langmuir waves was carried out by Rowland & Vlahos (1985). In the case of a higher beam density ($n_b/n_p \sim 0.2$) electron-acoustic waves become unstable (McQuillan & McClements 1988). The possible excitation of low-frequency ion-acoustic and ion-cyclotron waves by dense beams was studied in (Cromwell et al. 1988). Numerical simulation studies have shown that ion-acoustic (Büchner & Elkina 2005) and electron-acustic waves can heat the plasma. This causes an efficient dissipation of the electron flux through energy conversion.

Electron beam instabilities can lead to the development of electrostatic Double Layers (Büchner & Elkina 2006). DLs are unique nonlinear electric field structures in free-energy supplied environments. An ideal DL consists of an unipolar electric field, i.e. it exhibits a monotonic potential drop, and the charge neutrality condition is violated locally (Langmuir 1929). Dynamically, however, DLs are formed by accumulating electron phase space holes which are characterized by bipolar electric fields (Block 1977). A sufficient condition for a DL structure is a net potential drop through the entire layer. For electrons with energies less than the first potential ramp a DL provides an obstacle, which would stop the electrons at the ramp. The stagnation of the electron flow can dissipate the flow energy and heats the reflected electrons. In order to describe a basic feature of DLs, the local charge separation, at least a multifluid approach is required.

Double layers in current-free beam plasma, where a dense beam is neutralized by a return-current, are studied in the laboratory (Hairapetian & Stenzel 1990). Current-free DLs in solar coronal plasma were considered, e.g., in (Alfven & Carlqvist 1967); Khan (1989); Boswell et al. (2006). A combined action of anomalous resistivity and DLs was proposed to explain the dissipation of cosmic jets (Borovsky 1986). An analytical model of the diffusive acceleration of particles in auroral plasma due to interaction with weak double layers was developed by (Lotko 1986). Auroral electron acceleration by double layers was considered, e.g., by (Borovsky 1992). Auroral acceleration requires multiple weak double layers, organized in a chain along the field lines, to form a sufficently large total potential drop. Generally double layers can effectively accelerate electrons and cause a complicated nonlinear dynamics in the system, which has to be studied by means of numerical simulations.

A numerical study of DLs with semi-open boundary condition was performed by (D.L. Newman 2001). They intended to explain the ionosphere DC parallel electric field observed by the FAST (Fast Auroral SnapshoT) satellite (Lynch 2001). The dynamics of electron holes, created by an ion-acoustic instability, was discussed therein. The formation of DLs as a result of the nonlinear development of an electron current-driven instability was studied by means of a Vlasov code simulation (Büchner & Elkina 2006).

It is an open question, however, through which mechanism DLs are created in a return-current beam-plasma system, that is typical for the solar corona. Also, it is unclear that what is the precise mechanism of energy conversion from bulk current kinetic energy to electrostatic wave energy and, at later stages, to electron and ion thermal energy via the interaction with DLs.

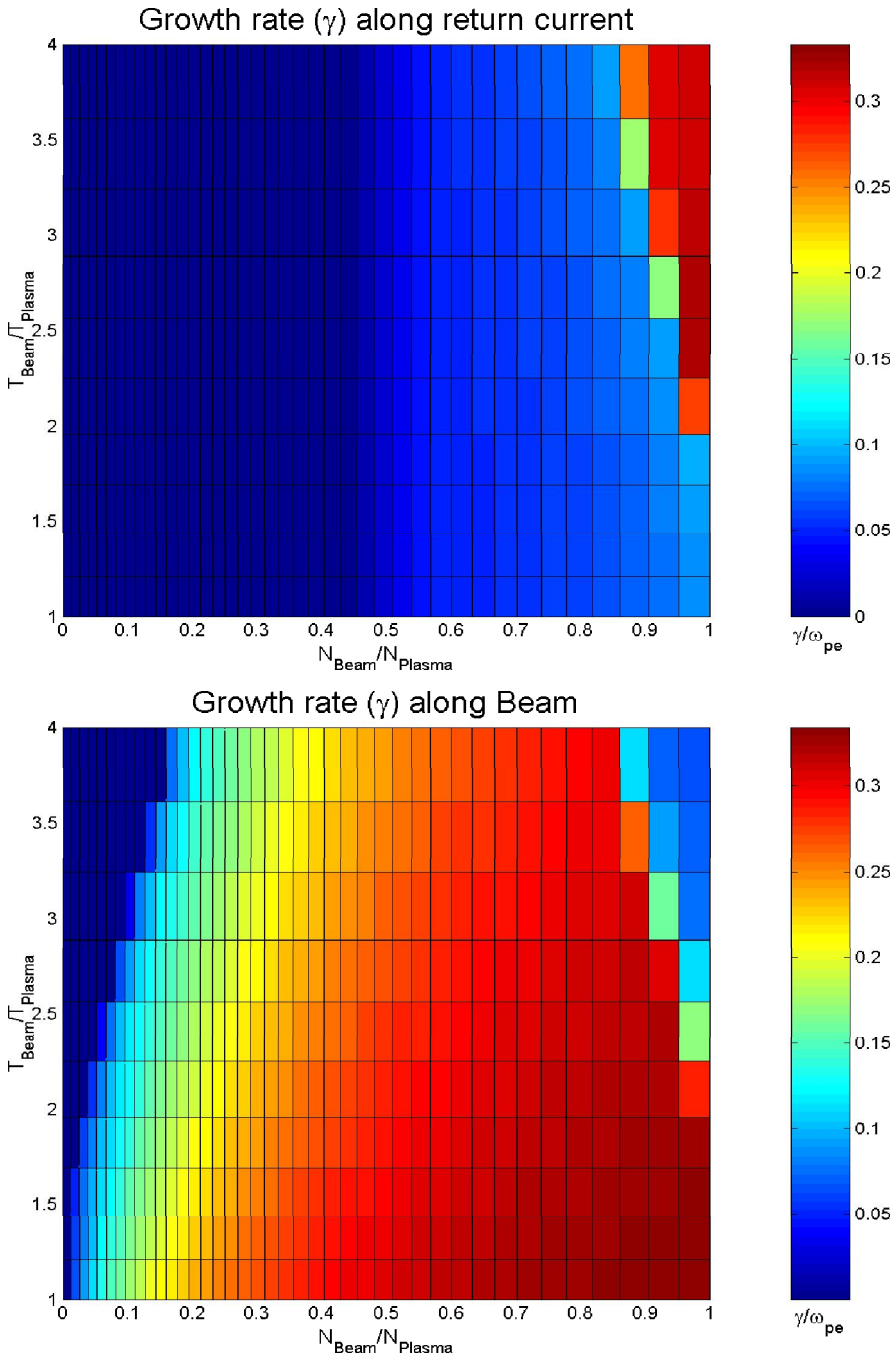

Figure 5.1: The normalized largest growth rates of waves propagating along beam and return-current directions shown as functions of density and temperature ratio for the real mass ratio of electrons and ions ($m_i/m_e = 1836$). Larger growth rates correspond to electron-electron acoustic (EE) mode while smaller growth ones correspond to the ion-acoustic (IA) mode.

Our goal is to analyze the stability of return-current beam plasma system in the solar corona and to investigate the consequences of the resulting wave-particle interaction, i.e whether it might explain the broken-power-law electron spectrum retrieved from solar HXR observations.

In section 5.2, we carry out a linear dispersion analysis for the most probable coronal parameters. To consider the nonlinear instability evolution, we performed a 1D Vlasov-code simulation and also its spectral analysis. These results are presented in section 5.3. At the nonlinear stage of the DLs evolution, fast electron holes are formed after electrons are accelerated by DLs. The dynamics of this unique phenomenon is discussed in section 5.4. There we discuss also the heating of ions and electrons. To address the formulation of the broken-power-law spectra and the discrepency of electron distributions retrieved from both footpoint- and coronal emission, the dissipation and relative anomalous transport characteristics of electrons are discussed in section 5.5.

A brief summary and a discussion of the implication of our results for the solar corona are given in section 5.6.

5.2 Basic Equations and Linear Dispersion Analysis

A counter-streaming return-current beam plasma becomes unstable and the generated waves dissipate the electron bulk motion, even though their net current is zero. To study the dispersion characteristics of this system a multifluid model is considered.

We assume a current and charge-neutrality system, i.e

$$\sum_{\alpha} q_\alpha N_\alpha = 0 \qquad \sum_{\alpha} q_\alpha N_\alpha V_{d\alpha} = 0 \tag{5.1}$$

where N_α represents the densities of the beams, $V_{d\alpha}$ is the mean velocity in the beam flow direction and $v_{t\alpha}$ is the thermal velocity of the beam electrons. For collisionless plasma, large amplitude electrostatic waves have strong influence on the anomalous momentum transport property, hence the electrostatic condition ($\vec{b} = (c/\omega)\vec{k} \times \delta\vec{E} = 0$) is assumed, which indicates $\vec{k} \parallel \vec{E}$.

The dispersion relation of electrostatic linear perturbations in the return-current beam system is:

$$1 = \frac{\omega_{pi}^2}{\omega^2} + \frac{\omega_{p,Beam}^2}{\left(\omega_{*Beam}^2 - k^2 S_{Beam}^2\right)} + \frac{\omega_{p,RC}^2}{\left(\omega_{*RC}^2 - k^2 S_{RC}^2\right)} \tag{5.2}$$

A basic beam-plasma fluid-like instability is the Buneman mode (Buneman 1958) (or ion-acoustic (IA), if thermal corrections are considered). In a return-current system, however two electron populations exist. Their relative drift may cause also an electron-acoustic instability (Gary 1993).

To identify the different possible excitation mechanisms, we performd a sub-system dispersion analysis. In the beam-plasma system (without the third term on the righthand side of eq. (5.2)) and the return-current beam plasma system (without the first term on the righthand side of eq. (5.2)), the ion-acoustic (IA) and the electron-electron two stream instability (EE) can be recognized respectively via a detailed comparison of growth rates

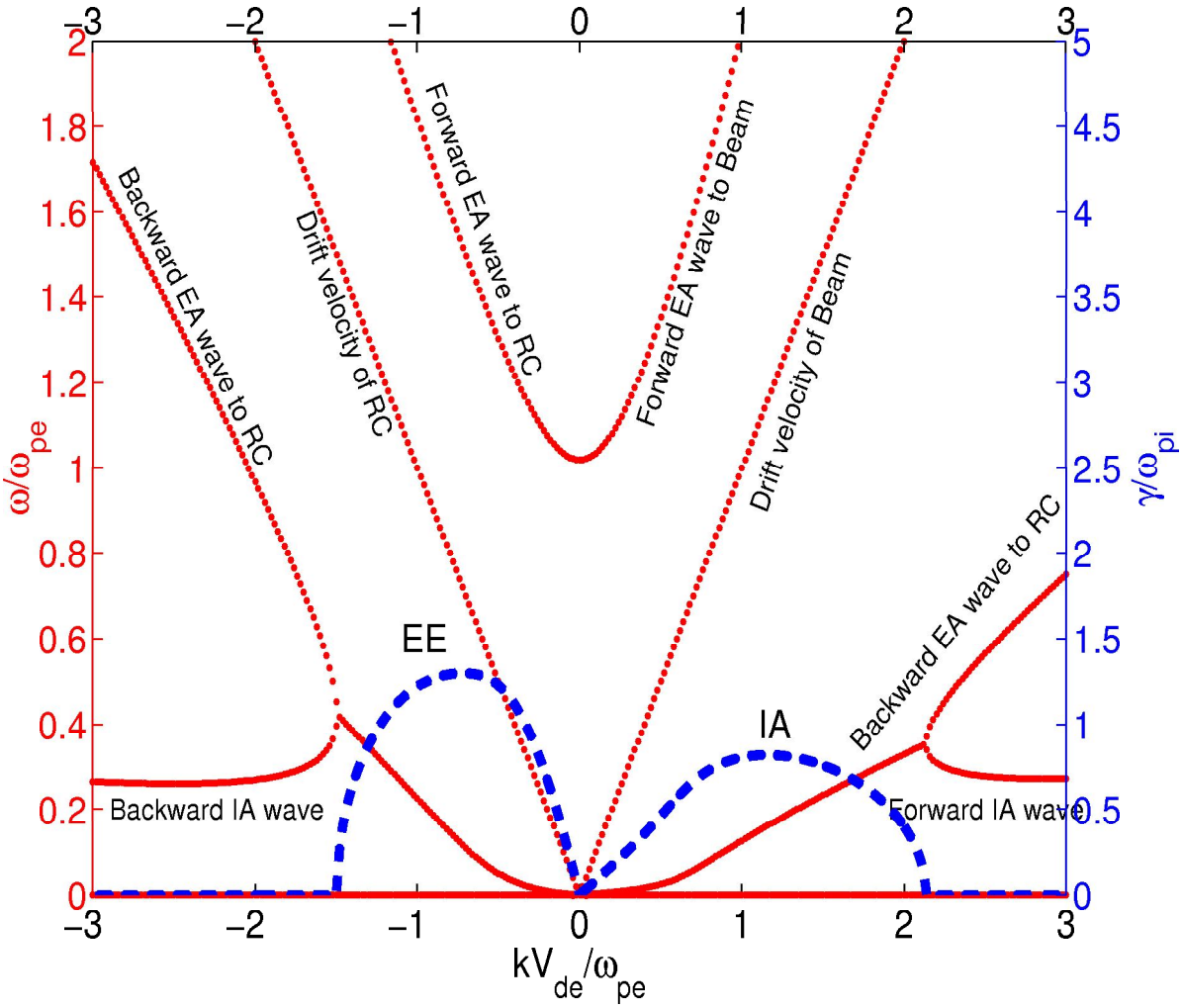

Figure 5.2: Dispersion relations for $m_i/m_e = 25$. Wave frequencies (red dotted lines) and growth rates of unstable modes (blue dashed lines) in a warm return-current beam plasma.

and dispersion characteristics. The electron-electron coupling (EE) leads to a much higher growth rate if the real mass ratio is applied.

We solve the linear dispersion equation (5.2) for the parameters of solar coronal loops, with the real mass ratio ($m_i/m_e = 1836$) to find the dominant mode in the system. In Fig. 5.1, the growth rates along the directions of beam and return-current are shown as functions of density and temperature ratios. For isothermal beam and return-current ($T_{Beam}/T_{Plasma} \approx 1$) ion-acoustic mode is excited along return-current direction and an electron-electron (EE) two-stream instability in the beam direction. Beams ejected from the primary acceleration sites can, however, be heated along the path of propagation before interaction with the background plasma. Hence, the dependence on the temperature ratio has also to be studied.

For larger temperature ratios ($T_{Beam}/T_{Plasma} > 1$) and comparable electron densities of the beam and return-current ($N_{Beam}/N_{Plasma} \approx 1$), the IA and EE mode switch their propagation directions. The energy transport of Doppler-shifted electron acoustic waves

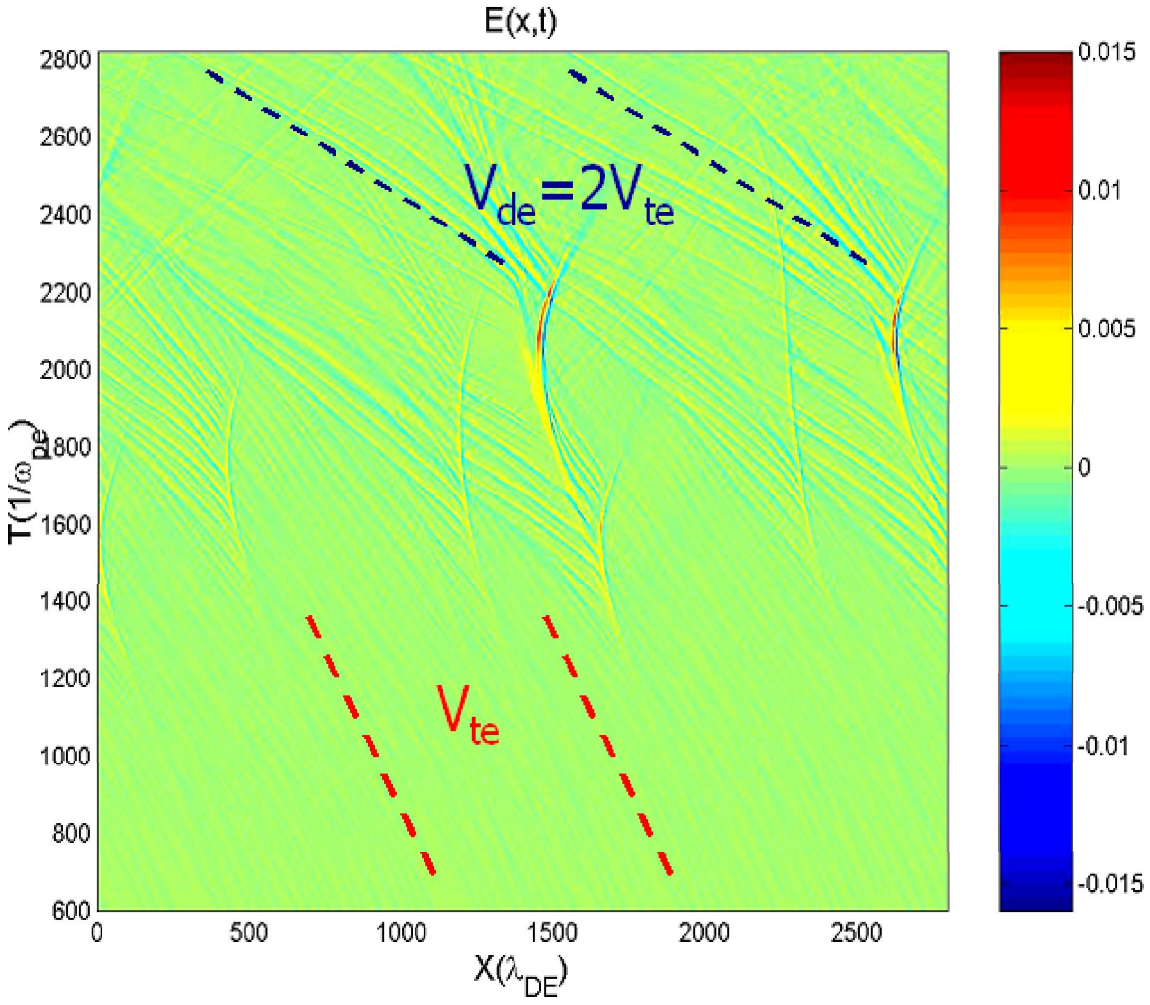

Figure 5.3: Electric field history $E_x(x,t)$. Double layers appears at $T\omega_{pe}^{-1} = 1400$. Two pronounced phase velocities are (1) the original electron-acoustic waves velocity V_{te}, and (2) the velocity of fast electron holes $V_{de} = 2V_{te}$

of beam and return current can be clarified by analyzing the coupling of the waves.

In order to compare with numerical simulation results, we carried out a linear dispersion analysisa for a mass ratio ($m_i/m_e = 25$). The result with reduced mass ratio is shown in Fig. 5.2. With the assumed electron temperature and current density of solar flares (Aschwanden 2006), the thermal velocity of electron $V_{te} \approx 2.58keV = 5 \times 10^9 cm \cdot s^{-1}$ and the bulk velocity of the beam is $V_{de} \approx c/3 = 1 \times 10^{10} cm \cdot s^{-1}$ (Kudriavtsev 1989);Fletcher (2005). During flares the beam temperature increases several times above the coronal plasma (Aschwanden 2006), hence we assume that the thermal velocity of the beam is twice the thermal velocity of the return-current:

$$\begin{aligned} V_{d,Beam} &= -V_{d,RC} = 2V_{th,RC} \\ V_{th,Beam} &= 2V_{th,RC} = 2V_{th,ion} \end{aligned} \tag{5.3}$$

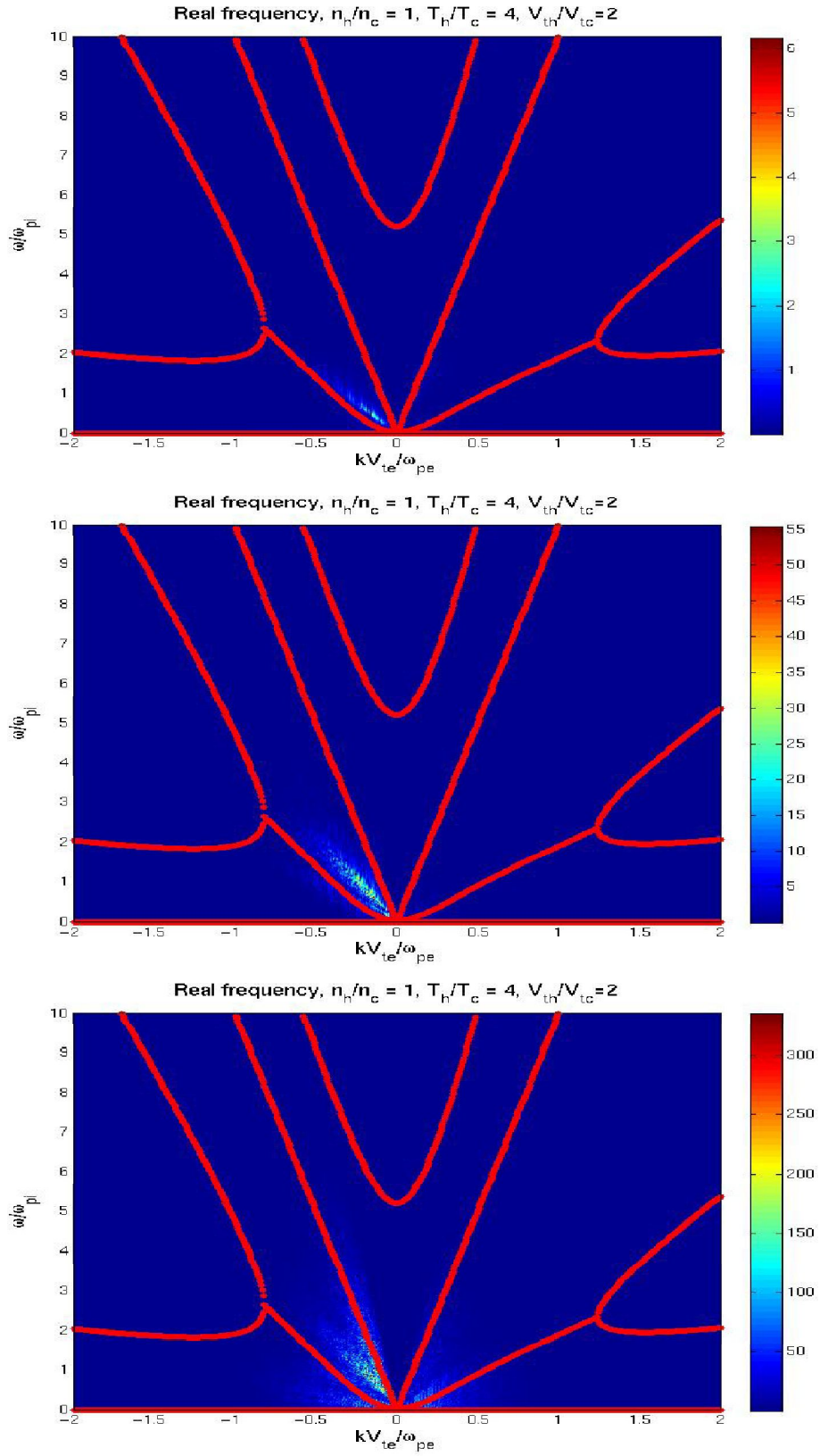

Figure 5.4: The spectra of simulation at different time are shown in each panels, 1) T: $0 - 700\omega_{pe}^{-1}$ 2) T: $0 - 1400\omega_{pe}^{-1}$ 3) T: $0 - 2800\omega_{pe}^{-1}$. The color-coded indices show the 2D FFT transform coefficient. On nonlinear stage fast electron holes appear, and propagate at velocity of return-current drift $2V_{te} = V_{de}$

$$N_{RC} = N_{Beam} = N_{ion}/2$$

The dispersion analysis reveals two unstable waves modes (see Fig. 5.2). Along the directions of the reverse current (negative K) an electron-acoustic wave propagates due to an electron-electron two-stream instability. The maximum growth rate $\gamma \simeq 1.5\omega_{pi} \approx 1/3\omega_{pe}$ is the characteristic growth rate of the resulting electron-electron two-stream instability, which is from a coupling of the forward propagating beam electron-acoustic wave and backward propagating return-current electron-acoustic wave.

Along the beam direction (positive K) an ion-acoustic (IA) wave grows unstably due to a coupling between the backward propagating beam electron-acoustic wave and the forward propagating ion-acoustic wave, and the maximum growth rate is $\gamma \simeq \omega_{pi}$. The wave frequencies are depicted by red dotted lines, and their growth rates are depicted by blue dashed lines. (Note that in our analysis the injected beam propagates in the positive direction)

The growth of unstable waves continues until the free energy of the system is reduced to marginal instability conditions. In order to study the resulting wave-particle interaction and the nonlinear evolution we use a fully kinetic 1D Vlasov code simulation.

5.3 Double Layer Formation and Spectrum Analysis

The evolution of an electron beam instability was investigated by means of an one-dimensional (1D) electrostatic Vlasov-Ampere code (Elkina & Büchner 2006). The code is based on an unsplit conservative finite-volume numerical discretization scheme, and it uses an open-boundary condition to study the evolution of the current-driven instability.

To study the nonlinear evolution of DLs in a current-neutralized beam plasma, we performed a simulation with the same parameters as in dispersion analysis (equation 5.3), i.e., a hot electron beam and an ambient cooler return-current electron drifting in the opposite direction to maintain the current neutrality condition. Both beams are modeled by drift-Maxwellian distributions. Ions forms a stationary background at the beginning of the simulation with a Maxwellian distribution.

We use an moderate artificial mass ratio $m_i/m_e = 25$ to distinguish the difference in ion and electron motion. The assumption of an artifitially low mass ratio is necessary to allow the ions to respond within a resonable simulation time. The length of the simulation domain is $3200\lambda_{DE}$. With typical solar flare parameters, this corresponds approximately to $\simeq 12m$ in a $10^7 m$ flaring coronal loop (Aschwanden 2006). A periodic boundary condition is a reasonable and sufficient assumption for a such long system.

DLs can be created at the nonlinear stage if the Bohm condition (Bohm 1949) is satisfied, i.e.

$$j_c = ne\sqrt{2kT_e/m_e} \tag{5.4}$$

which is satisfied for the solar flare plasma parameters used in our simulation setup (equation 5.3).

The simulation is performed until ($T = 2800\omega_{pe}^{-1}$), which allows to investigate the complete evolution of DLs. The spatial-temporal evolution of the electric field is shown in Fig. 5.3. During the linear stage ($T \leq 700\omega_{pe}^{-1}$) the electron-acoustic waves (EE-mode)

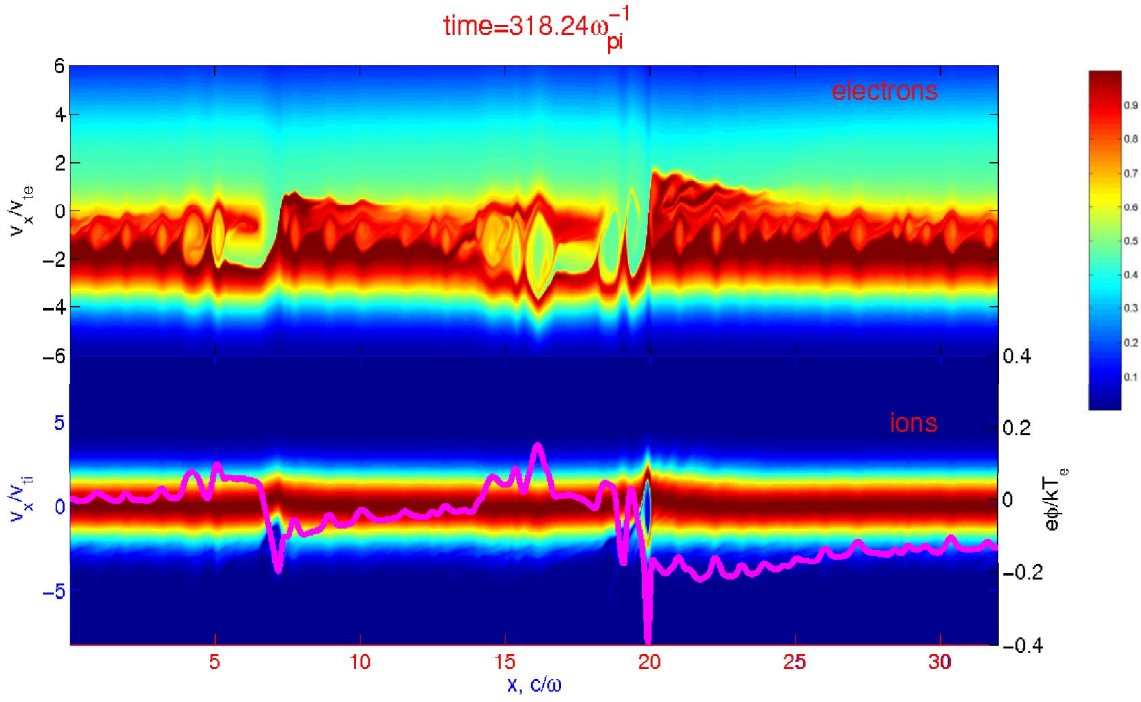

Figure 5.5: Electron and ion phase spaces are given at time $T = 318\omega_{pi}^{-1} = 1590\omega_{pe}^{-1}$. Electric field potential $e\phi/k_BT_e$ normalized by electron temperature is shown by solid line.

appear first in accordance with the linear stability prediction (see Fig. 5.2), which propagate along the return-current direction.

The nonlinear stage of the instability is characterized by the apperance of double layers. As one can see in Fig. 5.3 multiple double layers are created and later dissipated. Their life-time is about $T_{life} \sim 800\,\omega_{pe}^{-1}$. All double layers initially, during the first half of their life-time, move in the direction of the return-current electron flow. In the second half of their life-time DLs change their direction and start to move in the beam direction. A similar behaviour of double layers was observed in two-ion population plasma used to simulate auroral weak double layers (Yajima & Machida 2001).

The characteristics of unstable waves and nonlinear structures, their frequencies and wave numbers, can be obtained via a spectral analysis of the generated electric field for different time intervals.

Fig. 5.4 depicts the spectra for the simulation intervals (1) T : $700\omega_{pe}^{-1}$; (2) T : $1400\omega_{pe}^{-1}$ and (3) T : $2800\omega_{pe}^{-1}$. The color-coding indicates the spectral intensity of the modes

$$A(k,\omega) = \sum_{n=0}^{N-1}\left(\sum_{s=0}^{M-1} a(x,t)e^{\frac{-2\pi i}{M}s\omega}\right)e^{\frac{-2\pi i}{N}sk} \tag{5.5}$$

The wave frequencies obtained by the linear dispersion analysis are superposed (red curves) in Fig. 5.4. At the linear stage (1) one can see that the first excited wave is propagating in the direction of the return-current (negative $\vec{K}$). This agrees with the prediction

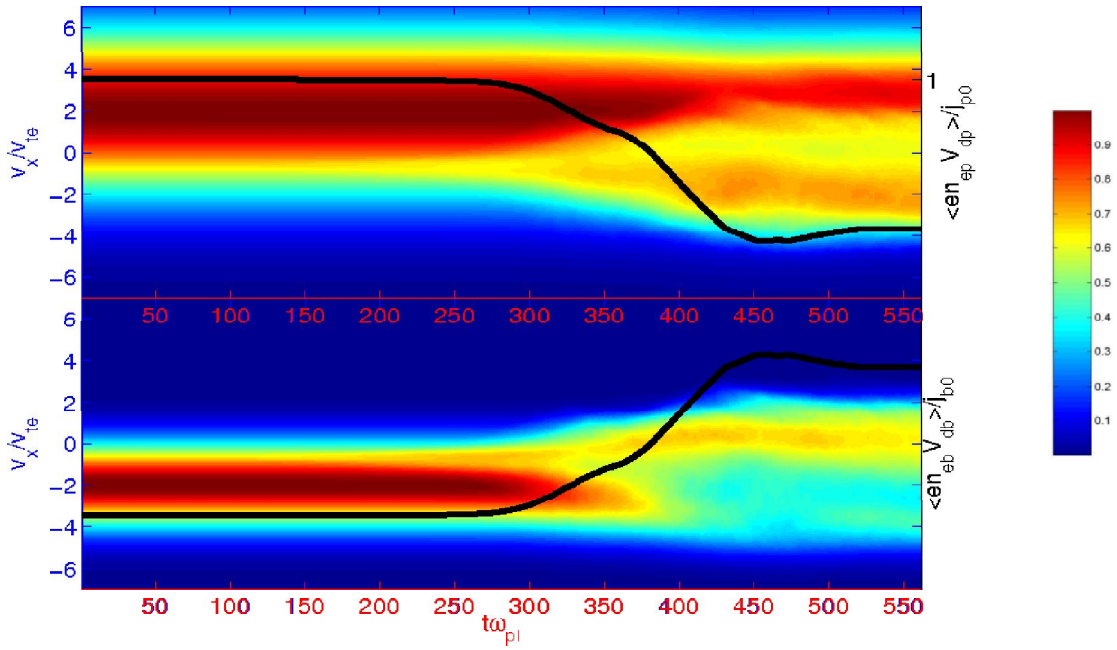

Figure 5.6: Spatially averaged electron distribution function corresponding to beam and plasma. Averaged current contribution are shown by continious line.

of the linear theory that EE mode grows faster. The second period (2) corresponds to the appearance of DLs. The excited wave spectrum is broader both in wave numbers as well as in frequency. Note that the phase-velocity of unstable waves increases but does not reach the drift velocity, yet.

Before stage (3) DLs start to decay and, consequently, the fast electron holes generated by the double layers take over the global dynamics of the simulation in this third phase, already as post-products of the interaction with DLs.

5.4 Dynamics of Fast Electron Holes

A real DL consists of several asymmetric bipolar electric field structures which all together cause a net potential drop. DLs primarily affect electrons in two ways: (1) As the phase space structures shown in Fig. 5.5 near $X = 20(c/\omega_{pe})$ and $X = 8(c/\omega_{pe})$, the first potential dip on the positive side of DL stops low-energy electrons since electrons are accelerated toward the higher potential side. (2) The overall potential difference accelerates those electrons that are able to cross the first barrier.

Contrary to the initial electron-acoustic waves (EE) generated by the interaction of beam and return-current electrons at the linear stage, fast electron holes result from a secondary electron two-stream instability via the interaction of DLs-accelerated return-current electrons with the background low speed return-current electrons. In the simulation interval shown in Fig. 5.5, the generation of fast electron holes is in the intervals

$X = 15 - 18(c/\omega_{pe})$ and $X = 5 - 7(c/\omega_{pe})$.

The additional third electron beam is created by the DL, with its own chracteristic drift and thermal velocities. To analyze the fast electron holes triggered by the third electron beam, we performed a sub-system dispersion analysis in which the thermal spread and drift difference of DLs-accelerated return-current electrons and the background low speed return-current electrons are considered. The rough estimate of the resulting secondary two-stream instability caused by the third beam shows that the electron holes should propagate at a speed of ($V_{Holes} = 2V_{te} = V_{de}$) to the background ions. This explains the observed phase velocity of the fast electron holes. Note that the calculated potential drop in Fig. 5.5 is normalized by initial thermal energy of electron beam, and the potential drop at this stage is around ($e\phi/kT_e = 0.4 \simeq 103.6eV$), showing the characteristic of a weak DL.

5.5 Plasma Heating and Anomalous Transport

The energy transfer is always an attractive topic in solar coronal studies. During flares, evolution of the plasma distribution takes place in the beam precipitation from the upper corona to the chromosphere. The question to be addressed is: Can the broken-power-law spectrum be explained by the energy and momentum transfer due to the excitation of DLs?

Consider both the energy range of Hard X-Ray emissions ($\geq 5keV$) and Soft X-Ray emissions ($< 5keV$). The HXR mostly are generated via thick-target bremsstrahlung while SXR result from free-free electron scattering. A consequence of plasma heating in coronal loops are the bright emissions of soft X-rays and extreme ultraviolet (EUV) radiations. Coronal HXR emissions correspond to low photon energies ($< 30keV$), and their characteristics are consistent with the radiation from a hot quasi-thermal plasma. Instead the chromospheric 'footpoint' emission is thought to be generated by a vast numbers of non-thermal particles accelerated during a flare.

Let us further assume that the electrons are beamed from the primary acceleration sites at the topside of coronal loops, the electron spectra are primarily nonthermal (Antonucci 1995). Then the observed coronal thermal emission in the collisionless coronal plasma should be generated through dissipation of the original nonthermal electron beam.

The simulated evolution of the space-averaged distributions of beam electrons as well as of the return-current electrons is depicted in Fig. 5.6. One can see the space-averaged distribution of the original non-thermal beam ($V_{de} > V_{te}$) exhibits heating after the appearance of DLs at $T = 1400\omega_{pe}^{-1} = 280\omega_{pi}^{-1}$. A similar behavior is observed in the space-averaged distribution of the return-current, which can be seen in the lower panel of Fig. 5.6. As one can see in the figure DLs can inhibit the bulk motion of electrons. This is not the behavior of ideal DLs that consist only of a potential drop. The separately concerned plots of electron distributions shows that the direct beam- and return-currents are enormously slowed down, while the non-thermal distribution is broadening. This affects mostly the lower energy part of electrons which contribute rather to the generation of SXT and coronal HXR. Another interesting point to notice is that the higher energy part of the direct beam is not incfluenced too much, which might explain the nonthermal chromospheric HXR sources. Note that (Zharkova 1997) drew a similar conclusion that

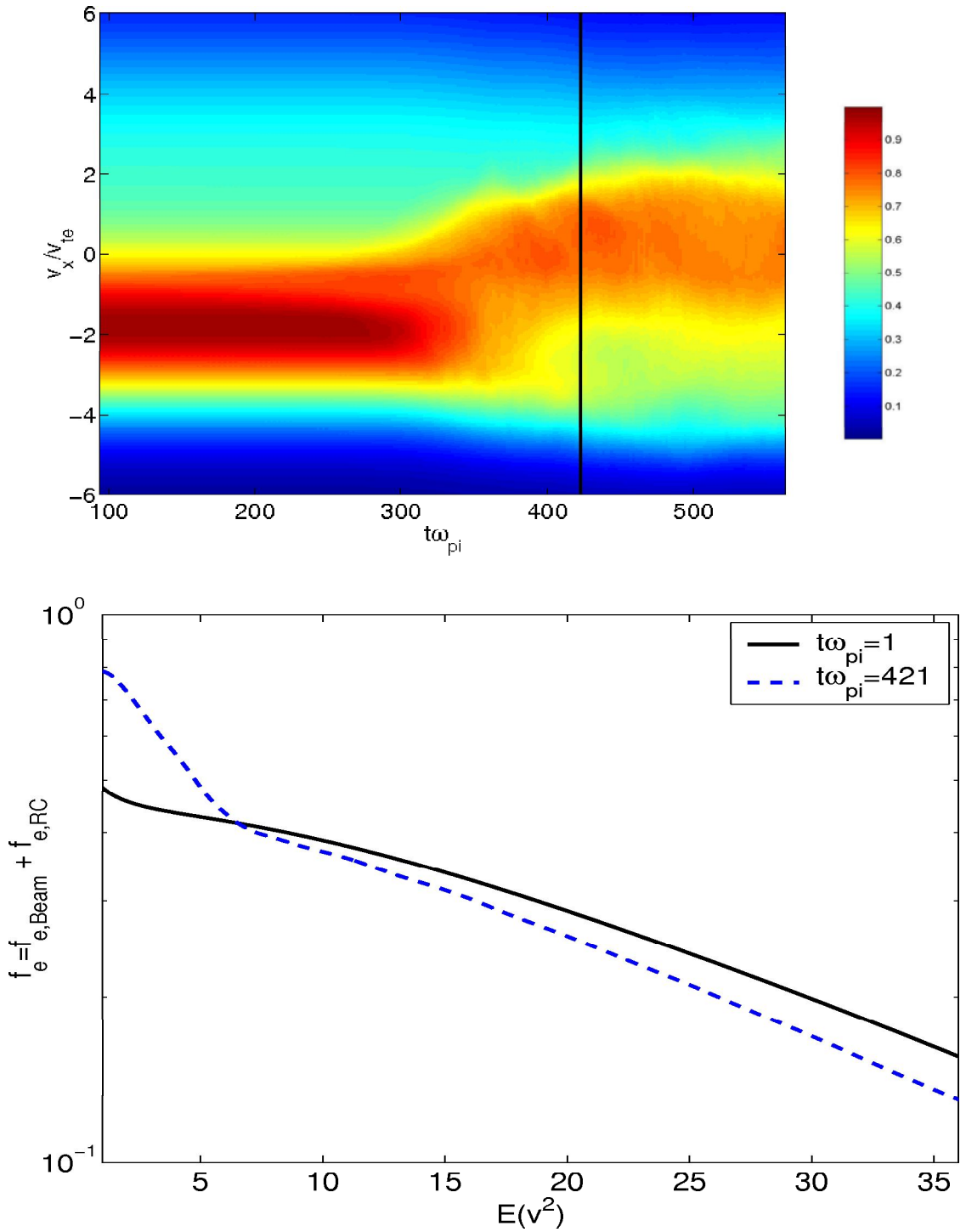

Figure 5.7: Combined spatially-averaged electron distribution function of beam and return current. For the right panel, the space-averaged downward-propagating ($V_x \geq 0$) distribution function at ($T = 421\omega_{pi}^{-1}$) is shown in blue dashed line, while the initial distribution is shown in black solid line.

the return-current mainly results into electron density depletion and the spectrum flattening at low energy part, with using their CEM model (Collisional, Electric and converging Magnetic field).

Consider their effects on electrons, we suggest that DLs play a role as an energy converter that transfers the original bulk energy of beam into thermal energy. The same effect is true for the return-current. After DLs transformed the electron drift energy into thermal energy, they gradually fade away. The reason is that the acceleration of fast electron holes takes away electric field energy. DLs disappear when free beam energy drops to the marginal threshold of any instability. In Figure 5.6 the averaged electron motion of individual species, their currents, are shown as black solid lines. The heavier background ions are also thermalized meanwhile.

To understand the observed HXR broken-power-law spectrum, we look at the combined space-averaged distribution of beam and return-current. As one can see in Fig. 5.7, a considerable amount of return current electrons is dragged along by the beam toward the positive propagation direction after the appearence of DLs ($T = 421\omega_{pi}^{-1}$). This results in a total density increase of the downward-propagating electrons (positive V_x), especially in the low energy range. The right panel of Fig. 5.7 shows the space-averaged distribution at simulation time $T = 421\omega_{pi}^{-1}$ in blue dashed line, comparing with the initial distribution in black solid line, the low energy electron for the downward-propagating part (positive V_x) has a higher density than higher energy range, hence we obtained a broken-power-law spectrum at the late stage of electron beam evolution. Note that the initial thermal velocity of return current electron is $c/6$, which is also the normalized velocity in simulation, therefore the normalized energy in the spectrum is around $7keV$. To compare with the observed HXR spectrum, our spectrum of electron distribution evolution from simulation agrees in non-relativistic energy range, e.g. the normalized energy $E = 16$ corresponds to $112keV$ in flare HXR spectrum.

The plasma environment we simulated here is the quasi-homogeneous part of the coronal loop above the transition region. Below the transition region the plasma density has strong density gradient. The impact cross section depends on the background plasma density and the incoming electrons, with different drift energy, should cause emission peaks at different altitude in chromosphere, as shown in Fig. (4) of (Aschwanden 2002). If this electron beam created at the late stage of the nonlinear beam evolution can further travel down to the chromosphere by maintaining this distribution characteristics, it eventually radiates HXR through collisional Bremstrahlung. Since the downward-propagating electron is dense in low energy part, two indeces are required for the drift-Maxwellian distribution fitting, hence revealing a broken-power-law energy spectrum.

5.6 Discussion and Conclusion

In order to understand the evolution of electron spectrum in the solar corona we have investigated the interaction of a precipitating beam of energetic electrons with its self-generated return current. For this purpose we have carried out a linear instability analysis and an one-dimensional Vlasov code simulation of a return-current beam plasma system for typical coronal parameters.

In preceding studies, instabilities in beam-current systems are usually considered of

ion-acoustic type (Watt et al. 2002); (Büchner & Elkina 2006). This is the case of only one electron beam in the system. An energetic electron beam in the corona will, however, induce an oppositely directed return current flow which maintains the current-free condition. Our sub-system dispersion analysis, applied to coronal plasma parameters, shows that forward and backward unstable waves are generated by different origins. In addition to an ion-acoustic instability along the original electron beam direction, an electron-acoustic two-stream instability is excited along the return-current direction. The later one has larger growth rate and dominates the linear stage.

To consider the nonlinear instability evolution and wave-particle interaction of the saturated state, a Vlasov code simulation was performed. We found that multiple double layers develop in the system. Spectrum analysis of the generated electric field allowed us to analyze the evolution of the nonlinear structures out of the linear instability phase, the so called double layers (DLs).

After the appearence of DLs also fast electron holes also appear. Due to electron acceleration by the DLs. As post-products of DLs, these fast electron holes propagate at the drift velocity of the return-current. The phase velocity estimate from dispersion analysis and from the spectrum analysis shows that the fast electron holes result from a secondary electron two-stream instability which are generated by the self-interacting return-current electron beams. The unique generation mechanism of this nonlinear dynamical phenomenon has not been reported in the previous study of beam and return-current system. We conclude that in a current-free return-beam coronal plasma fast electron holes are generated from a secondary two-stream instability.

Note that this mechanism would also appply to the observed topside ionosphere fast electron holes if the plasma comprises of a drifting beam and background ions. Indeed, space plasma observations of the FAST (Fast Auroral SnapshoT) satellite have discovered a variety of nonlinear localized electric field structures in the auroral ionosphere. Isolated bipolar field structures have been observed in the downward current region where they have been interpreted in terms of electron phase-space holes moving upward at speeds on the order of electron drift velocities (Ergun 1998). Our analyses have revealed a similar behavior of fast electron holes for the solar coronal condition at the late stage of evolution that propagate at the drift speed of the return-current.

But, mainly, our results can explain the deduced electron beam density of the chromospheric footpoints (Fletcher 2005) and the commonly observed broken-power-law HXR spectrum of the solar corona.

Since the return-current is a reasonable assumption in coronal loops because of the ejected electron beam propagates through a fully ionized plasma, DLs are expected to generate and influence the electron transport in the beam and return-current system. As shown in the individual space-averaged distribution of beam and return-current electrons, we found that higher energy beam electrons are not influenced very much but lower energy beam electrons are. The kinetic energy of the slowed-down beam electrons changes the electron propagation direction of return-current. As a consequence, the combined electron distribution clearly exhibits a density increment of downward-propagating electrons (positive V_x). Hence, we suggest that the observed broken-power-law spectrum is a natural consequence of the interaction of beam electrons with the self-generated current-free DLs.

6 Summary

The plasma transport properties in the collisionless solar corona environment have been extensively studied in this thesis. The influence of the collisionless transport was first investigated in this work from the key mechanism that triggers a coronal reconnection, the origin of the anomalous resistivity in the coronal current sheet, then it follows the particle acceleration via the collisionless looptop fast shock. In the last chapter we also demonstrate that the common observation of broken-power-law HXR spectrum is simply a result of plasma collisionless interaction with the self-generated electrostatic double layers.

One of the main results in this collisionless transport study is the derivation of the general multifluid dispersion relation. This general dispersion relation allows a plasma stability analysis in the linear stage, and it also help us on the identification of the unstable waves that in later stage creates the plasma phase space structures, which can eventually cause great influence to the characteristics of plasma transport.

The primary conclusions of each chapter are summarized into following:

1. Electrostatic instabilities generated by multifluid drift motion

In a free energy supporting plasma system, instabilities take place to bring the energy state back to equilibrium. In a multifluid plasma consideration, the relative drift motion between each species plays the role as the supporting free energy. From the derived ganeral dispersion relation in section 2.1 the system evolution tendency was analyzed. The derived dispersion relation is the extension of many previous works, and the breakthrough points of this equation is the consideration that excludes many further assumptions, such as a specific propagation angle, the cold plasma or electrostatic wave limits. Because the dispersion relation considers also the relative motions the growth rates of feasible instabilities can also be calculated instead of the wave frequencies only.

Because of the phase space structures generated by the electrostatic instabilities, magnetic reconnections can be triggered in collisionless plasma environment. We also focus on the idetification of instabilities. A "sub system" method that can use to distinguish the origin of instability is also developed.

In an one dimensional beam plasma system, two of the famous instatilities, the ion acoustic instability and Buneman instability, are discussed to share the same characteristics and they are just the two revilements of same mode, one is considered from kinetic point of view and the other from fluid limit. We further argued, from the kinetic theory derivation, that the multifluid description of plasma contains the Landau resonance effects since its expression is the same with the dispersion relation derived from kinetic theory.

2. Anomalous resistivity created by current driven instabilities

The linear stability analysis and nonlinear saturation estimation are carried out for

the parameter range of coronal plasma. For instability propagating along the direction of background magnetic field line and plasma drift motion, Buneman mode is the only dominant mode. However, deviate away from the parallel propagation the modified two stream instability (MTSI) also plays an important role, and the growth rate of this mode is comparable to the growth rate of the Buneman mode in the low plasma beta and high relative drift condition. In general this two dimensional dispersion analysis obtains the information that is usually lost in the extensively considered one dimensional dispersion analysis.

In the nonlinear saturation estimation of the instability generated anomalous resistivity, we use the criteria that the electrostatic waves reach saturation level when the plasma particles are trapped in potential wells of instability. After trapping the drifts of different species are reduced and the system is reduced back to marginal stable state. Via this criteria the estimated anomalous resistivity generated by MTSI reaches the same order of magnitude as the Buneman instability. We concluded that in a real current driven plasma environment the anomalous resistivity contributed from MTSI mode should be taken into consideration as well as the widely studied Buneman mode.

3. Particle acceleration via the coronal looptop fast shock

From modern solar coronal HXR observations, the energy of energetic particles during solar flares is retrieved for different stages. The real plasma outflow of the coronal reconnection sites is seldom directly observed then this quantity is usually refered as the Alfvén velocity outside the diffusion region. In both methods the obtained plasma velocity is still much less than the plasma energy obtained from the coronal footpoint HXR emissions. This observation discrepancy implies a secondary acceleration mechanism in addition to the plasma acceleration by magnetic reconnection.

In this PIC simulation with a reflective boundary condition, which is assumed to mimic the obstacle-like coronal SXR loop, a looptop fast mode shock is formed between the reflective boundary and the injecting plasma. The mode of this shock is identified by the signature of the increase of both background magnetic field and plasma density. With the parameters assumed from the local Alfvén velocity, the original $7keV$ quasi-nonthermal plasma outflow can eventually be heated up to a temperature with the thermal velocity $2/3c$ speed of light. These thermal plasma can be further synchronized to be injected to the coronal foot point, and revealing emission spectrum in the level of $100 - 200keV$, which is the usual observed footpoint HXR radiation.

4. Double layers and the resulting broken-power-law spectrum

The electrostatic double layers, which are generated by large scale phase space structure, play important roles in the coronal plasma transport. The original Maxwellian plasma beam injected from the primary acceleration sites gradually evolves into a broken-power-law distribution via the interaction with double layers.

There are three plasma species in our Vlasov code simulation, an injected electron beam, the background ions and the induced return current of electrons. The return current electron is induced by the injected electron beam according the Ampere's law.

In general there are two instabilities in this system, the forward going Buneman or ion acoustic mode propagating in the direction of injected electron beam, and the backward going electron acoustic mode. Because of the smaller mass of electrons the instability growth rate of electron acoustic mode is higher than the ion acoustic mode in the instability linear stage. Therefore the initial free energy goes to this mode instead of ion acoustic

instability. In the nonlinear stage of simulation large scale electrostatic double layers are generated. Starting from the appearance double layers the bulk motion of injected electron beam and return current electron beam are slowed down. Partially the electrons of return current is dragged along with injected beam, and hence the spectrum in the later stage of simulation has the characteriscs of broken-power-law. Although this spectrum looks like the origins of the spectrum coming from two different sources, in our simulation it is shown that spectrum can also be a natural consequence of plasma transport, as a result of plasma interaction with double layers. The dynamics and energy transfer between plasma and waves are also discussed in that chapter.

For the extension of this thesis, the actual acceleration mechanism in the fine structure of looptop fast shock still requires a detailed study, which should contain linear dispersion analysis of the unstable waves in shock transition layer and a more suitable boundary condition for simulation that can represent the real coronal SXR loops. We propose that a multifluid fluid simulation can, till some level, reveal the intresting physics on this topic.

A Derivation of the General Multifluid Dispersion Relation

Waves in multifluid plasma have been discussed quite extensively in the plasma research of past few decades. One of the most detailed discussion is summarized by Swanson (1989) of the previous work of multifluid waves, and the instabilities in some limits were also discussed therein. Therefore, the basis of the knowledge in a multifluid plasma system is substantial.

Nevertheless, because of the high complexity in the multifluid system, a general dispersion relation for the waves and instabilities in a warm magnetized plasma with relative drifts between different species has not been obtained yet. In spite of some limited cases, we also intend to find a general expression that is electromagnetic in nature and the propagation angle is arbitrary referring to background magnetic field. Because of the intention to extend to such a general range, the difficulty of mathematical algebra is expected, although few previous works have been focused on some specific limits and were useful to their applications. However, to obtain a general dispersion relation can help us to identify waves and instabilities, and the discrepancy of previous works can be bridged as well.

To find out the general dispersion relation, we start form a set of conservation equations of mass, momentum and energy. Because the plasma is comprised charged particles, the Maxwell's equations are also used to describe the interaction between each species. In our consideration the binary collision term is neglected, therefore this equation is not applicable to very high density situation where the binary collision takes an important role. The linearized multifluid equations are as follows

$$n_j = N_j \frac{\vec{K} \cdot \vec{u}_j}{\omega_{*j}} \tag{A.1}$$

$$\omega_{*j}^2 \vec{u}_j - S_j^2 \vec{K}(\vec{K} \cdot \vec{u}_j) - i\omega_{*j} \frac{e_j}{m_j}(\delta\vec{E} + \frac{\vec{U}_j \times \vec{b}}{c}) - i\omega_{*j}\vec{u}_j \times \vec{\Omega}_j = 0 \tag{A.2}$$

$$\frac{e_j}{m_j}\delta\vec{E} = \frac{ic^2{\omega_{pj}}^2}{\alpha\omega\sigma_j}(\vec{K}\vec{K} \cdot - \frac{\omega^2}{c^2})\vec{j} \tag{A.3}$$

$$\frac{e_j}{m_j}\vec{b} = -\frac{ic{\omega_{pj}}^2}{\alpha\sigma_j}(\vec{K} \times \vec{j}) \tag{A.4}$$

$$\vec{j} = \sum_j \sigma_j(\vec{u}_j + \vec{U}_j \frac{\vec{K}\cdot\vec{u}_j}{\omega_{*j}}) \tag{A.5}$$

where the notations ω_{*j} and α are defined as below

$$\omega_{*j} = \omega - \vec{K}\cdot\vec{U}_j \tag{A.6}$$

$$\alpha = \omega^2 - c^2K^2 \tag{A.7}$$

As discussed in section 2.1, we are looking for $\vec{u}_j$ and $\vec{K}\cdot\vec{u}_j$ in terms of an inner product of a tensor with $\delta\vec{E}$. Therefore we start from $\vec{K}\cdot(A.2)$

$$\begin{aligned}\omega_{*j}^2(\vec{K}\cdot\vec{u}_j) - S_j^2K^2(\vec{K}\cdot\vec{u}_j) - i\omega_{*j}\frac{e_j}{m_j}(\vec{K}\cdot\delta\vec{E} + \frac{\vec{K}\cdot(\vec{U}_j\times\vec{b})}{c}) \\ -i\omega_{*j}\vec{K}\cdot(\vec{u}_j\times\vec{\Omega}_j) = 0\end{aligned} \tag{A.8}$$

In the above equation, the magnetic perturbation $\vec{b}$ can be derived from Maxwell's equation $\vec{b} = \frac{c}{\omega}\vec{K}\times\delta\vec{E}$, then $\vec{U}_j\times\vec{b}$ be expanded as

$$\vec{U}_j\times(\frac{c}{\omega}\vec{K}\times\delta\vec{E}) = \frac{c}{\omega}((\vec{U}_j\cdot\delta\vec{E})\vec{K} - (\vec{U}_j\cdot\vec{K})\delta\vec{E}) \tag{A.9}$$

Substituting this back to equation A.8, we have

$$\begin{aligned}\omega_{*j}^2(\vec{K}\cdot\vec{u}_j) - S_j^2K^2(\vec{K}\cdot\vec{u}_j) - i\omega_{*j}\frac{e_j}{m_j}(\vec{K}\cdot\delta\vec{E}) - i\omega_{*j}\frac{e_j}{m_j}\frac{K^2}{\omega}(\vec{U}_j\cdot\delta\vec{E}) \\ +i\omega_{*j}\frac{e_j}{m_j}\frac{1}{\omega}(\vec{K}\cdot\vec{U}_j)(\vec{K}\cdot\delta\vec{E}) - i\omega_{*j}\vec{K}\cdot(\vec{u}_j\times\vec{\Omega}_j) = 0\end{aligned} \tag{A.10}$$

In equation A.10, $\vec{K}\cdot(\vec{u}_j\times\vec{\Omega}_j)$ is the term that has not been replaced. To solve we use $\vec{K}\times(A.2)$

$$\begin{aligned}\omega_{*j}(\vec{K}\times\vec{u}_j)\cdot\vec{\Omega}_j = i\frac{e_j}{m_j}[-(\vec{K}\times\vec{\Omega}_j)\cdot\delta\vec{E} + \frac{(\vec{K}\cdot\vec{U}_j)(\vec{K}\times\vec{\Omega}_j)\cdot\delta\vec{E}}{\omega}] \\ +i[(\vec{K}\cdot\vec{\Omega}_j)(\vec{\Omega}_j\cdot\vec{u}_j) - \Omega_j^2(\vec{K}\cdot\vec{u}_j)]\end{aligned} \tag{A.11}$$

Again, the term $\vec{\Omega}_j\cdot\vec{u}_j$ in the above equation is the term that has not been replaced. To solve this we let the background magnetic field is parallel to the drifts of each species $\vec{\Omega}_j//\vec{U}_j$ and then use $\vec{\Omega}_j\cdot(A.2)$

$$\vec{\Omega}_j \cdot \vec{u}_j = \frac{S_j^2(\vec{K}\cdot\vec{\Omega}_j)(\vec{K}\cdot\vec{u}_j)}{\omega_{*j}^2} + i\frac{e_j}{\omega_{*j}m_j}(\vec{\Omega}_j\cdot\delta\vec{E}) \tag{A.12}$$

Then we Substitute this back to equation A.11

$$\omega_{*j}\vec{K}\cdot(\vec{u}_j\times\vec{\Omega}_j) = i\frac{e_j}{m_j}[(\frac{\vec{K}\cdot\vec{U}_j}{\omega}-1)(\vec{K}\times\vec{\Omega}_j)]\cdot\delta\vec{E} \tag{A.13}$$
$$+i[\frac{S_j^2(\vec{K}\cdot\vec{\Omega}_j)^2}{\omega_{*j}^2}(\vec{K}\cdot\vec{u}_j) + i\frac{e_j}{\omega_{*j}m_j}(\vec{K}\cdot\vec{\Omega}_j)(\vec{\Omega}_j\cdot\delta\vec{E}) - \Omega_j^2(\vec{K}\cdot\vec{u}_j)]$$

Put (A.13) back to (A.10) to replace the last term $\omega_{*j}\vec{K}\cdot(\vec{u}_j\times\vec{\Omega}_j)$ then we obtain

$$(\vec{K}\cdot\vec{u}_j)(\omega_{*j}^2 - S_j^2K^2 + \frac{S_j^2(\vec{K}\cdot\vec{\Omega}_j)^2}{\omega_{*j}^2} - \Omega_j^2) = \tag{A.14}$$
$$i\omega_{*j}\frac{e_j}{m_j}[\vec{K} + \frac{K^2}{\omega}\vec{U}_j - \frac{(\vec{K}\cdot\vec{U}_j)\vec{K}}{\omega}$$
$$+i\frac{(\vec{K}\cdot\vec{U}_j-\omega)(\vec{K}\times\vec{\Omega}_j)}{\omega_{*j}\omega} - \frac{\vec{K}\cdot\vec{\Omega}_j\Omega_j}{\omega_{*j}^2}]\cdot\delta\vec{E}$$

Till this step we have found the term $(\vec{K}\cdot\vec{u}_j)$, which should be replaced into wave equation to find out dispersion relation. Therefore we leave the equation A.14 temporarily and look for a replacement of another term $\vec{u}_j$.

Equation A.3 is the wave equation which can be used to solve dispersion relation, and it can be expressed as

$$(\omega^2 - c^2K^2)\delta\vec{E} = \frac{ic^2{\omega_{pj}}^2m_j}{\omega\sigma_je_j}(\vec{K}\vec{K}\cdot - \frac{\omega^2}{c^2})\vec{j} \tag{A.15}$$
$$= 4\pi\frac{ic^2}{\omega}\left[\Sigma_j(\sigma_j\omega\frac{\vec{K}(\vec{K}\cdot\vec{u}_j)}{\omega_{*j}}) - \frac{\omega^2}{c^2}\vec{j}\right]$$

In the above equation, the coefficient 4π appears because of the definition of the plasma frequency $4\pi\frac{e_j^2N_j}{m_j} = \omega_{pj}^2$ in CGS units system. In equation A.5 that represents the whole current, $\vec{u}_j$ is the term that has not been transformed, then

$$\omega_{*j}^2\vec{u}_j = S_j^2\vec{K}(\vec{K}\cdot\vec{u}_j) + i\omega_{*j}\vec{u}_j\times\vec{\Omega}_j \tag{A.16}$$
$$+i\omega_{*j}\frac{e_j}{m_j}\left[\underline{\underline{I}}\cdot\delta\vec{E} + \frac{\vec{K}(\vec{U}_j\cdot\vec{\delta}E)}{\omega} - \frac{(\vec{U}_j\cdot\vec{K})}{\omega}\underline{\underline{I}}\cdot\delta\vec{E}\right]$$

In the above equation $\vec{u}_j \times \vec{\Omega}_j$ has not been transformed, so we use $\vec{\Omega}_j \times (A.2)$

$$\omega_{*j}^2(\vec{\Omega}_j \times \vec{u}_j) = S_j^2(\vec{\Omega}_j \times \vec{K})(\vec{K} \cdot \vec{u}_j) + i\omega_{*j}\frac{e_j}{m_j\omega}(\vec{\Omega}_j \times \delta\vec{E}) \tag{A.17}$$
$$+i\omega_{*j}\frac{e_j}{m_j\omega}(\vec{\Omega}_j \times \vec{K})(\vec{U}_j \cdot \delta\vec{E}) - i\omega_{*j}\frac{e_j}{m_j\omega}(\vec{U}_j \cdot \vec{K})(\vec{\Omega}_j \times \delta\vec{E})$$
$$+i\omega_{*j}(\Omega_j^2\vec{u}_j - (\vec{\Omega}_j \cdot \vec{u}_j)\vec{\Omega}_j)$$

Also the term $(\Omega_j \cdot \vec{u}_j)\vec{\Omega}_j$ in the above equation should be replaced. We then use the relation $(\Omega_j \cdot A.2)\vec{\Omega}_j$ to derive

$$(\Omega_j \cdot \vec{u}_j)\vec{\Omega}_j = \frac{S_j^2(\vec{K} \cdot \vec{\Omega}_j)\vec{\Omega}_j(\vec{K} \cdot \vec{u}_j)}{\omega_{*j}^2} + \frac{i\omega_{*j}\frac{e_j}{m_j}\vec{\Omega}_j\vec{\Omega}_j \cdot \delta\vec{E}}{\omega_{*j}^2}$$

Put the above expression in to equation A.17

$$\omega_{*j}(\vec{\Omega}_j \times \vec{u}_j) = -\frac{S_j^2(\vec{\Omega}_j \times \vec{K})(\vec{K} \cdot \vec{u}_j)}{\omega_{*j}} + i\frac{e_j}{m_j}(1 - \frac{(\vec{U}_j \cdot \vec{K})}{\omega})(\vec{\Omega}_j \times \delta\vec{E}) \tag{A.18}$$
$$-i\omega_{*j}\frac{e_j}{m_j\omega}(\vec{K} \times \vec{\Omega}_j)(\vec{U}_j \cdot \delta\vec{E}) + \frac{e_j}{\omega_{*j}m_j}\vec{\Omega}_j\vec{\Omega}_j \cdot \delta\vec{E} + i\Omega_j^2\vec{u}_j$$

Now replace this term back to equation A.16, we obtain

$$(\omega_{*j}^2 - \Omega_j^2)\vec{u}_j = \left(S_j^2\vec{K} + i\frac{S_j^2}{\omega_{*j}}(\vec{K} \times \vec{\Omega}_j) - \frac{S_j^2}{\omega_{*j}^2}(\vec{K} \cdot \vec{\Omega}_j)\vec{\Omega}_j\right)(\vec{K} \cdot \vec{u}_j) + \tag{A.19}$$
$$\left[i\omega_{*j}\frac{e_j}{m_j}\left(\underline{\underline{I}} + \frac{\vec{K}\vec{U}_j}{\omega} - \frac{\vec{U}_j \cdot \vec{K}}{\omega}\underline{\underline{I}}\right) - \frac{e_j}{m_j}\left(\frac{(\vec{K} \times \vec{\Omega}_j)}{\omega}\vec{U}_j + i\frac{\vec{\Omega}_j\vec{\Omega}_j}{\omega_{*j}}\right)\right] \cdot \delta\vec{E}$$
$$+\frac{e_j}{m_j}(1 - \frac{\vec{K} \cdot \vec{U}_j}{\omega})\underline{\underline{A}} \cdot \delta E \tag{A.20}$$

where

$$\begin{pmatrix} 0 & -\Omega_{zj} & \Omega_{yj} \\ \Omega_{zj} & 0 & -\Omega_{xj} \\ -\Omega_{yj} & \Omega_{xj} & 0 \end{pmatrix} \cdot \delta\vec{E} = 0; \underline{\underline{A}} \cdot \delta\vec{E} = \vec{\Omega}_j \times \delta\vec{E}$$

In equation A.19 we have obtained the information of $\vec{u}_j$ in terms of $\vec{K} \cdot \vec{u}_j$ and $Tensor \cdot \delta\vec{E}$. Combining with the equation A.14 that replaces the term $\vec{K} \cdot \vec{u}_j$, we can obtain an equation that is expressed in the form of $Tensor \cdot \delta\vec{E}$ only, the so called dispersion relation.

The procedures are, first replacing $\vec{u}_j$ in equation A.5 to obtain $\vec{j}$ in terms of $\vec{K} \cdot \vec{u}_j$, and then putting $\vec{j}$ into the wave equation A.15. Till this step, the only term we should replace is $\vec{K} \cdot \vec{u}_j$, which can be solved by equation A.14. The derived general dispersion relation, equation 2.19 for a warm magnetized plasma with relative drifts is obtained, and this relation applies to all wave propagation angles.

B Wave and Instability Identification in a Multi-Fluid Plasma

With the one-fluid assumption of a warm magnetized uniform plasma, there are only three characteristic waves exsiting in the system. This approach is the so-called magnetohydrodynamics (MHD) limit, and it is applicable and useful for most of the large spatial-scale and low-frequency plasma phenomena. However, mumerous highly energetic processes in space plasma environment such as the particle acceleration in solar flares, or the plasma transport in the laboratory Tokamak plasma, the kinetic effects should be considered in order to reflect the self-generated dynamics precisely and also avoid the abuse of physical parameters assumptions, which are sometimes over-estimated in the sigle fluid model. The kinetic effects also play important roles in the particle acceleration mechanism or in the so-called collisionless resistivity (Anomalous resistivity), for which the necessary generation of local electric field is a key feature, and this is neglected in the charge-neutrality ideal MHD assumption.

In principle, an electric field in the plasma waves is demonstrated as one or a few charge-separation sites in the wave fine-structures. In a fully kinetic approach, the net spatial charge depends on the plasma distribution of each species, hence the value of the local net charge can be either positive or negative accumulated and local electric fields are generated. Nevertheless, the kinetic approach of solving plasma problems usually faces the difficulty of system complexity, especially in the numerical simulations, an inevitable process is to seek for a compromised fluid description that contains the "to-some-level" kinetic effect. To obtain the required information of the localized electric field in plasma, the multi-fluid treatment is a good expression for saving the charge seperation characteristics, and it also maintains the Gaussian shape plasma distribution for each species so that the advantage of an efficient numerical calculation is preserved.

In a multifluid system, more plasma waves and instabilities are expected than in MHD, and indeed these waves are of higher frequency than those in the MHD limit because of the individual motions (as relative moving fluids) of different species, and most important of all the mutual interaction of different species are also considered. In addition, numerous kinds of current driven instability are triggered in the multifluid system according to the provided free energy, which are exihibited as the relative drifts of each species. In appendix A we derived the general electromagnetic dispersion relation of a warm magnetized plasma. In this section it is focused on the method of how to distinguish the different instabilities in a three-fluids electrostatic plasma.

Because of the complexity in multifluid system, many waves and instabilities were previously studied under assumptions, such as the wave propagation angle is either in

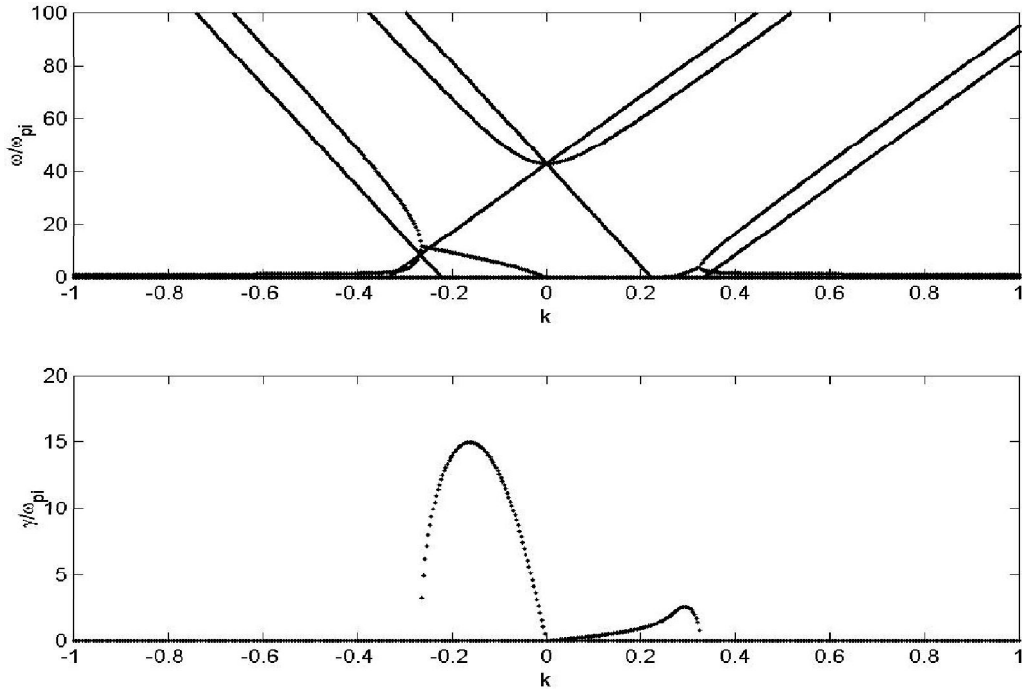

Figure B.1: The dispersion curves of a three-fluids system is shown in this plot. The upper panel exhibits the real frequencies of each branches and the lower panel shows the corresponding grwoth rates of the unstable modes.

parallel or perpendiclar to ambient magnetic field. Different names are given for different conditions, and sometimes even for the waves of the same branch in the dispersion surface. Therefore it causes great confusion for the understanding of the wave nature and also the transition from one angle to another. In addition, even for a single propagation direction names are sometimes misused when there are more than two species existing in the system. The wave frequencies, the real part of the solution of dispersion relation, are connected to each branches, therefore the instability modes shown in dispersion plot are considered the same although their corresponding growth rates are very different. To introduce the basic concept of waves and instabilities identification, we should start from an electrostatic case in the multifluid system.

In Fig. B.1 a typical three-fluids dispersion plot along the direction of magnetic field is shown. An ion species appears in the system as the background medium and the dispersion curves are all based on the ion reference frame. In this setup there are two counter-streaming electron species drifting along the background magnetic field. All these three components are cold, in order to discuss the simplest case, and the charge-neutrality is set, i.e. the total electron density is equal to the background ion density. The positively drifting electron beam has a normalized velocity $V_{1,drift} = 3$, which is normalized to the unit of background Alfvén velocity, and the negatively drifting electron has a velocity $V_{2,drift} = -4.5$.

Several wave modes and two instabilities are shown in this plot. Because of the relative drift between ions and electrons, the electron plasma frequencies are Doppler-shifted

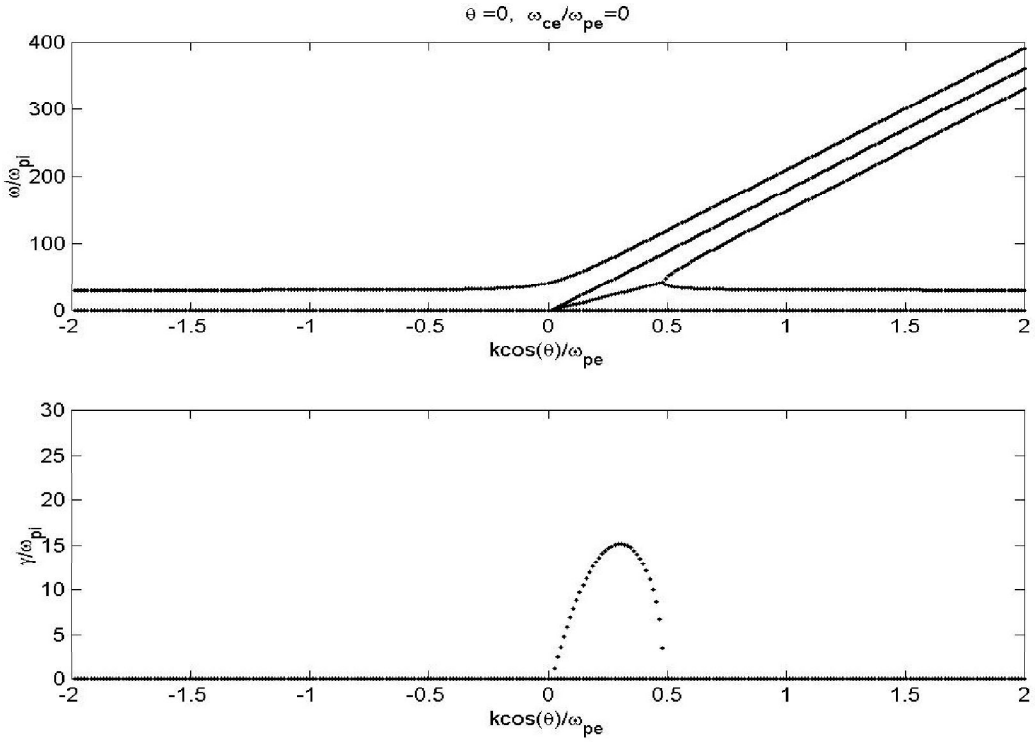

Figure B.2: The real frequency and growth rate of the electron-electron system are shown in this plot. The relative speed between two electrom species is the same as the value used in Fig. B.1.

referring to ions. This Doppler-shift effect is demonstrated as the inclined frequency branches, either with positive or negative slops. In the reference of electrons, we see the electron Langmuir waves propagate both forward and backword to the drift, although in fact they are just oscillations and their group velocities are zero, two Doppler-shifted branches of one drifting species are shown in the dispersion plot. To distinct one wave from the other in this Doppler-shifted pair, we call a branch is forward propagating if the phase velocity is faster than the drift velocity in the ion rest frame, and backward propagating if the phase velocity is slower than the drift velocity. With this discrepancy there are two electron Langmuir waves to both the positively drifting and negatively drifting electron species. It is the same to the background ion, two ion Langmuir oscillations are also propagating forward and backward to ion reference frame. One point to be addressed is, the information of this ion Langmuir oscillation do not really propagate, since in cold plasma limit the sound velocities are zero, but the phase velocities are not zero.

With the knowledge of how to distinguish different waves, we then look at the drift instabilities caused by the wave-coupling of those branches. It's clear that two instabilities correspond to the forward and backward directions. It is quite surprising that, although the dispersion curves of the real wave frequency are similar for both propagation directions and the drift velocities are not too different, which is shown in the upper panel of Fig. B.1, the corresponding growth rates of these coupling have very different values, which is shown in the lower panel of Fig. B.1. In reality this suggests that the causes of these instabilities can come from different origins, but the complicated dispersion curves does

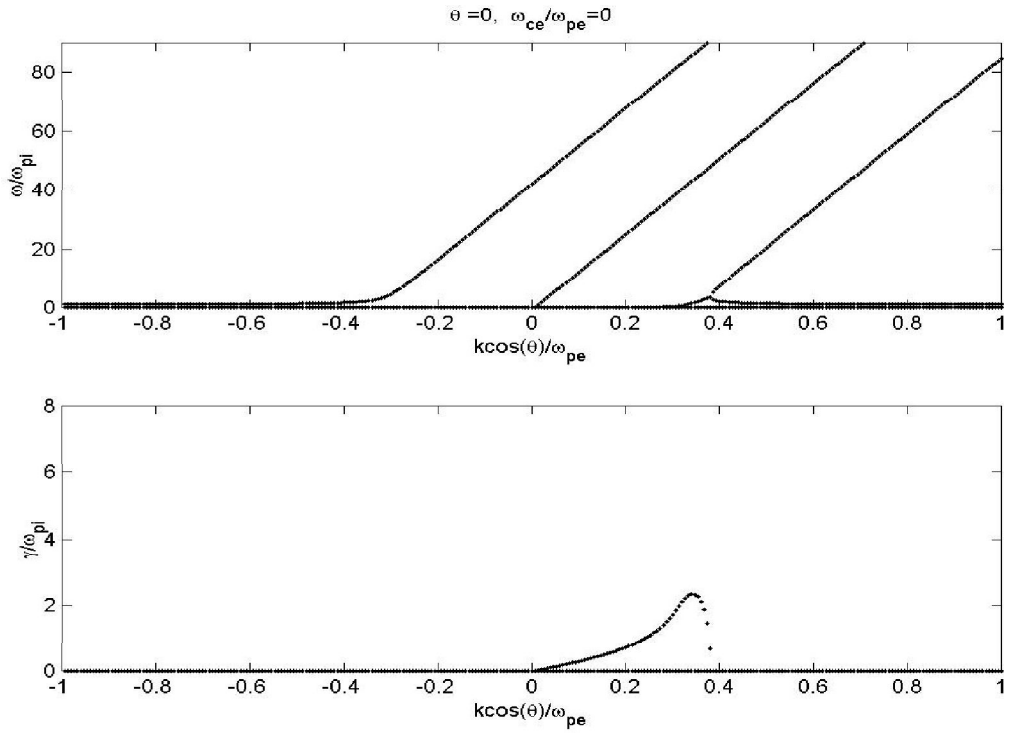

Figure B.3: The real frequency and growth rate of the electron-ion system are shown in this plot. The electron existing here mimics the backward drifting flow, and the relative speed between ion and electron is the same as the value used in Fig. B.1.

not allow a clear distinction of wave coupling at the first glance. To clarify the instability nature, we carry out a "sub-system" analysis to identify the instability modes in a complex system.

With an implied electromagnetic field, in general, species with smaller mass usually respond to the force more instantaneously and heavior particles require longer time to react according to the higher inertia. Therefore in a two electrons and one ion species system, we expect the interaction between the two electron species would respond faster, and the frequencies and growth rates can be found from the dispersion relation

$$0 = 1 - \frac{\omega_{pe1}^2}{(\omega - \vec{k}\cdot\vec{V}_{e1})^2} - \frac{\omega_{pe2}^2}{(\omega - \vec{k}\cdot\vec{V}_{e2})^2} \tag{B.1}$$

The dispersion curves of Eq. B.1 are shown in Fig. B.2. It is obvious the instability shown here is the result of the interaction of two electron Langmuir waves, or the electron acoustic waves when the thermal effects of electron are considered. Hence it is appropriate to call this instability an "electron acoustic instability". It is shown that the highest growth rate along the background magnetic field is around $\gamma \approx 15\omega_{pi}$ with the relative drift between two electrons $V = 7.5$.

With the same token, the interaction between the background ion and the forward streaming electrons can also be analyzed with the consideration of these two species only. The expected wave coupling in this circumstance is between the backward propagating

electron Langmuir wave and the forward propagating ion Langmuir wave, or the electron acoustic wave with ion acoustic wave in thermal case, and this has been studied by Buneman (1958) in his famous work. The dispersion relation of the sub-system is expressed as

$$0 = 1 - \frac{\omega_{pi}^2}{\omega^2} - \frac{\omega_{pe}^2}{(\omega - \vec{k} \cdot \vec{V}_e)^2} \tag{B.2}$$

The dispersion curves of Eq. B.2 are shown in Fig. B.3. We can see the highest growth rate in this case is around $\gamma \approx 3\omega_{pi}$ with a drift between ion and electron $V = 3$. It is very different from the growth rate of electron acoustic instability, and conventionally this instability is called "Buneman instability".

To the first order of correctness, the interactions of every two species are considered. The last interaction between the background ion and the backward drifting electron shows no instability because the electron acoustic instability in the negative direction has a much higher growth rate and with the same electrostatic nature, therefore the provided free energy is taken by the forward drifting electron instead of the background ion, another Buneman mode is not expected in this direction. In this analysis, it is shown that even a single interaction between each two species in a multifluid complex system is still preserved as its orginal characteristics with only two species. The abundence of informations contained in a multi-species system can be actually broken down and analyzed in a relatively physical transparent "sub-system". Therefore with the "sub-system" we described here, it is possible to identify different modes in a complicated system.

Bibliography

Aggarwal, S. S. 1979, Astrophysics and Space Science, 66, 341

Ahedo, E. and V. Lapuerta 2001, Phys. Plasmas, 8, 3873

Alexander, D., & Metcalf, T. R. 1997, ApJ, 489, 442

Alfven, H. & Carlqvist, P. 1967, Solar Phys., 1, 220

Antonucci. 1995, Il Nuovo Cimento D

Arfken, G. B. and H. J. Weber 1995, Mathematical Methods for Physicists (Academic Press: London), ISBN 0120598159, pp.414

Aschwanden. 1999, ApJ, 517, 977

Aschwanden, M. 2002, Solar Phys., 210, 383

Aschwanden, M. 2006, Physics of the solar corona (Springer)

Aschwanden, M.J., & Schwartz, R.A. 1996, ApJ 464, 974.

Aschwanden, M.J. 1999a, SP 190, 233.

Aschwanden, M.J. 2001, ApJ 560, 1035.

Aschwanden, M.J., Brown, J.C., & Kontar, E.P. 2002b, Solar Phy., 210, 383.

Bai, T., Hudson, H.S., Pelling, R.M., at el. 1983, ApJ 267, 433.

Battaglia, M. and Benz, A. O. 2006, A&A 456, 751

Bellan, P. 1999, Phys. Rev. Lett., 83, 4768

Benz, A.O. & Smith, D.F. 1987, SP 107, 299.

Block, L. 1977, ApSS, 55, 59

Bogachevm, S. A. and B. V. Somov 2007, Astronomy Letters Vol. 33, No. 1, 54

Bohm, D. 1949, Minimum ionic kinetic energy for a stable sheath (New York: McGraw-Hill)

Borovsky, J. 1986, ApJ, 306, 451

Borovsky, J. E. 1992, Phys. Rev. Lett., 69, 1054

Boswell, R.W., Marsch, E. and Charles, C. 2006, Astrophys. J. 640, L199

Boswell, R. W., Marsch, E., & Charles, C. 2006, Astron. J., 640, L199

Brown. 1971, Solar Phys., 18, 489

Brown, J.C. & Melrose, D.B. 1977, SP 52, 117.

Brown, J.C., Aschwanden, M.J., & Kontar, E.P. 2002a, SP 210, 373.

Brown, M.R., Cothran, C.D., Landerman, M., et al. 2002, ApJ 577, L63.

Burgess, D. 2006, J. Geophys. Res., 111, A10210

Büchner, J. & Elkina, N. 2005, Space Sci. Rev., 121, 237

Büchner, J. & Elkina, N. 2006, Phys. Plasmas, 13, 2304

Büchner, J. 2006a, Space Sci. Rev., 122, 149

Büchner, J. 2006b, Space Sci. Rev., 124

Büchner, J. & Daughton, W. 2007, The role of current-aligned instabilities in reconnection (Cambridge, UK: Cambridge University Press), 145

Buneman, O. 1958, Phys. Rev. Lett., 1, 8

Buneman, O. 1959, Phys. Rev., 115, 503

Buneman, O. 1963, J. Nucl. Energy C, 4, 111

Bychenkov, V., Silin, V., & Uryupin, S. 1988, Physics Report, 164, 119

Coroniti, F. V. 1985, Space Sci. Rev., 42, 399

Cromwell, D., McQuillan, P., & Brown, J. C. 1988, Solar Phys., 115, 289

Davidson, R. 1983, Basic Plasma Physics 1: Chap. 3.3 Kinetic waves and instabilities in a uniform plasmas (North-Holland Publishing Company)

Davidson, R. C. & Gladd, N. T. 1975, Physics of Fluids, 18, 1327

Dennis, B. R. 1988, Solar Phys. 118, 49.

Diaz,C. J. 1981, Plasma Phys. 23 455

Dreicer, H. 1959, Phys.Rev. 115, 238.

Elkina, N. & Büchner, J. 2006, J. of Comp. Phys., 213, 862

Emslie. 1980, ApJ, 235, 1055

Ergun. 1998, Geophys. Rev. Lett., 25, 2041

Fletcher, L. 2005, Space Science Rev., 121, 141

Fletcher, L., and DePontieu, B. 1999, ApJ 520, L135.

Fredrick, R. W., F. V. Coroniti, C. F. Kennel and F. L. Scarf 1970, Phys. Rev. Lett., 24, 994

Gary, A., Smith, C., & Lee, A. 1984, Phys. Fluids, 27, 1852

Gary, G. A. & Alexander, D. 1999, Solar Phys., 186, 123

Gary, S. P. 1993, Theory of Space Plasma Microinstabilities (Theory of Space Plasma Microinstabilities, by S. Peter Gary, pp. 193. ISBN 0521431670. Cambridge, UK: Cambridge University Press, September 1993.)

Grigis, P. C., & Benz, A. O. 2004, A&A, 426, 1093

Hairapetian, G. & Stenzel, R. 1990, Phys. Rev. Lett., 65, 175

Hildebrandt, J., Krüger, A., Chertok, Fomichev, V. V. and Gorgutsa, R. V. 1998, Solar Physics, 181, 337

Hamilton, R.J. & Petrosian, V. 1992, ApJ 398, 350.

Hirose, A. 1978, Plasma Phys., 20, 481

Holman, G. D., Sui, L., Schwartz, R. A., & Emslie, A. G. 2003, ApJ, 595, L97

Holman, G.D. 1985, ApJ 293, 584.

Hoshino, M. and N. Shimada 2002, ApJ 572, 880

Ishihara, O., Hirose, A., & Langdon, A. 1981, Phys. Fluids, 3, 452

Jovanović, D., and P. K. Shukla 2004, Phys. Rev. Lett., 93, 015002-1

Jones, F.C. 1994, ApJS 90, 561.

Kallenrode, M.-B. 2003, J. Phys. G: Nucl. Part. Phys. 29, 965

Kane, S. R., & Anderson, K. A. 1970, ApJ, 162, 1003

Khan, J. 1989, Proc. of Asronomical Society of Australia, 8, 29

Knoepfel, H., & Spong, D.A. 1979, Nucl.Fusion, 19/6, 785.

Kudriavtsev, I. V., Charikov, I. E. 1989, Pis'ma v Astronomicheskii Zhurnal, 15, 353

Kuramitsu, Y. & Krasnoselskikh V. 2005, Phys. Rev. Lett. 94, 031102

Krauss-Varban, D., & Wu, C. S. 1989, J. Geophys. Res., 94, 15367

Krotscheck, E., and W. Kundt 1978, Communications in Mathematical Physics, 60, 171

Landau, L. D. 1946, J. Phys.(U.S.S.R.), 10, 25

Langmuir. 1929, Phys. Rev., 33, 954

Lapuerta, V. and E. Ahedo 2001, Spacecraft Charging Technology, Proceedings of the Seventh International Conference held 23-27 April, 2001 at ESTEC, ESA SP-476, 2001., p.563

Lee, R. E., S. C. Chapman and R. O. Dendy 2004, 31st EPS Conference on Plasma Phys. London, 28G, O-4.15

Leonid M. Malyshkin & Russell M. Kulsrud 2006, arXiv:astro-ph/0609342v1

Levinson, A. 1992, ApJ, 401, 73

Li, P. 1995, Astrophys. J. 443, 855.

Lin, R. P. and Schwartz, R. A. 1987, Astrophys. J. 312, 462.

Litvinenko, Y.E. and Somov, B.V. 1995, SP 158, 317.

Litvinenko, Y.E. 1996b, ApJ 462, 997.

Lotko, W. 1986, J. Geophys. Res., 91, 191

Lynch, K. A.; Bonnell, J. C. C. W. P. W. J. 2001, American Geophysical Union, Spring Meeting 2001, SM41B-04

MacKinnon, A.L.., B. J. H. J. 1985, Solar Phys., 99, 231

Mantei, T. D., F. Doveil, D. Gresillon 1976, Plasma Phys., 18, 705

Marian Karlický 1993, Solar Phy., 145, 137

Mascheroni, P. L. 1977, Phys. Rev. Lett., 39, 197

Masuda, S., Kosugi, T., Hara, H., et al. 1994, Nature 371, No. 6497, 495.

Matsushita, K., Masuda, S., Kosugi, T., et al. 1992, PASJ 44, L89.

McAteer, R. T. J., et al. 2007, ApJ, 662, 691-700,

McClements, K.G., Su, J.J., Bingham, R., et al. 1990, SP 130, 229.

McTiernan, J. M. & Petrosian, V. 1991, Astrophys. J. 379, 381.

McQuillan, P. & McClements, K. G. 1988, J. Plasma Phys., 40, 493

McKenzie, D.E. & Hudson, H.S. 1999, ApJ, 519, L93

McMillan, B. B. & Cairns, I. 2006, Phys. Plasma, 13, 052104

McMillan, B. B. & Cairns, I. 2007, Phys. Plasma, 14, 2103

Melrose, D. B., Instabilities in Space and Laboratory Plasmas (Cambridge University Press, Cambridge, 1986)

Newman, D. L., M. G. 2001, PRL, 87, 255001

Nezlin, M. 1976, Sov. Phys. Usp., 19, 946

Ogawara, Y. et al. 1991, Solar Phy., 136, 1-16

Ott, E., McBride, J. B., Orens, J. H., & Boris, J. P. 1972, Physical Review Letters, 28, 88

Panov, E. V., Büchner, J., Fränz, M., et al. 2006, Geophys. Res. Lett., 33, 15109

Papadopoulos, K. 1988, Ap&SS, 144, 535

Parks, G. K., & Winckler, J. R. 1969, ApJ, 155, 117

Petrosian, V., Donaghy, T. Q., & McTiernan, J. M. 2002, ApJ, 569, 459

Phillips, K.J.H. 2004, ApJ 605, 921.

Piana, M., Massone, A. M., and Kontar, E. P. et al. 2003, Astrophys. J. Letts. 595, L127.

Priest, E. & Forbes, T. 2000, Magnetic reconnection: MHD theory and applications (Cambridge)

Rowland, H. L. & Vlahos, L. 1985, Astronomy Astrophys, 142, 219

Sato, T., and H. Okuda 1980, Phys. Rev. Lett., 44, 740

Shiota D. et al. 2005, ApJ, 634:663ąV678

Sizonenko, V. & Stepanov, K. 1971, Plasma Phys., 13, 1033

Somov, B.V. & Kosugi, T. 1997, ApJ, 485, 859.

Steinacker, J. & Miller, J.A. 1992, ApJ 393, 764.

Stoof, H. T. C. 1993, Phys. Rev. B 47, 7979

Sturrock, P.A. 1966, Nature 5050, 695.

Sui, L. & Holman, G. D. 2003, ApJ, 596, 251

Sui, L., Gordon D. Holman, and Brian R. Dennis 2006, ApJ, 645, L157

Sukovatov, Yu.A. 2004, Physica Scripta, 64, 398

Swanson, D. G. 1989, Plasma Waves (Academic Press: London), ISBN 012678955X, pp.137

Takaaki Yokoyama & Kazunari Shibata 1997, ApJ, 474, L61

Tohru Shimizu, Koji Kondo & Masayuki Ugai 2005, ESA SP, 596E, 25S

Treumann, R. A. 2001, Earth Planet Space, 53

Tsuneta, S. & Naito, T. 1998, ApJ 495, L67.

Tsuneta, S. 1985, ApJ 290, 353.

Uzdensky, D. 2003, Astrophys. J., 587, 450

Vedenov, A. 1963, J. Nuclear Fusion, 5, 169

Vestrand, W. T. 1988, Solar Phys. 118, 95.

Vlasov, A. A., J. Phys. (U.S.S.R.), 9, 25

Voitenko, Y. 1995, Solar Phys., 161, 197

Volwerk, M. 1993, PhD Thesis, Strong Double Layers in Astrophysical Plasmas, Utrecht University, The Netherlands.

Waldmeier, M., 1957, Die Sonnenkorona, vol. 2 (Basel: Verlag Birkhäuser)

Watt, C. E. J., Horne, R. B., & Freeman, M. P. 2002, Geophys. Rev. Lett., 29,

Wild J P, Smerd S F and Weiss A A 1963 Ann. Rev. Astron. Astrophys. 1 291

Winske, D. 1985, Space Science Reviews, 42, 53

Wolfgang Baumjohann and Rudolf A. Treumann 1997, Basic Space Plasma Physics (Imperial College Press: London), ISBN 186094079X, pp.254

Wu, C.S. 1984, J. Geophys. Res. 89, 8857.

Yajima, A. & Machida, S. 2001, Earth, Planets and Space, 53, 139

Yoon, P. & Lui, T. 2006, J. Geophys. Res., 111, A02203

Zhang, H.Q., Sakurai, T., Shibata, K., et al. 2000, Astron. Astrophys, 357, 725.

Zharkova. 1997, Astron. Astrophys, 320, 13

Zharkova,V. V. and M. Gordovskyy 2005, Astron. Astrophys, 432, 1033ąV1047

Publications

K. W. Lee, N. V. Elkina and J. Büchner 2007, Geophysical Research Abstracts, Vol. 9, 00884

K. W. Lee, N. V. Elkina and J. Büchner 2007, Geophysical Research Abstracts, Vol. 9, 01098

K. W. Lee, J. Büchner and N. V. Elkina 2007, Current driven low-frequency electrostatic waves in the solar corona: Linear theory and nonlinear saturation, Phys. Plasmas 14, 112903

K. W. Lee, J. Büchner and N. V. Elkina 2008, Collisionless transport of energetic electrons in the solar corona due to current-free double layers, Astron. Astrophys, 478, 889